Thermophysical Properties and Bulk Ion Irradiation Investigations in Ceramics with Potential Nuclear Applications

Author:
Zhang, Ji

Publication Date:
2016

DOI:
https://doi.org/10.26190/unsworks/19085

UNSW Australia

Faculty of Science

School of Materials Science and Engineering

Thermophysical Properties and Bulk Ion Irradiation Investigations in Ceramics with Potential Nuclear Applications

A Thesis in

Materials Science and Engineering

By

Ji Zhang

Submitted in Partial Fulfilment of the

Requirements for the Degree of

Master of Engineering

April 2016

ACKNOWLEDGEMENTS

First of all, I would like to express my gratitude to Prof. Sean Li, who has given me the opportunity to study in his group. His invaluable guidance and enlightening advices have led me in a correct direction.

I would like to express my deepest thanks to Dr. Daniel J. Gregg from ANSTO (Australian Nuclear Science and Technology Organisation) for enlightening me the first glance of research related to radiation damage. Working under the tutelage of great materials scientist like him gave me the opportunity to learn more and improve better in the field of materials science. His valuable advice was indispensable to this work.

I am very grateful to Dr. Eric R. Vance, Dr. Gregory R. Lumpkin, Dr. Gordon J. Thorogood, and Dr. Ken Short from ANSTO for being so kind, helpful and motivating. During the course of my work, they have provided me invaluable advices and knowledge for data analysis throughout my master research.

I also express my gratitude my gratitude to technical staff in UNSW and ANSTO, for their technical support and assistance in experimental work, various training provided for the better understanding of instruments I used during the course of my master studies. Special thanks to Dr. Thiam Tech Tan, Kim Lu from ANSTO for their support in each and every respect.

I sincerely appreciate the companionship of my lab mate: Rui Guo, roommates: Yunfeng Li, Runzhi Zhang, Yifeng Jiang, Peizhe Guan and Yingze Zhou, and gym mate: Xingrun Xiong (Carrie) for providing a good working and living atmosphere.

All of the support acquired from knowledge and shape my ideas to date comes from the faith, hope and pride of my parents. It was their love, patient encouragement, which keeps me on going. There are no better words to express the feeling of gratitude to them, although I offer my sincere words of acknowledgement to them. Finally, it has been a pleasure journey to conduct my master in UNSW, Sydney.

Abstract

The growing stockpiles of plutonium and minor actinides have become a worldwide issue. Methods of actinide management include developing materials for nuclear waste forms and inert-matrix fuels (IMF) for actinide burning. The work described here has included thermal property assessment of potential IMF materials produced via a novel synthesis method, and radiation-damage studies of a range of ABO_4 compounds with potential as nuclear waste forms.

In the first study, a smaller particle size (submicron) and improved homogeneity of MgO-$Nd_2Zr_2O_7$ IMF mixtures were achieved via a novel aqueous solution method. Thermal diffusivity, heat capacity, thermal expansion and thermal conductivity measurements found that the smaller particles did not significantly reduce the resulting material's thermal properties when compared to samples prepared by more traditional synthetic methods. Importantly, the homogeneity produced is a key factor that could significant effect the performance of the IMF at elevated temperature in reactor.

Study 2 and study 3 were focused on the effects of Au ion-beam irradiation on the structural properties of ABO_4 compounds. It was found that $CaWO_4$ (scheelite) and YVO_4 (zircon) both with tetragonal structures, displayed less damage than $LaVO_4$ (fergusonite), $LaNbO_4$ (fergusonite) and $YNbO_4$ (monazite) with monoclinic structures. The results suggest that the radiation tolerance was better with higher atomic number in group II and $CaWO_4$ showed evidence of a slow recovery from its damaged structure, even at room temperature. Further, thermal annealing experiments were undertaken to investigate recovery of the material from the damage.

List of Figures

List of Tables

1. Introduction

1.1 Project objectives

The global stockpiles of plutonium were estimated to be around 505 tons at the end of 2014 and is growing steadily, and they represent a proliferation concern [1]. Plutonium and other actinides need to be immobilised on their amounts reduced by satisfactory means. Inert matrix fuel (IMF, burning surplus plutonium and other minor actinides in light water reactor) and advanced nuclear waste forms (such as Synroc, nuclear waste host phase materials for long-term disposal) were the subject of my study focus. In this work, my objectives were to investigate a new molecular level synthetic approach for a more homogenous MgO-$Nd_2Zr_2O_7$ (a potential IMF candidate), and to determine the radiation damage tolerance of a family (ABO_4 structure type) of potential nuclear waste host materials.

1.2 Overview

Chapter 1, briefly introduce the project objectives in this work.

Chapter 2, started with an introduction and overview of the general principles of thermal property on parameters that contribute to thermal conductivity, and basic mechanisms of radiation damage, experimental parameters and amorphization mechanisms.

Chapter 3, instruments for characterization were briefly introduced such as X-ray diffraction (XRD), scanning electron microscopy (SEM), transmission electron microscope (TEM), and Raman spectroscopy. Also instruments for thermal property measurements like Simultaneous Thermal Analysis (STA), dilatometer (DIL) and laser flash (LFA) were described.

Chapter 4, the Thermophysical and structural properties of materials produced via a novel synthesis approach for MgO-$Nd_2Zr_2O_7$ mixture were assessed. A comparison with traditional production methods was also discussed. The novel method provides a simple pathway for the candidate IMF MgO–lanthanide zirconate pyrochlore production without need for organic solvents and mechanical milling, making it very attractive for a potential scale-up production.

Chapter 5, a range of nuclear waste host phase materials with various structures within the (ABO_4 type compounds) was studied. Au ion irradiation was used to simulate the α-radiation. Grazing incidence X-ray diffraction was used to examine the damaged layer, and irradiated samples were cross-sectioned for SEM and Raman analyses. This study provides guidance for further investigation on ABO_4 compounds.

Chapter 6, as a continued of the study on ABO_4 structure types, scheelite and powellite compounds were investigated. Different A- and B-site atoms were selected for the Au ion irradiation study. The same characterization techniques were used to those described above to further investigate the structural changes following radiation damage. The radiation tolerance of these compounds was outstanding, and the structural changes during and after irradiations were very interesting, however more work needs to be done in order to fully understand these features.

Chapter 7, summarises all experimental findings in this thesis and provides valuable information for future research on the radiation damage of the ABO_4 structure type as waste form candidates.

2. Literature Review

A number of studies have been completed which investigate Inert Matrix Fuels (IMFs) [2-8] and radiation effects on material properties. In this literature review, first will introduce basic theories of thermal conductivity in ceramic materials, followed by the effects of irradiation on the structural properties of ceramic materials.

2.1 Theory of thermal properties of ceramic oxides

In theory there are two contributions to thermal conductivity, the electronic (κ_E) and lattice (κ_L) contributions. The electronic component is described by the Wiedemann-Franz law, where the ratio of thermal to electrical conductivity of a metal is proportional to the temperature; on the other hand, lattice contributions arise from lattice vibrations.

$$\kappa = \kappa_E + \kappa_L \tag{2.1}$$

For example, some solids have a high electrical resistance value, thus the thermal conductivity is dominated by lattice vibration. On the other hand, electronic conductivity via charge carrier mechanisms also plays an important role in determining the thermal conductivity.

2.1.1 Electronic thermal conductivity

The Wiedemann-Franz law states the ratio of thermal conductivity and electrical conductivity (σ) and is shown below;

$$\kappa_E/\sigma = LT \tag{2.2}$$

where, σ is electrical conductivity, T is the temperature, and L is the Lorenz number. By using the non-degenerate approximation, the Lorenz number can be written as,

$$L = \left(\frac{k_B}{e}\right)^2 \cdot \left(r + \frac{5}{2}\right) \tag{2.3}$$

r is the scattering parameter k_B is Boltzmann's constant, and e is the electron charge. For most metals the Lorenz number is a constant. However, for ceramic or semiconductor materials the positive and negative charge carriers are contained, and dipolar conduction takes place.

2.1.2 Phonon thermal conductivity

Considering Equation 2.4 which describes κ_L as the product of heat capacity (C_v), phonon velocity (v) and phonon mean free path (l_{ph}). This equation gives a rough description of the lattice vibration contribution to phonon thermal conductivity; it neglects the frequency dependence of each parameter. For parameter l_{ph}, it is related with relaxation time τ though the phonon velocity.

$$\kappa_L = \frac{1}{3} C_v v l_{ph} = \frac{1}{3} C_v v^2 \tau \qquad (v = \frac{l}{\tau}) \tag{2.4}$$

In a perfect single crystal without defects, the phonon free path would be infinite, since the thermal vibrations are harmonic at a temperature of absolute zero. However, as the temperature increases the lattice vibrations will gradually become anharmonic due to the vibration of the atoms in the crystal. The phonon free path will then be affected by both Normal processes and Umklapp processes, where the former processes conserve the phonon momentum and do not contribute to the thermal resistance directly, instead it redistributes the momentum in the phonon system. While the latter processes conserve the phonon momentum and are responsible for the observed finite thermal conductivity.

When the temperature is equal or above the Debye temperature θ_D, the Umklapp scattering is the dominant factor and the phonon thermal conductivity can be given by [9]

$$\kappa_L = \frac{(6\pi^2)^{2/3}}{4\pi^2}\frac{\bar{M}v_s^3}{T\eta^{-2/3}\gamma^2} \tag{2.5}$$

where $\bar{M}$ is the average mass per unit cell, η is the number of density of primitive unit cells, γ is Grüneisen parameter and v_s is the speed of sound. This expression is applied to a simple crystal structure, low mass contrast and is an excellent estimate for κ_L. Note that this equation also agrees with the $\kappa_L \propto 1/T$ law.

At temperatures below θ_D, the phonon thermal conductivity $\kappa_L$exponentially increases with $1/T$. When the temperature approaches absolute zero, $\kappa_L$decreases with T^3.

However, in addition to the Normal processes and Umklapp processes, the limitations of the thermal conductivity in a real crystal are mainly contributed by point defect scattering (τ_d^{-1}, inclusions induced lattice distortion or lattice imperfection), boundary scattering (τ_b^{-1}, mostly in nanostructure materials), and phonon-phonon scattering (τ_p^{-1}, including normal process and *Umklapp* process), as shown in Equation 2.6

$$\tau^{-1} = \tau_p^{-1} + \tau_d^{-1} + \tau_b^{-1} \tag{2.6}$$

At temperatures above θ_D in a real crystal, the Umklapp process is often the dominant scattering effect. Eric et al.[9] have emphasized the universality for $\tau_U(\omega) \propto \frac{\bar{M}v^3}{V^{1/3}\omega^2\gamma^2T}$ the Umklapp process depends strongly on the an-harmonicity of the bonding (Grüneisen parameter, γ), average mass ($\bar{M}$), and temperature (T).

Boundary scattering in polycrystalline materials is particularly effective in nanostructured materials, it depends on the grain size d and v_g, descried in Equation 2.7 [10, 11]. While it is most notable at very low temperature ($T \ll \theta_D$).

$$\tau_b^{-1} = \left(\frac{d}{v_g}\right)^{-1} \tag{2.7}$$

Within crystalline semiconductor material, point defect, vacancy, and dislocation are the major factors contribute to the τ_d^{-1}.

$$\tau_d^{-1} = \frac{V\omega^4}{4\pi v_p^2 v_g}\left(\sum_i f_i\left(1-\frac{m_i}{\bar{m}}\right)^2 + \sum_i f_i\left(1-\frac{r_i}{\bar{r}}\right)^2\right) \tag{2.8}$$

The f_i is the atoms fraction with mass (m_i) and radius (r_i), $\bar{m}$,and $\bar{r}$ indicate the average mass and radius, respectively [12, 13]. Equation 2.8 can only apply for the defects that are smaller than the phonon mean free path. On the other hand, the defects larger than the phonon wavelength will be considered in other factors [14].

The scattering mechanisms are highly dependent on the frequency of different populations of phonons. Toberer et al. [9] have shown the frequency dependence on phonon scattering (Figure 2.1). Usually, high frequency phonons are caused by point defect and Umklapp scattering, and low frequency phonons are contributed by boundary scattering. The dashed line effective τ in the Figure 2.1 represents the overall scattering mechanism.

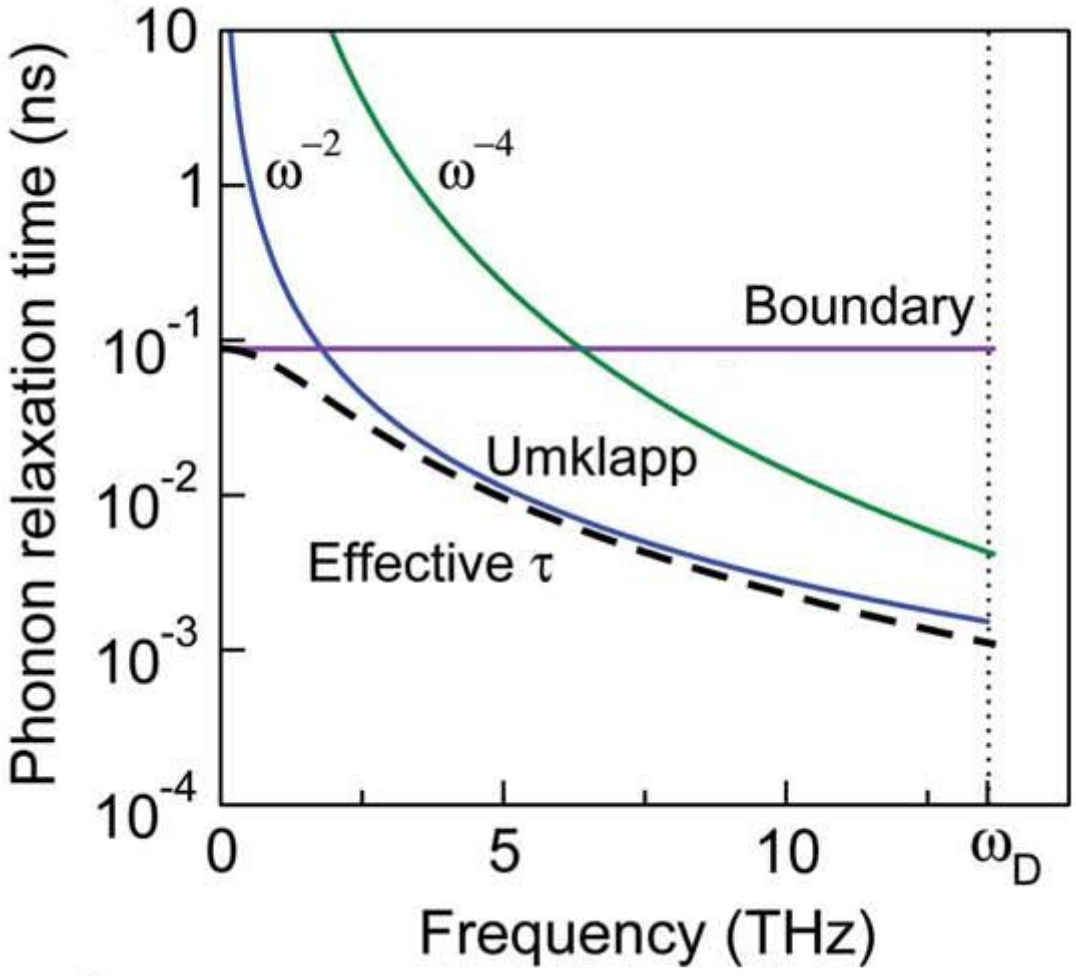

Figure 2.1 Real materials have many scattering mechanisms, which depend on frequency [9].

2.1.3 Composite materials

In the case of composite materials, the thermal conductivity is not only dependent on the individual components but also dependent on the microstructure [15]. The overall thermal conductivity of a composite material with spherical particles which are randomly distributed in the matrix can be described as

$$(1 - C_D) = \frac{\kappa_D - \kappa_C}{\kappa_D - \kappa_M}\left(\frac{\kappa_M}{\kappa_C}\right)^{1/3} \quad (2.9)$$

where κ_M, κ_D and κ_C are the thermal conductivity of matrix, dispersed phase, and composite respectively. C_D is the concentration of the dispersed phase. Miller [16] has given a more practical equation for composites, effective thermal conductivity (κ_{EFF}) is show in Equation 2.10.

$$\kappa_{EFF} = \kappa_D + (1 - V_D)(\kappa_M - \kappa_D)\left(\frac{\kappa_{EFF}}{\kappa_M}\right)^{1/3} \quad (2.10)$$

However, in practice, the composite materials can have random shapes and be randomly distributed in the matrix. Therefore, Equation 2.9 and 2.10 given the upper and lower limit for the thermal conductivity with regard to randomly distributed particles. For non-spherical particles, the estimation of thermal conductivity gets more complex, finite element modelling is required to observe the overall thermal conductivity.

2.2 Waste forms for used nuclear fuel immobilization and the physical property of material under radiation

2.2.1 Synthetic rock

The term Synroc comes from synthetic rock, invented by Professor Ted Ringwood of ANU (Australian National University) in the late 1970s. It is an advanced ceramic containing geochemically stable mineral phases which can potentially immobilise uranium and thorium for a billion years. The original form of synroc consists of mainly hollandite ($BaAl_2Ti_6O_{16}$), zirconolite ($CaZrTi_2O_7$) and perovskite ($CaTiO_3$), and it was intended mainly for immobilisation of liquid high-level radioactive waste produced from the reprocessing of fuel from light water reactors. This process to make a Synroc waste form includes mixing and calcination at 750 ℃ to produce a powder form. The powder was then compressed in a bellows-like stainless steel container or HIPed (hot isostatic pressing) at 1150 – 1200 ℃. In recent years, plutonium immobilization matrix studies

have led to pyrochlore-rich titanate ceramic with an increased loading of plutonium, natural uranium and neutron absorbers (Gd, Sm, Hf) needed for nuclear criticality control.

2.2.2 Radiation Damage and Stability

There are many interactions of radiation with solids, within the solids due to neutrons, heavy ions, protons and electrons irradiations. As a result there are atomic displacements and transmutation reactions. Considering a particle with energy (E), when it collides with a lattice atom, the energy of the energetic particle will partially transmit to the lattice structure. Therefore the maximum energy to be transferred can be expressed as [17]

$$T_{max} = \Lambda \mathrm{E} \tag{2.11}$$

$$\Lambda = \frac{4M_1 M}{(M_1 + M)^2} \tag{2.12}$$

where, M_1 is the mass of the energetic particle, M is the mass of the stationary particle.

As the incoming particle gives its energy to the lattice atom, vacancy and interstitial defects will occur in the crystal structure. The minimum amount of energy required in order to displace a lattice atom is E_d, and it depends on crystal structure and direction of displacement.

Defect production

Displacements per atom (dpa) is a parameter that commonly describes the damage which is produced by different irradiation methods. Norgett-Robinson-Torrens (NRT) model [18] is the most common used to calculate the number of atomic displacements in irradiated materials. In NRT model, the number of Frenkel pairs $\nu_{NRT}(T)$, generated by primary knock-on atom (PKA) of energy T is given by

$$\nu_{NRT}(T) = \frac{\kappa E_D(T)}{2E_d} \tag{2.13}$$

where κ is usually equal to 0.8, $E_D(T)$is the energy of the PKA lost to electron excitation. By integrating Equation 2.14 over time and recoil spectrum, gives displacement per atom (dpa) which also known as the atom concentration of displacements.

$$dpa = \iint \phi(E)\nu_{NRT}(T)\sigma(E,T)dTdE \tag{2.14}$$

where $\sigma(E,T)$ the probability of a particle with energy E will impart one recoil atom with energy T to struck atom, and $\phi(E)$ is the neutron flux.

There are two major differences of using ion beam irradiation (used in this study) to simulate the effect of α-irradiation. One fundamental difference is the particle energies due to the different particles production methods. Ions are produced in accelerators and only selected energy can be emerged in addition the energy beams are very narrow. However, on the other hand, neutron energy spectrum in the reactor has various orders of magnitude energy levels; therefore, the radiation damage done to the solids are complicated due to the multivariate source. Another major different is the depth of perpetration. Ions tend lose energy quickly due to high electronic energy loss, which triggers the non-uniform energy deposition profile [19]. The penetration distance for ion beams is from 0.1 to 100 μm.

Influence of experimental conditions on irradiated microstructure

There are several key experimental factors that will influence the irradiated sample, such as irradiation dose, irradiation temperature, and dose rate of the implanting ion. The material that is being analysed will behave differently, if the atomic weight, crystal

structure and atomic bonding vary. In this study, the focus is more on the materials side than the experimental conditions. However, all aspects will be discussed.

- Experimental conditions
    - Irradiation dose

This was introduced in the Defect production section already, where dpa is a useful parameter to compare the displacement damage levels in many irradiation conditions. This parameter is very important to quantify the effects in irradiated materials, and is very effective in correlating the initial damage production levels over a wide range of materials [20].

    - Irradiation temperature

Different irradiation temperatures have great influence on microstructural evolution of irradiated materials. The influence is related to migration of point defects. There are several major temperature regimes that were found in the early experimental studies which were focused on the isochronal annealing electrical resistivity measurements on metals irradiated near absolute zero temperature.

    - Dose rate

At very low temperature, near absolute zero, the damage accumulation is independent of dose rate, since point defect migration does not occur. However, as the temperature increases to the point where point defect migration has occurred, the damage rate can have a significant influence on the damage accumulation. The irradiation temperature starts to increase from absolute zero, the linear dependence of defect accumulation and irradiation fluence will transit to square root dependence. Similarly, the critical dose of

amorphization is independent of dose rate near absolute zero temperature, and becomes inverse square root dependence when at elevated temperature.

- Various physical properties of the target material
    - Atomic weight

Materials with light atoms tend to have more spatially diffused displacement cascades than heavy atoms, due to the increase in nuclear and electronic stopping power with increase atomic weight. However, there is not a universal relation between atomic weight and microstructural parameters such as overall defect production, defect cluster yield or visible defect cluster size [20].

- Crystal structure

The effect of crystal structure in these studies is partially explained by using the structural-topology-based model that Hobbs [21] proposed. According to the model, the susceptibility to amorphization (at absolute zero temperature) is governed by the connectivity of the cation polyhedra. In another words, materials have high topological connectivity for the cation polyhedra are resistant to radiation induced amorphization.

- Atomic bonding

Atomic bonding, such as metallic ionic, covalent and polar covalent, is a potential factor to consider in these studies. In ceramic oxides, atomic bonding can directly or indirectly affect point defect migration and annihilation mechanisms like introduction of recombination barriers, and thereby result in different microstructure behaviours under radiation.

Radiation induced effects on microstructure

In general, energetic particles deposited into a material would create atomic displacements which can induce microstructural change due to the crystalline to amorphous phase transformation. Thus a high concentration of point defects (as well as voids) or solute segregation (as well as precipitation) where generated in crystalline lattices. Correspondingly, the physical and mechanical properties of the materials may undergo degradation.

- Amorphization

Amorphization normally occurs at very low temperature when self-interstitial atom (SIA) is limited, and major swelling may occur (5-30%), with reduction of elastic moduli [22, 23]. This crystalline to amorphous phase transition generally occurs for damage levels of ~0.1 – 1 dpa at low temperatures in ceramics. There are several mechanisms that may lead to this amorphization, including direct amorphization within collision cascades, increase in crystalline free energy caused by point defect accumulation, and disordering processing [24, 25]. In general, amorphization in ceramics occurs homogeneously or heterogeneously, becomes more difficult with increasing temperature and occurs only below a critical temperature.

Homogeneous amorphization is normally associated with a progressive defect accumulation due to accumulation of point defects or a specific defect type [26]. Homogeneous amorphization is important for electron irradiation. On the other hand, heterogeneous amorphization processes are for ion irradiation in the majority of ceramics, such as α–decay. This heterogeneous amorphization is mainly associated with: first direct impact amorphization within an individual collision cascade and second local accumulation of high defect concentrations due to the overlap of collision cascades [26].

- Thermal conductivity degradation

For a pure metal thermal conductivity degradation is mainly caused by the electron scattering from point defects & defect clusters and nuclear transmutation to solute atoms. The degradation can occur over a wide range of irradiation temperatures. Thermal conductivity for metals and ceramics decreases significantly (greater than 10% for high conductivity materials) [27, 28]. For non-metallic irradiated materials, the thermal conductivity is typically degraded by displacement damage due to phonon scattering by point defects [28].

- Segregation and precipitation

This can happen at intermediate temperature when SIA are movable, where part of the SIAs diffuse in point defect sink structures such as grain boundaries, intrinsic vacancies, and free surfaces. The solute atoms can preferentially couple with point defects (formed during irradiation), resulting in either enhancement or depletion of solutes at the point defect sink structure. This solute-defect coupling will influence the point defect diffusion kinetics, and the solute enrichment or depletion may strongly affect the local composition and form new phases.

For ion beam irradiation, the ions from the beam can break the relative balance of SIA compared to vacancies flowing to defect sinks. The injection of ions can act as additional interstitial atoms which will suppress void nucleation and growth [29, 30].

- Dimensional instabilities

Irradiation growth is due to anisotropic growth of dislocation loops on different planes. Anisotropic growth in polycrystalline materials can result in large grain boundary stress and finally to fracture. Figure 2.2 shows BeO near room temperature under irradiation

resulting in large anisotropic lattice parameter changes [31]. In the figure, where the neutron fluence is above $2 \times 10^{20} cm^{-2}$ (~ 0.2 dpa) an α-axis expansion of ~0.1%, and c-axis expansion of greater than 0.5% was observed, resulting in a rapid decrease in flexural strength [32].

Volumetric swelling normally occurs at temperatures below recovery temperature due to the formation of voids, and typically a linear relation with increasing dose is observed. MgO was one of the first few refractory materials studied, it has very good irradiation stability under neutron irradiation, also it has been reported that the swelling is about 0.3% for polycrystalline MgO at 430 K following a 30 dpa dose [33]. Furthermore, annealing of MgO at 1273 K leads to significant recovery (60%) of the radiation damage.

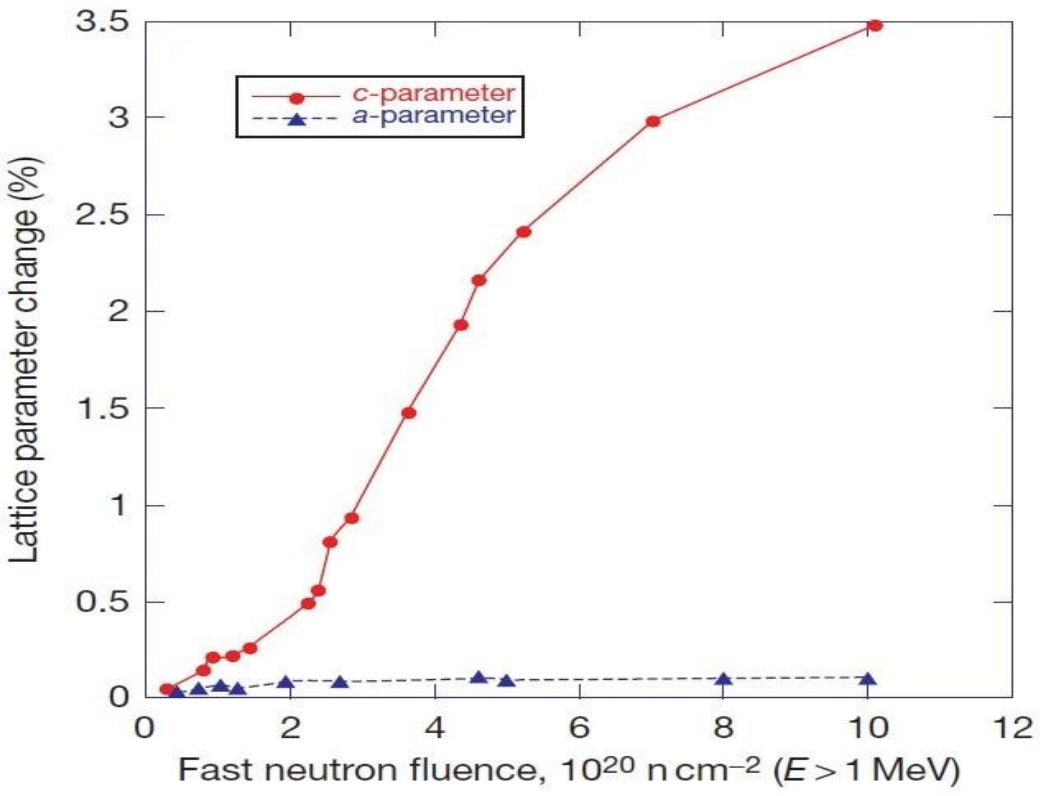

Figure 2.2 Effect of fission neutron irradiation near 75 ℃ measurement of BeO lattice parameter changes. Reproduced from [31].

2.2.3 Thermal spike model for formation of amorphous defects

This basic assumption in the thermal spike model was proposed by Seitz and Kehler [34]. It is that around the injected ion there is a high temperature region formed in the material which is created by the electronic energy loss of the injected ion. The temperature starts to rise in a few tens of Pico seconds, and the temperature will keep increasing after the ion passes though the lattice site. The time needed for the energy transfer from the injected ion to the excited electron is quicker than the time of lattice vibration. Therefore, the electronic energy loss from the injected ion will transfer to the excited electrons, and convert to thermal energy in a localized region. The time of the energy transfer from the excited electrons to the lattice of ions depends on the material, such as metallic, semiconductor, or ionic [35].

The local temperature may surpass the melting point of the material as for example, in UO_2 (with T_m = 3150 K). Phase changes and defect formation may accompany the rapid heating and quenching of the lattice. The approximation of maximum radius of amorphized region along the injected ion tracks is to assume the entire region of the heat effected zone where the temperature rises to or above the melting point becomes amorphous [26]. However, the molten region does not all become amorphous; instead, some epitaxial regrowth occurs during the cooling period. Thus the amorphous region is smaller than the original molten zone [26].

2.3 Candidate Materials for Inert Matrix Fuels

The choice of IMF is heavily depending on the reactor system and also the application. For example, in multi-recycle system, plutonium burn up is not important as the fuel reprocesses and refabricate into new fuel. On the other hand, once through cycle for

destruction of plutonium is required that the fuel is capable for high burn up and low solubility in groundwater under repository condition due to the safety storage in long term. The choice of matrix material is depending on factors including melting temperature, thermal expansion, responses to the neutron irradiation and fission fragment implantation in the fuel matrix, also chemical durability with respect to the fuel, coolant and clad, neutron absorption cross section, resistance to corrosion, degradation of strength and thermal conductivity during irradiation.

2.3.1 Heterogeneous fuels

Generally, heterogeneous fuels consist of a distribution of either metal or ceramic particles embedded in a metal or ceramic matrix, and the main categories are listed as below.

Cercer dispersion fuels

Cercer dispersion fuels are consisting with macro or microscopic dispersion of fissile phase in ceramic matrix. Cercer fuel is heavily depending on the microstructural characteristic of the fuel. In order to optimizing fuel behaviour of microstructural verities as it through reactor; macro-dispersion maintain the thermal conductivity and structural orderliness of the fuel matrix under radiation which suffer a large amount of fissile phase particles; micro-dispersion consist fine distributed fissile phase into neurotic inert matrix.

There is wide range of choices for ceramic matrix including oxide, carbide, and nitride ceramics as binary, ternary and higher compounds [6], for instance, a dispersion of PuO_2 particles (100 μm) in MgO. Recent work focusing on the plutonium burning [36], out-of-pile characterization, and irradiation testing of uranium contained fissile surrogate for plutonium fuel using cercer concept [4, 37-39].

There are several recent experiment tests on irradiation of cercer fuel. The investigations of candidate inert matrix material such as MgO $MgAl_2O_4$, Al_2O_3, and $Nd_2Zr_2O_7$ have been carried out [33, 40, 41]. In general, all tested IM are performed accredited at fast neutron fluence (>0.1 MeV) of $1.95 \times 10^{26}\, m^{-2}$, however, Al_2O_3 showed 4% of volume swelling. For micro and macro-dispersions of UO_2 of MgO has shown different fuel behaviour [42]. In the experiment, the swelling and restructuring of micro-dispersion greater than macro-dispersed specimens, on the other hand, macro-dispersed specimens showed matrix cracking. The irradiation experiments in EFTTRA-T3 have investigated MgO, CeO_2, $MgAl_2O_4$ and Y_2O_3 with and without loading of UO_2 (2.5 vol. %) [43]. The performance of UO_2-$MgAl_2O_4$ showed unsuitable as fuel in experiments. MgO, CeO_2 and Y_2O_3 fuel specimens, showed low swelling and fission gas release (3-8%), and CeO_2 and Y_2O_3 exhibiting showed less matrix cracking, suggesting that the matrices may undergo plastic deformation under irradiation in order to accommodate the swelling. Ceramics in general is brittle, therefore care must be taken which thermal and mechanical stress appears in the matrix will not exceeding the elastic limit of the fuel itself, otherwise cracking of fuel matrix can be emerged.

Cermet dispersion fuels

The advantage of using cermet dispersion fuel is its robust behaviour under irradiation. Between late 1950's and early 1960's there are a large number of work have been done force on cermet fuels, it acts as oxide pellet fuel in fast and light water reactors. In reactors, it is found that the cladding is often metallurgically bonded to matrix; the absence of a fuel to cladding gap dramatically Improves fuel to coolant heat transfer and lowers fuel centreline temperature [6]. A barrier is needed to prevent the reaction of matrix and the fuel particle. Cermet fuels have shown high burn up capability, the fuel burn up lifetime is inverse proportion to fuel temperature. Aluminium matrix cermet fuels (including

silicides, oxides) have been established, it is test with high powder density (up to 500 W/cm^3) to high burn up. Thurber summarized data on dispersions of UO_2 particles in stainless steel matrices available at about 1964 as a function of fuel surface temperature and fission density [44].

In the system which uses burnable poison to control the reactivity, plutonium oxide as the dispersed fuel phase (loading range of 6-12 Vol. %) for plutonium burning application. Erbia and gadolinia can add in the system as burnable poison for reactivity control, these burnable poison can either in solution with the fuel particle or as a separate phase. Former studies have forced on the application of cermet to Pu-burning in LWR [45], irradiation testing of aluminium matrix dispersion of UO_2 as fuel of LWRs. Corrosion resistance of aluminium clad fuels is improved by silumin (AlSi) in LWR.

Metmet dispersion fuels

The fissile metal dispersed in aluminium matrix fuel has been extensively tested. For example, Pu-Al alloy fuels (dispersion of $PuAl_4$ precipitates in aluminium matrix, due to the low solubility of Pu in aluminium), have been test over hundred time of irradiation test and high burn up (90% burn up) test. Although some promising results is obtained, due to its low melting temperature of aluminium, and corrosion of aluminium matrix by coolant, the application of this type fuel is been limited.

There are several suggestions to use aluminium alloy dispersion fuel as IMF. The advantages of this type fuel include low fuel centreline temperature, very high burn up, environmentally friendly fabrication process of fuel rods. Zirconium brazing alloys have melting temperature of 690 to 860℃ and as it melt they penetrate fuel particle joints and ensure the metallurgical contact between both cladding and fuel component [6].

Zirconium brazing alloy used in IMF will enhance thermal conductivity and ensure satisfied bond to fuel cladding.

2.3.2 Radiation behavior of MgO-$Nd_2Zr_2O_7$

In order to investigate the behaviour of MgO-$Nd_2Zr_2O_7$ fuel in reactor, radiation behaviour studies are required. Recent researches concerned the crystal to amorphization at different dose element, dose rate, and energy; critical amorphization temperature; and phase transformation [40, 46-48].

Ion beam irradiation is one process to simulate the radiation damage processes in the matrix. The ionic radius ratio (r_A/r_B), of A- and B-site cations are used to predict the stability of pyrochlore under heavy-ion irradiation [49]. The cation antisite defect is the most stable defect in pyrochlore, and as A-site cation have similar radius as B-site cation, the materials will preference to accommodating the antisite cation. Thus, low cation ionic radius ratio will more favour to forming disordered structure. For example, ionic radius of Sn^{4+} is midway between the ionic radius of Ti^{4+} and Zr^{4+}, the critical amorphization dose at room temperature and critical temperature (T_c) for $Gd_2Sn_2O_7$ ($r_A/r_B = 1.526$) and $Gd_2Ti_2O_7$ ($r_A/r_B = 1.74$) are ~3.4 dpa 350K and 0.2 dpa and 1120K [50].

Although the ionic size of cations is an important role in determine the radiation response for varies types of pyrochlore compositions, the r_A/r_B ratio alone cannot be used to precisely predict the radiation tolerance characteristics. There are several violations of cation ionic radius ratio criteria in determining crystal chemistry such as 48f oxygen positional parameter x and radiation resistance [47]. For instance, $Nd_2Zr_2O_7$ has the ionic radius ratios equal to 1.54 and it cannot become amorphization at 25K, on the other hand where the critical amorphization temperature for $Gd_2Sn_2O_7$ is about 350K and it have cation ionic radius ratio of 1.526. The 48f oxygen positional parameter (x) is defining the

polyhedral distortions and deviation from the ideal fluorite structure; also it is affected by the cation ionic size of A- and B-sites [51]. Table 2-1 have shown some literature data of structural parameters and irradiation results for $A_2B_2O_7$ pyrochlore. Comparing the data from the table, with an increasing "x" value and an increasing degree of structural disorder where the crystal structure is close to the fluorite structure, therefore pyrochlore will have greater tendency having an order-disorder transition, and resulting more radiation tolerant.

Table 2-1 Structural parameter and irradiation results for $A_2B_2O_7$ under 1 MeV Kr^+ ion irradiation. Zirconate pyrochlore are irradiated by 1.5 MeV Xe^+[47].

Composition	r_A/r_B	O_{48f} x parameter	T_c(K)
$Sm_2Ti_2O_7$	1.78	0.327	1045
$Eu_2Ti_2O_7$	1.76	0.3267	1080
$Gd_2Ti_2O_7$	1.74	0.3263	1120
$Tb_2Ti_2O_7$	1.72	0.3281	970
$Dy_2Ti_2O_7$	1.7	0.3275	910
$Y_2Ti_2O_7$	1.68	0.33	780
$Ho_2Ti_2O_7$	1.68	0.3285	850
$Er_2Ti_2O_7$	1.66	0.3278	804
$Yb_2Ti_2O_7$	1.63	0.33	611
$Lu_2Ti_2O_7$	1.61	0.3297	480
$La_2Zr_2O_7$	1.61	0.333	310
$Nd_2Zr_2O_7$	1.54	0.335	defect fluorite at 25K
$Sm_2Zr_2O_7$	1.5	0.342	defect fluorite at 25K
$Gd_2Zr_2O_7$	1.46	0.345	defect fluorite at 25K

$La_2Sn_2O_7$	1.68	0.3294	1025
$Nd_2Sn_2O_7$	1.607	0.3322	850
$Gd_2Sn_2O_7$	1.526	0.3348	350
$Dy_2Sn_2O_7$	1.488	0.3372	amorphization at 25K
$Ho_2Sn_2O_7$	1.471	0.3366	amorphization at 25K
$Y_2Sn_2O_7$	1.477	0.3369	defect fluorite at 25K
$Er_2Sn_2O_7$	1.455	0.3375	defect fluorite at 25K

Lutique et al [48] have investigated the radiation stability of $Nd_2Zr_2O_7$ against fission products using iodine irradiation (120 MeV). The SEM results indicate there is a smoothening of the surface compare to un-irradiated surface, however no significant swelling has been observed, and with higher fluence irradiation, XRD analysis observe a new phase which be identified. Sattonnay et al [40] studied the phase transformation and recovery process due to annealing using electronic excitation (S_e) and ballistic process (S_n) with heavy ions energy of ~1 GeV, ~100 MeV, and a few MeV. From their results, in S_e regime there is also amorphization at highest fluence, anion-deficient fluorite phase transition occurs and in S_n regime there is only anion-deficient fluorite phase is formed at dose of 40 dpa, the damage recovery is done in two steps: (i) anion-deficient fluorite structure formed at 325°C; (ii) stable pyrochlore phase is recovered at 1300°C.

2.4 Immobilization of Spent Fuels

The immobilization and long-term disposal of nuclear wastes have become a significant challenge. There are various types of high level nuclear wastes generated from nuclear operations, mainly spent fuel, liquid from reprocessing spent fuels and waste arising from the production of nuclear weapons, also weapon grade plutonium from dismantled

nuclear war-heads. One way to dispose of these high level nuclear wastes is to process them into dense refractory solids (waste forms) which can survive a long period of time underground (e.g. U & Th containing minerals monazite and zircon). Over the past several decades, synthetic rock (Synroc) waste forms have been studied as nuclear waste host phase materials, because these types of natural minerals often contain uranium and thorium. For example, pyrochlore [52], and zirconolite [53], are both ideal host phases for Pu, U and actinide immobilization. In recent years zircon ($ZrSiO_4$) [54] and monazite ($REEPO_4$, where REE are rare earth elements) [55] (ABO_4), and zirconium-based materials with fluorite or defect fluorite structures have also been extensively studied. These materials have excellent resistance to α-radiation induced amorphization and excellent chemical durability [22, 56-58]; however, little work has been done on other compounds in the ABO_4 family which regard to radiation tolerance.

The ABO_4 family has a crystal structure consisting of A cations surrounded by isolated BO_4 (B = P, Si, V, and Nb) tetrahedra, and numerous structures of ABO_4 are found. Further, these are polymorphic at normal atmosphere with different structures at higher pressure. There are mainly four structure types, monazite (monoclinic, P21/n), zircon (tetragonal, I41/amd), scheelite (tetragonal, I41/a), and fergusonite (monoclinic, I2/c). The strong tetrahedral bonding of B-O provide eight-fold (tetragonal) or nine-fold (monoclinic) coordination around the A atoms [59]. The structures show various combinations of valence for both A- and B-site atoms such as I-VII, II-VI, and III-V groups. There are many studies on the phase transformations of these structures [60-63]; the pathways from one structure to another have been summarized by Aldred [59] with, pressure, temperature, preparation techniques and changes in A and B site atom size. As a nuclear waste host material, the potential phase changes (loss in crystallinity and amorphization) of these compounds can affect the durability over the long term.

The crystal structures of ABO_4 type compounds at normal pressure have been studied by Seifert and Bastide [64, 65] who also provide a classification diagram of the crystal structures for ABO_4 based on the ratio of r_A/r_O vs r_B/r_O. There are many studies on different A-site atoms of zircon, and monazites using ion beam irradiation or the doping of actinides [22, 57, 66-69]. The most studied ABO_4 compounds were zircon (tetragonal) and monazites (monoclinic) and these respond differently to ion irradiation. Meldrum et al. [22] have studied actinide induced radiation damage in zircon (natural and synthetic) and monazite. In their studies, α-decay damage in natural monazite phosphates has shown three amorphization stages from crystalline → isolated amorphous zones → polycrystalline → complete amorphization; however, the ion beam irradiation on synthetic monazite and zircon have shown to follow a damage-accumulation pathway; also monazite cannot be amorphized by 800 KeV Kr^+ ions at temperatures greater than 175 ℃; whereas zircon can be simply amorphized at temperatures up to 740 ℃ [22]. Meldrum et al. [69] have also described the effect of structure variations of zircon and monazite on ion beam irradiation (Kr^{2+}, 800 KeV) using Hobb [21] model, and according to the model the susceptibility to amorphization is governed by the connectivity of the cation polyhedra. However very little work has been undertaken to investigate other B cations in this system. Lu et al. [70] investigated the radiation tolerance of varying B-site compositions of vanadate-phosphate fluorapatites. By changing the PO_4/VO_4 ratio at the B-site, they concluded that the reduction of radiation stability upon substitution at the B-site was attributed to a decreasing of ENSP (electronic-to-nuclear stopping power) ratio. The importance of the ENSP ratio is that the ionizing radiation in certain energy ranges appears to promote defect recombination in many ceramic oxides [69].

2.5 Summary

This chapter provides an overview of well-established thermal conductivity theories and radiation related structure stability theoretical background, as well as candidate fuel materials in the nuclear applications and the candidate immobilization materials for spent fuels. The material fabrication method and characterization techniques will be discussed in the next chapter.

3. Experimental Procedures

3.1 Characterization of synthesized of samples

X-Ray Diffraction (BRUKER D8 Advance diffractometer) was employed for structural and phase identification, utilizing Cu Kα radiation over a 10-80° 2θ range, with a step size of 0.02 °and a counting time of 20s per step. The XRD patterns were refined using a Rietica program (version 2.1) [71], and the Le Bail method [72]. The peak profiles were approximated by a Pseudo-Voigt function. The lattice parameters were refined by gradually adding the parameters and the peak shape was calculated by continuously modelling graphics until the R factor reached a stable low number. For irradiated samples, Grazing incidence X-ray diffraction (GI XRD) was used to characterize only the top layer of the ion irradiated sample surface. The diffractometer was fitted with an incident beam Gobël mirror and a 0.18 parallel-plate collimator for parallel beam conditions. A set of incident angles (1°, 2°, and 4°) was tested; the maximum extinction of X-rays was satisfied when the incident angle is at 4°. The scan range was 15-60° 2θ and the step size was 0.03 °with a counting time of 20s per step.

Scanning Electron Microscopy (SEM) was undertaken with a Zeiss Ultra Plus SEM with an Oxford Instruments X-Max 80 mm^2 SDD X-ray microanalysis system. The operating power was 15 KV, and samples were analysed for microstructural and phase composition. Samples were mounted in an epoxy resin and polished to a 1 μm diamond finish and coated with a thin film of carbon on top of the polished surface. All images were captured in SEM using backscattered electron channelling contrast imaging with an ASB (angular selective backscatter) detector [73].

A JEOL JEM 2200FS (JEOL Ltd., Akishima, Tokyo, Japan) transmission electron microscope (TEM), equipped with a field emission gun (FEG) electron source operated

at 200 kV and in-column Omega filter electron energy loss spectrometer (EELS), was used to estimate the crystallite size and elemental distribution. TEM images were recorded with a CCD camera (Model 894 Ultrascan 1000, Gatan, Pleasanton, CA) mounted below the Omega filter. Samples for TEM were prepared by suspending crushed powder in ethanol and depositing several drops on a holey carbon coated 200-mesh copper grid.

Raman spectra were undertaken using a Renishaw inVia Raman spectrometer equipped with an Argon ion laser (514nm) and a Peltier cooled CCD detector. Raman spectra were collected in the range of 100-1100 cm^{-1} with a spectral resolution of about 1.7 cm^{-1} for the 1800 l/mm grating. The spot size was about 1.5 μm for x50 magnification.

3.2 Characterizations of thermal properties

In order to determine the thermal conductivity; there will be three measurements was undertaken. Simultaneous Thermal Analysis (STA), Dilatometer (DIL), and Laser Flash (LFA). Thermal conductivity is thus a material specific property used for characterizing steady heat transport. It can be calculated using the following equation:

$$\lambda(T) = \rho(T) * C_P(T) * \alpha(T) \qquad (3.1)$$

Where λ: Thermal conductivity ($W\ m^{-1}K^{-1}$)

α: Thermal diffusivity (m^2s^{-1})

C_p: Specific heat capacity ($J\ Kg^{-1}K^{-1}$)

ρ: Density ($Kg\ m^{-3}$)

Density can be calculated by the following equation:

$$\rho = \frac{\rho_0}{\left(1 + \frac{\Delta L}{L_0}\right)^3}$$

Where $\frac{\Delta L}{L_0}$ is the linear thermal expansion coefficient which can be calculated from dilatometry.

In the following paragraphs each instruments will be described, including its features, how they operate, and what method was used to calculate the thermal diffusivity and specific heat capacity.

3.2.1 Simultaneous Thermal Analysis (STA)

NETZSCH STA 449 F1 can measure the thermal gravity for mass change behavior simultaneously with differential scanning calorimeter which gives heat flow behavior as well as the mass change. The furnace was Pt/Rh, with an operating temperature range of room temperature to 1500℃, and a platinum thermocouple (type S with temperature range from RT to 1650℃) is used for TGA, TGA-DSC (C_p) measurements, the sample crucibles are also platinum. Also, STA can work under different atmosphere environment (e.g. argon, oxygen, nitrogen, helium).

In this work, STA was used to determine specific heat capacity of samples, and only DSC is employed. In order to have accuracy results, first the working principle of the DSC needs to be understood. The DSC measures specific heat capacity by heating the sample and measuring the temperature difference between the sample and a reference. The sample state is shown in Figure 3.1. The sample will be placed in the center of the crucible and keep reference crucible empty. The furnace is directly heated to the center, and the temperature is detected by thermocouples. There is one thermo-element shared with the crucibles, it allows exchange from temperature to voltage which detects the difference between two crucibles. The voltage is usually in microvolt (μv).

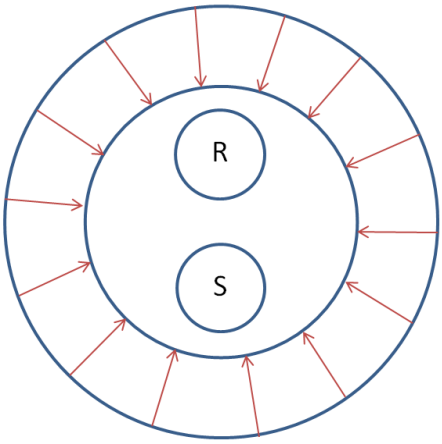

Figure 3.1 Drawing of sample place geometry (R = reference, S = Sample)

In general, the specific heat (C_P) indicates the amount of energy required to heat one gram or one mole of a material by one Kelvin at the constant pressure. For calculation of specific heat there are three basic measurements needed (baseline, reference, and sample). The following equation shows how those three measurements are related.

$$C_p = \frac{\text{Signaldifference (Sample} - \text{Baseline)}}{\text{Sample mass} * \text{Heating rate} * \text{Sensitivity}} \quad (3.2)$$

The sensitivity is calculated based on the reference sample measurement (usually use sapphire as reference sample).

$$\text{Sensitivity} = \frac{\text{Signaldifference(Reference} - \text{Baseline)}}{\text{Mass (Referecne)} * \text{Heating rate} * \text{theoret.}\, C_p\ \text{(Reference)}} \quad (3.3)$$

For the experiment, DSC measurement was undertaken from room temperature up to 1400°C for a few milligram of powder, in a 50 ml/min argon flow with a heating rate of 10 k/min. Sapphire (Monocrystalline Alumina) was used as a standard reference sample and Pt crucibles have been employed. The results, Ratio method was applied to determine specific heat. This method could determine individual C*p* values at different temperatures, and it was described by the following equation:

$$C_p^S(T) = \frac{m_R}{m_S} * \frac{\Delta V_s(T)}{\Delta V_R(T)} * C_p^R(T) \quad (3.4)$$

Where C_p^S and C_p^R are sample specific heat and reference sample specific heat, m_S and m_R are the masses of the sample and reference standard, respectively; and $\Delta V_s(T)$ and $\Delta V_R(T)$ are the voltage differences between the sample/reference curves and the baseline (units in micro volte), respectively. It was worth to mentioning that the Ratio method assumes the experimental conditions in the three runs are the same. In another words, consistent baseline was very important in order to have the most accurate Cp value.

3.2.2 Dilatometer (DIL)

There were many applications of DIL such as linear thermal expansion, coefficient of thermal expansion, shrinkage expansion, sintering temperature/sintering step, and density change. In my experiment I only focused on the linear thermal expansion. A NETZSCH DIL 402C was used for measuring thermal expansion of the samples. It can determine very small dimensional changes within the range from 0.125 nm to 1.25 nm as a function of temperature. The degree of linear expansion was defined as the fractional change in length per degree of temperature change. It can be expressed as following equation:

$$\alpha = \frac{1}{L_0}\left(\frac{\Delta l}{\Delta T}\right) \quad (3.5)$$

Where, α coefficient of expansion; L_0 initial sample length; Δl change in length; ΔT change in temperature.

The Dilatometer DIL 402C employed a high-resolution displacement transducer Vacodil® measuring system; the application temperature range was from -180℃ to 1680℃ (alumna sample carrier); also it had the viability of high vacuum atmosphere (10-4 mbar) and the ability to measure under different gas environments; the sample

temperature controller (STC), control system, can provide sample temperature control and make sure the temperature in the furnace was uniformly distributed.

The operation system of DIL 402C was very important to understand. The general top view of the furnace and the sample holder is shown in Figure 3.2, where the sample was at the end of the sample holder connected with a pushrod, and the movable furnace was surrounding the sample holder. The linear variable displacement transducer (LVDT) system was utilized to measure the sample length at different temperatures. During the testing, a force was applied on the sample (standard: 15 cN to 45 cN) when sample expanses the LVDT core is moved, and an output signal was recorded at every temperature in Kelvin. The temperature is controlled by the thermocouple near the heating element of furnace or next to sample.

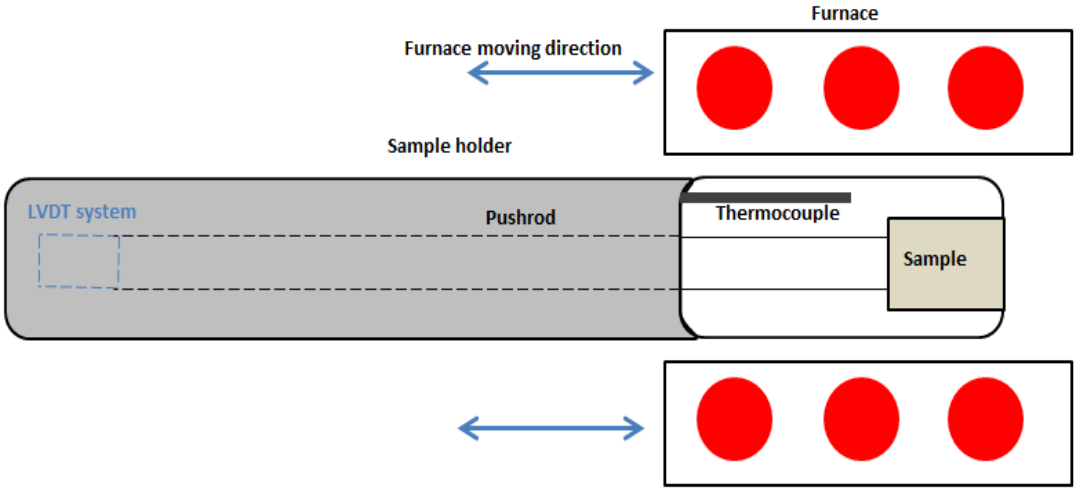

Figure 3. 2 Drawing of sample holder and furnace

The measurement temperature range was from RT to 1200℃, the heating rate was 5 K/min, and argon gas flow into the furnace was at a flow rate of 50 ml/min. In order to obtain accurate data, a correction of the pushrod was needed to estimate the error, because

during the heating the pushrod and the sample holder was exposed in the same temperature as the sample, and the output single was the sum of the sample, sample holder and pushrod.

3.2.3 Laser Flash

There were several methods of measuring the thermal diffusivity, such as laser flash method, thermal wave interferometry method and also thermo-graphic techniques. Among these methods the laser flash method has been most frequently used.

Figure 3.3 illustrates the laser flash system. The sample carrier was located inside the furnace and a cap covered the sample (prevents the laser energy from impinging directly on the detector). As the furnace heats up the sample chamber and the sample reach the expected temperature, a laser pulse was deployed onto the surface of the sample and the sample will absorb the burst energy and give a rise to heat. Subsequently, on the other side of the sample surface a slight temperature increase occurs and the temperature increase of the sample surface was measured by IR detector as a function of time. Under the adiabatic conditions, the thermal diffusivity D can be measured by:

$$D = 0.1388 \frac{l^2}{t_{1/2}} \tag{3.6}$$

Where l is the sample thickness and $t_{1/2}$ is the time required for the rear surface to reach half of the maximum temperature.

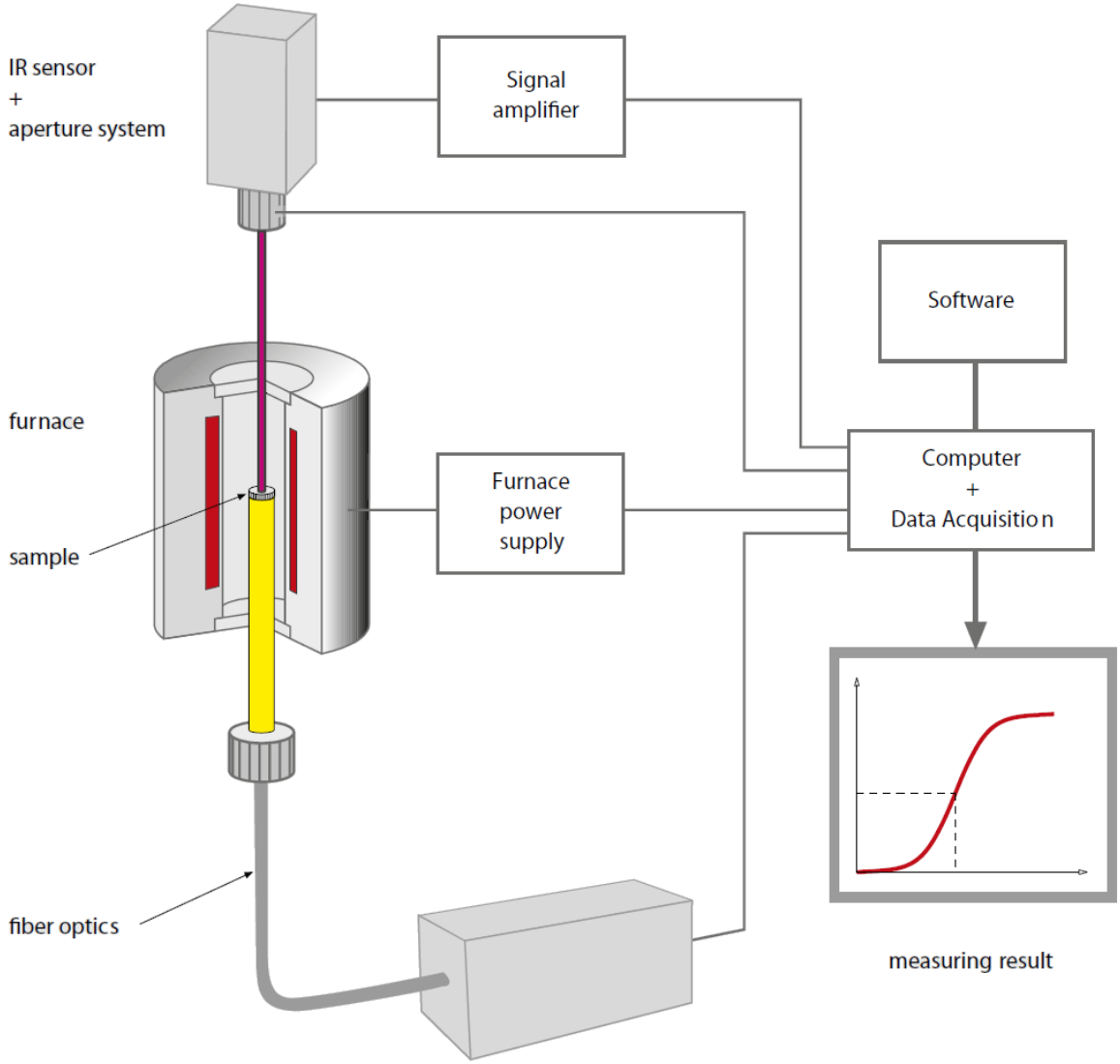

Figure 3.3 The laser flash system

For the present experiment, the samples were sintered and shaped into pellets with diameter of 10 mm and placed onto an Al_2O_3 sample holder with a SiC cap cover. The samples were heated up with a rate of 10 K/min and measured from 100℃ to 1400℃ with 100℃ temperature steps, and each temperature step had three laser pulses to determine consistency. The gas atmosphere employed was helium gas which used for furnace chamber and argon was used for sample chamber.

4. Novel Synthesis and Thermal Property Analysis of $MgO–Nd_2Zr_2O_7$ Composite

4.1 Introduction

The global stockpiles of plutonium were estimated to be around 505 tons at the end of 2014 and grows steadily, and they represent a proliferation concern [1]. Inert matrix fuel (IMF) materials offer the advantage of burning surplus plutonium and other minor actinides (MA) produced from the fuel cycle in current light water reactors with minimal production of further actinides [74, 75]. In an IMF, plutonium (or other MA) is embedded in a uranium-free matrix so as to burn it without breeding any new plutonium by neutron capture in U-238 [76]. This concept of actinide burning uses a non-fertile matrix such as ZrO_2 to provide a more efficient consumption of plutonium compared to that in mixed uranium and plutonium oxide fuel (MOX). Potentially this once-through cycle U-free IMF strategy utilizes the energetic value of plutonium as well as reduces the radiotoxicity and proliferation risk of nuclear waste. There is extensive literature on various materials for use as IMFs for burning plutonium [77-79] and candidates to be used as IMF materials must meet strict material performance requirements. These include high temperature stability, irradiation stability, high thermal conductivity, low neutron capture cross-section for the non-MA elements, good resistance to corrosion in hot aqueous solution, and good compatibility with reactor coolant [49, 80, 81]. The centerline temperature of the composite IMF pellets for this application would be expected to be in the 1000-1500 ℃ range. A composite material of magnesia (MgO) and pyrochlore structured ceramic ($A_2B_2O_7$) is a leading candidate among those oxides studied for use as IMF materials [75, 79, 82-87]. MgO possesses a high melting point (2827 ℃), high thermal conductivity (13 W K^{-1} m^{-1} at 1000 ℃), good neutronic properties, and good radiation resistance [88], however it cannot incorporate plutonium or MA within its crystal

structure. Pyrochlore ($A_2B_2O_7$) is a corrosion resistant [89], radiation tolerant phase [90] capable of incorporating plutonium and MA within its crystal structure [91] and is in itself a candidate nuclear waste form for the incorporation of Pu and MA [79, 90, 92], however its thermal conductivity is relatively low [86, 93]. As a result, the combination of MgO and pyrochlore provides an IMF candidate that has attracted substantial interest in recent years [75, 79, 82-87].

The conventional method to produce $Nd_2Zr_2O_7$ with the pyrochlore structure is the solid-state mechanical mixing of single metal oxide material, followed by high temperature calcination [83, 85]. However, it is difficult to produce pyrochlore powder with homogeneous composition, thus multiple milling steps are required to overcome this drawback. In order to improve the uniformity of the materials, several wet-chemistry routes have been investigated for the preparation of the pyrochlore phase. All wet chemistry methods involve the mixing of starting materials at the molecular level, thus leading to high compositional homogeneity, high stoichiometric control, and relatively low sintering temperatures. The common methods for the production of $Nd_2Zr_2O_7$ include sol–gel processing [88, 94, 95], co-precipitation [85, 86, 96-100], the Pechini polymeric route [101-104] and the precipitation-combustion method [105, 106].

The only published method to produce MgO–$Nd_2Zr_2O_7$ composite materials, to my knowledge, is physically mixing and sintering pre-prepared ceramics of MgO and $Nd_2Zr_2O_7$ [82, 83, 85, 87, 88]. Besides the traditional grinding and mortar mixing, used in an attempt to improve the homogeneity of the final product, several other approaches have been employed including high-energy shaker blending and ball milling [83, 85, 87]. Nevertheless, the peak size of the particles is still over 2 microns (varying widely up to several tens of microns) with significant non-homogeneity throughout the composite

materials. Large and hard pyrochlore agglomerates form in the milled composite powders and these do not rearrange during sintering to homogenise the microstructure. As a result, there is the potential for local "hot-spots" in the larger pyrochlore particles which would incorporate the Pu and MA within the fuel matrix. Further, previous work [83] has shown the tendency for cracks to form between the heterogeneities and the interpenetrating matrix as a result of differential sintering, and this would be detrimental to affect the conductivity of the composite.

In the present study, a homogeneous NdZr-complex was produced using an aqueous media with zirconium(IV) bis(diethyl citrato)dipropoxide (Tyzor ZEC) as starting material. Intrinsic stabilizer groups (diethyl citrato) in the Tyzor ZEC not only provide water stability, but also decrease the chemical reaction rate, contrary to the traditionally used zirconium alkoxides which are extremely moisture sensitive. The drying and subsequent calcination of the mixture of synthesized NdZr-complex and the Mg aqueous soluble salt (nitrate, carbonate, or carbonate basic) led to the formation of MgO and the $Nd_2Zr_2O_7$ pyrochlore in a one pot synthesis procedure. The presence of glucose as an organic matrix ensured no gel product was formed during the drying and calcination processes. This new molecular level synthetic approach facilitates the production of homogeneous oxide materials at a relatively low temperature and removes the requirement of subsequent milling steps. $Nd_2Zr_2O_7$ with the pyrochlore structure was obtained within the composite material when prepared in both powder and pellet form and then characterized by a range of techniques. Both $Nd_2Zr_2O_7$ pyrochlore and MgO phases appeared homogenously mixed with submicron sized particles even without milling steps. Glucose was used as a fuel during the exothermic reaction between the fuel and an oxidizer (i.e., nitrates), contributing to the formation of homogeneous oxide ceramics. During the combustion, the evolution of gaseous products dissipates the heat

of combustion, thus reducing the possibility of premature local partial sintering among the primary particles, which leads to formation of 'soft' agglomerates. Comparison composites were also prepared using traditional mixed oxide or sol-gel processing, following similar procedures to those reported in literature [83, 85] and the result compared to the novel method describe here.

Thermophysical properties, such as thermal conductivity, remain one of the most important material properties for the design of safe fuel performance. As mentioned above, one method to improve thermal conductivity is to increase the volume fraction of highly conductive particles. Both the effect of particle size and volume fraction of MgO on the thermal conductivity of the MgO-$Nd_2Zr_2O_7$ composites formed via a novel one-pot preparation were investigated in this study and the results compared to those for composites produced by standard synthetic techniques.

4.2 Experimental section

Zirconium(IV) bis (diethyl citrato) dipropoxide or Tyzor® ZEC containing 12 wt% ethanol and 12 wt% 1-propanol (product of DuPont™), neodymium (III) nitrate hexahydrate (99.9%+), magnesium nitrate hexadrate (98+%), tetrabutyl zirconate, and magnesium oxide were purchased from Aldrich and used as received. Nd_2O_3 (Alfa Aesar 99.9%) and ZrO_2 (Alfa Aesar 99.7%) were used directly. The zirconium content in Tyzor ZEC was determined by gravimetric analysis. All chemicals were A.R. grade, with Milli-Q grade water being used in all experimental procedures.

Aqueous solution (AS)

For a typical synthesis, 6 mmol Tyzor ZEC was dissolved in 60 mL water at 45 ℃. A solution of 6 mmol neodymium (III) nitrate was added to the Tyzor ZEC solution before the pH was adjusted by titration to pH=8.0–8.3 by dropwise addition of 1.667 M ammonia to precipitate the NdZr-complex. The mixture was stirred for 2 hours at room temperature and the precipitate was separated from the aqueous phase by centrifuge to obtain the NdZr-complex precipitate. The calculated magnesium nitrate and the glucose (about 40 wt% of the calcined composites) were thoroughly mixed by a magnetic stirrer with NdZr-complex precipitate, which was dried overnight at 100 ℃. The mixture was calcined at 1000 ℃ for 5 hours (1.5 ℃/min ramp rate). The calcined powder was pelletized using a uniaxial press with approximately 2.5 MPa pressure, and sintered under various conditions in air in a furnace.

Mixed oxides (MO)

A conventional mixed metal-oxide process was employed. Stoichiometric quantities of neodymium oxide and zirconium oxide were heated to 850 ℃ for 10 h to completely remove adsorbed H_2O and CO_2, followed by ball milling in PTFE containers using yttria-stabilized zirconia balls and cyclohexane as the milling media. After drying at 110 ℃, the powder was heated to 1400 ℃ in air for 50 h to form $Nd_2Zr_2O_7$ pyrochlore. The produced pyrochlore was then ground with a mortar and pestle and ball milled with magnesium oxide power in PTFE containers using yttria-stabilized zirconia balls in cyclohexane for 16 h and finally dried at ~110 ℃. The mixed powder was then pelletized using a uniaxial press at ~2.5 MPa and sintered at 1400 ℃ for 50 h in air.

Sol-gel processing (SG)

The sample was prepared by a modified alkoxide route. Nd_2O_3 was first converted to its nitrate salt by dissolving in concentrated nitric acid. A stoichiometric amount of tetrabutyl

zirconate was dissolved in isopropanol and mixed with the aqueous solution containing $Nd(NO_3)_3 \cdot 6H_2O$ in a stainless-steel beaker. The mixture was heated to dryness with stirring on a hot plate at ~110 ℃. The dried powder was subsequently calcined in air for 10 h at 700 ℃ and ball milled in PTFE containers using yttria-stabilized zirconia balls in cyclohexane. The calcined powder was then heated to 1400 ℃ in air for 50 h to form $Nd_2Zr_2O_7$ pyrochlore. The produced pyrochlore was ground with a mortar and pestle and ball milled with magnesium oxide powder in PTFE containers using yttria-stabilized zirconia balls in cyclohexane for 16 h and finally dried at ~110 ℃. The mixed powder was then pelletized using a uniaxial press at ~2.5 MPa and sintered at 1400 ℃ for 50 h in air.

The samples were characterized by XRD, SEM and TEM for compositional and structural analysis, and thermal property analysis were carried out by Laser Flash (LFA), Simultaneous thermal analysis (STA) and Dilatometry (DIL). Density of all samples which used in measurements was measured using Archimedes' method. Details were provided in Chapter 3.

4.3 Results and Discussion

4.3.1 Structural and compositions

For the aqueous solution (AS) synthesis route, the MgO and $Nd_2Zr_2O_7$ phases are formed simultaneously during the solution combustion. Figure 4.1 shows the XRD profiles of the powder samples with various MgO and $Nd_2Zr_2O_7$ volume fractions upon sintering at 1200 ℃ or 1400 ℃ for 12 h. The results showed only MgO and $Nd_2Zr_2O_7$ pyrochlore phases were produced for all variations studied irrespective of temperature.

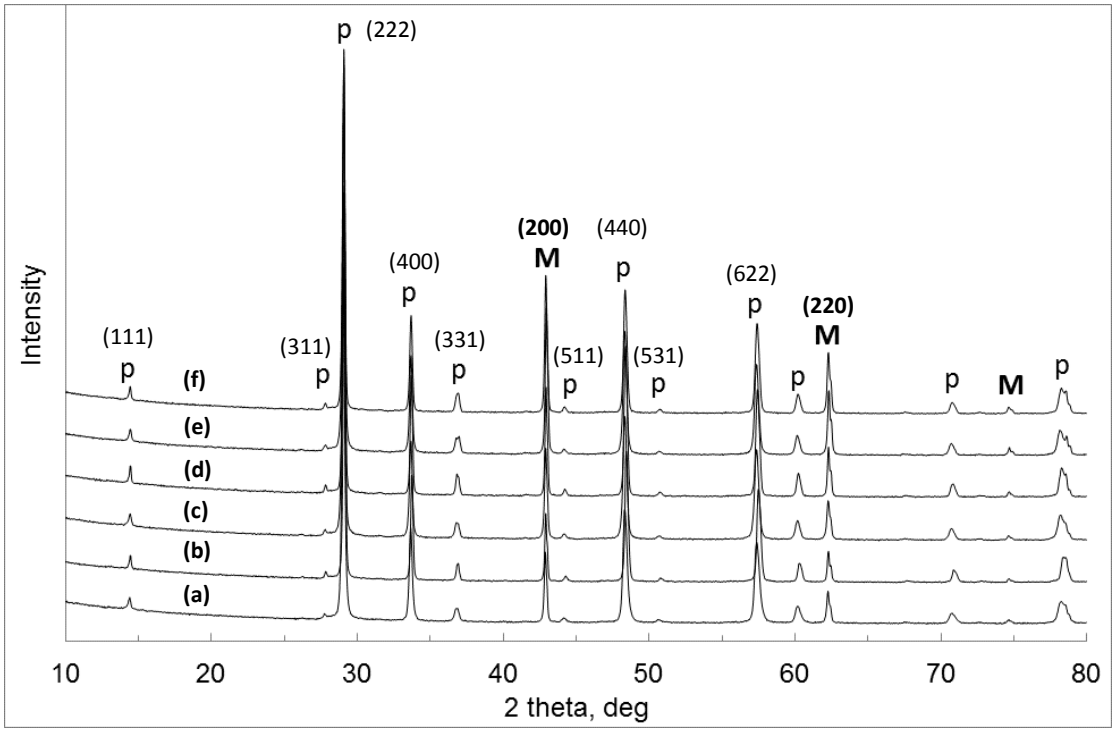

Figure 4.1 XRD patterns following sintered for 12 h for powder samples (a) AS 50:50 at 1200 ℃, (b) AS 50:50 at 1400 ℃, (c) AS 60:40 at 1200 ℃, (d) AS 60:40 at 1400 ℃, (e) AS 70:30 at 1200 ℃, and (f) AS 70:30 at 1400 ℃. M and p refer to MgO and pyrochlore phases, respectively.

Pellets were prepared from powders synthesized by the three routes (aqueous solution (AS), mixed oxides (MO) and sol-gel (SG)) and they were sintered at various temperatures for 50 h and the bulk densities and apparent porosities are shown in Table 4-1. For the AS 50:50 sample, sintering at 1200 ℃ leads to the lowest bulk density with a high apparent porosity of ~37%. When the sintering temperature is increased to 1400 ℃ the bulk density increases to 4.6 g/cm^3 (93% theoretical density) and no further advantage, from a density perspective, was noted by increasing the sintering temperature to 1500 ℃. To allow direct comparison, all subsequent samples were sintered at 1400 ℃ for 50 h. Bulk density was constant for all 50:50 MgO:$Nd_2Zr_2O_7$ samples, irrespective of the

different synthesis methods and satisfactory density results were therefore obtained using the AS route even without additional ball milling steps required for the SG and MO preparations.

Table 4-1 Bulk density and apparent porosity of pellets sintered for 50 h (mean ± standard error of mean, N=3).

Sample*	Sintering temperature	Bulk density (g/cm^3)	Theoretical density (%)	Apparent porosity (%)
AS 70:30	1400 ℃	3.98 ±0.07	90	0.5 ±0.1
AS 60:40	1400 ℃	4.30 ±0.01	92	1.8 ±0.1
AS 50:50	1200 ℃	3.11 ±0.02	63	37.1 ±0.4
AS 50:50	1400 ℃	4.62 ±0.04	93	0.8 ±0.1
AS 50:50	1500 ℃	4.57 ±0.02	92	0.6 ±0.05
SG 50:50	1400 ℃	4.74 ±0.02	96	1.3 ±0.1
MO 50:50	1400 ℃	4.84 ±0.04	98	0.9 ±0.3

*AS, SG, MO refer to samples synthesized by an aqueous solution, sol-gel/nitrate, or mixed-oxide method, respectively. The figure ratio shown after the synthesis method represents the volume ratio between MgO and $Nd_2Zr_2O_7$.

The XRD patterns for the AS 50:50 pellet samples sintered at different temperatures are shown in Figure 4.2. The peak intensity in the patterns only slightly increases with increasing temperature from 1200 ℃ to 1500 ℃, with little changes in the intensity of the super-lattice reflections, suggesting insignificant changes in the pyrochlore ordering. Further, there is no obvious change in peak width with sintering temperature suggesting the $Nd_2Zr_2O_7$ grain sizes are similar in the temperature range studied and in the presence of 50 vol.% MgO.

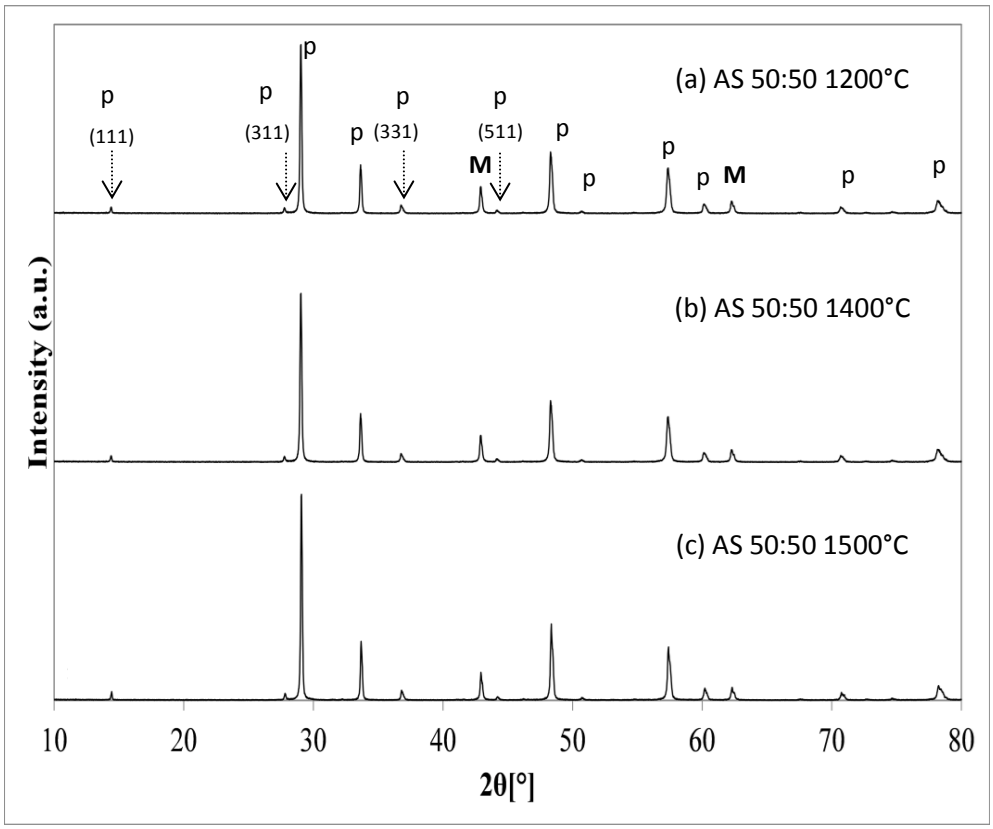

Figure 4.2 XRD patterns of pelletised samples AS 50:50 sintered for 50 h at (a) 1200 ℃, (b) 1400 ℃ and (c) 1500 ℃. M and p refer to MgO and pyrochlore phases, respectively. Pyrochlore super-lattice reflections are indicated with arrows.

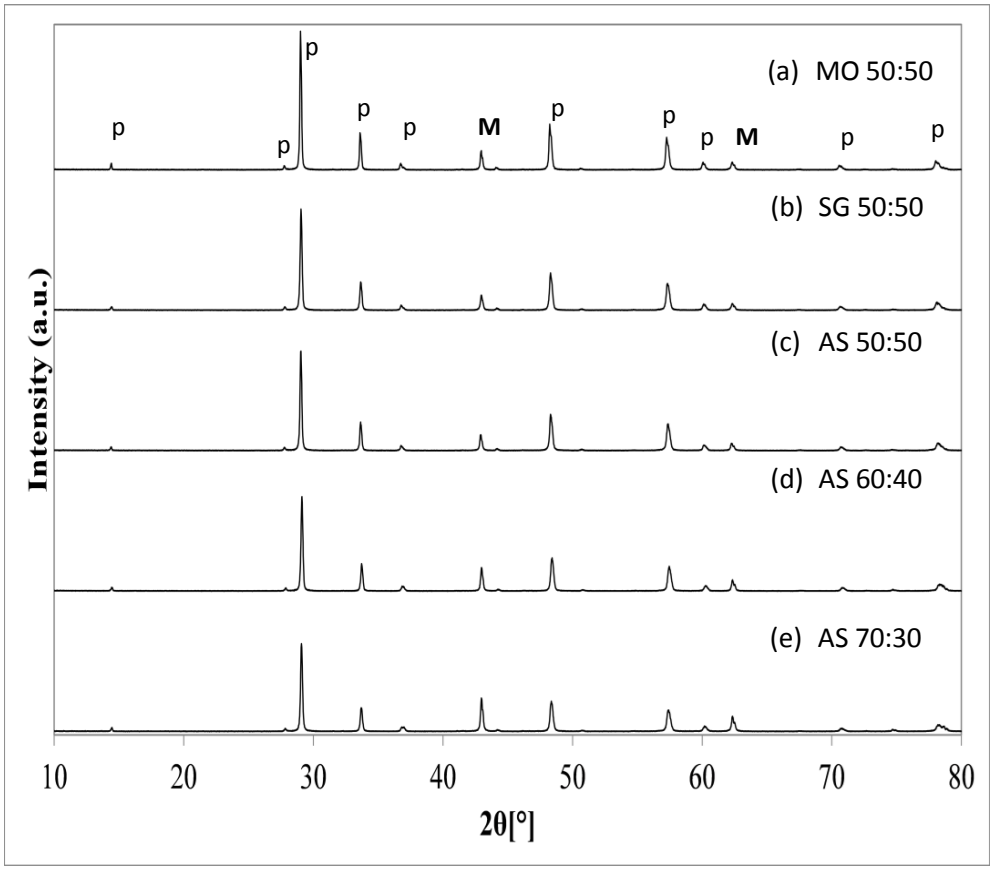

Figure 4.3 XRD patterns of pellet samples sintered for 50 h at 1400 ℃. p and M refer to pyrochlore and MgO phase, respectively.

The XRD patterns for samples synthesized by the three different routes with 50:50 MgO:$Nd_2Zr_2O_7$ (v/v) together with samples prepared by the aqueous solution route with varying MgO and $Nd_2Zr_2O_7$ volume fractions are displayed in Figure 4.3. The slightly higher intensity for MO 50:50 samples could be due to its longer total heat treatment time of 100 h (50 h to form $Nd_2Zr_2O_7$ pyrochlore, and 50 h after mixing with MgO), leading to slightly higher crystallinity. Among the aqueous solution route samples, the peak intensities of the MgO reflections increased as the MgO volume fraction increased from 0.5 to 0.7 with corresponding decrease in intensity of the pyrochlore reflections.

SEM was performed to assess the distribution of the MgO and $Nd_2Zr_2O_7$ phases for pelletized samples. As shown in Figures 4.4(a) and 4.4(b), the grain sizes for both phases synthesized by mixed oxide and sol-gel methods vary from approximately 1–5 μm. Further, large pyrochlore agglomerates of the order of hundreds of microns were observed for the MO and SG samples, as described previously [83] for these composites prepared by standard ball milling procedures. By contrast, no such agglomerates were observed for samples produced by the aqueous solution route and grains of the order of 200–500 nm were formed, regardless of the volume fractions of the two phases (see Figure 4.4(c) – (e)). Importantly, samples with MgO 50:50 vol.% synthesized by the aqueous solution route appear significantly more homogeneous than those samples prepared by mixed oxide and sol-gel routes.

Uniform distribution of MgO and $Nd_2Zr_2O_7$ is an essential feature for a material used as an IMF [85]. For samples AS 50:50 and AS 60:40, the microstructures were highly consistent, with equally distributed MgO or $Nd_2Zr_2O_7$ phases (Figure 4.4). Some MgO agglomerates (~5 μm), however were observed at the higher MgO volume fraction for sample AS 70:30 (see Figure 4.4(e) and 4.4(f)). This is important when considering a once though then out approach where the large agglomerates of MgO have been shown to be detrimental to the corrosion resistance of the composite [85].

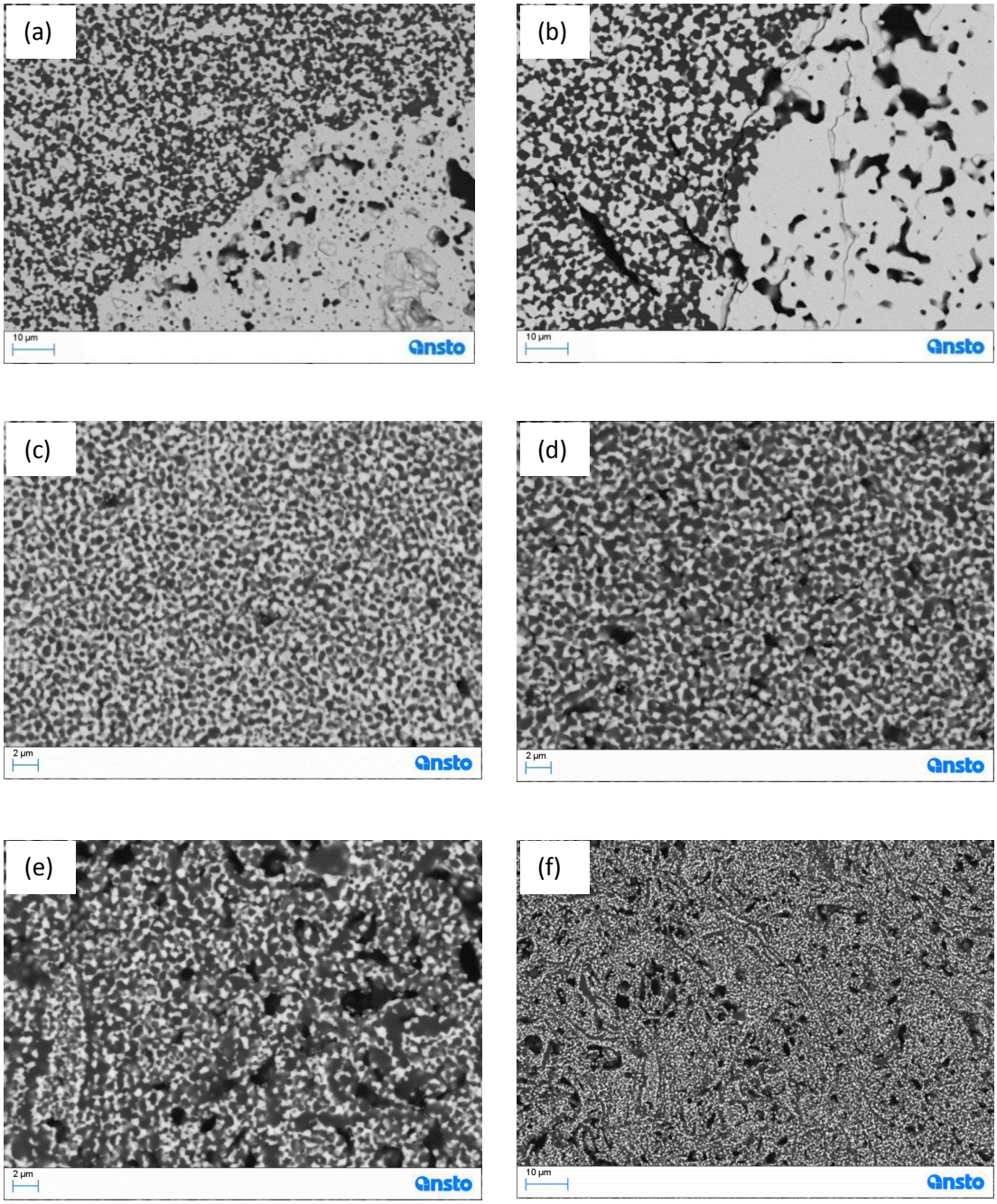

Figure 4.4 Back-scattered SEM images of pellet samples (a) MO 50:50, (b) SG 50:50, (c) AS 50:50, (d) AS 60:40, (e) AS 70:30 and (f) AS 70:30 with low magnification. Pellet samples were sintered for 50 h at 1400 ℃. Dark grains are the MgO phase and the light grains are $Nd_2Zr_2O_7$, black areas are pores.

TEM was used to assess the interface between grains for AS 50:50 and the results are shown in Figure 4.5. Figure 4.5(a) is a bright field TEM image showing grains of both

phases are in the range of ~200–500 nm in size, in agreement with SEM analyses. Pores are visible as white regions at triple points. MgO grains are generally brighter than $Nd_2Zr_2O_7$ grains, although electron diffraction can cause some MgO grains to be dark, e.g. the large mottled grain at bottom center of Figure 4.5(a). Electron energy loss spectroscopy (EELS) elemental maps of Mg, Zr and Nd are shown in Figures 4.5(b), 4.5(c) and 4.5(d), respectively. In these elemental maps, light regions indicate the element is present. The light phase in Figure 4.5(b) corresponds to MgO. The distribution of Zr and Nd in Figures 4.5(c) and 4.5(d), respectively, are identical (except in the upper left corner where the sample thickness is too great for reliable EELS elemental mapping) and corresponds to the $Nd_2Zr_2O_7$ phase. These results confirm the compatibility of the phases using the aqueous synthesis preparation with distinct phases of MgO and $Nd_2Zr_2O_7$ with no secondary phases at the grain boundaries. Further, no cracking was noted between the grains as a result of differential sintering. Such cracks have been observed previously [83] and are detrimental to affect the conductivity.

The grains are relatively small and may be expected to reduce thermal conductivity when compared to products from mixed oxide or sol-gel preparations (with 1-5 μm particles), due to an increase in grain boundaries per sample volume relative to standard synthesis methods. However, most grains appeared interconnected; the observed connectivity the MgO phase prevents significant reduction of the thermal conductivity of the composite.

The microstructure of the composite is an important factor when considering materials for this use, as the lack of continuity of MgO phase through the material may cause dispersion of the thermal conductivity of the composite [83, 85]. On the other hand, inconsistent microstructures with large agglomerates of $Nd_2Zr_2O_7$ will result in low and inconsistent thermal conductivity. Although a fine microstructure (< 1 μm) is produced

by the aqueous synthesis approach which resulted in an increase of grain boundaries, a benefit as seen from SEM and TEM is that a homogeneous composite with no cracks at the grain boundaries and a thermally conductive path appears to run though the composite even for the AS 50:50 sample. Also, the small grain sized particles achieved will assist in radiation tolerance of the composite from a cracking perspective as the effects from anisotropic swelling on amorphization (detailed well in literature) are limited. The achievement of the small grain size and even distribution of the two phase are extremely difficult or hardly possible to achieve by physical mixing of the two powders as in many reported references. The application of this novel synthesis in the real nuclear fuel production would provide better structural and composition properties.

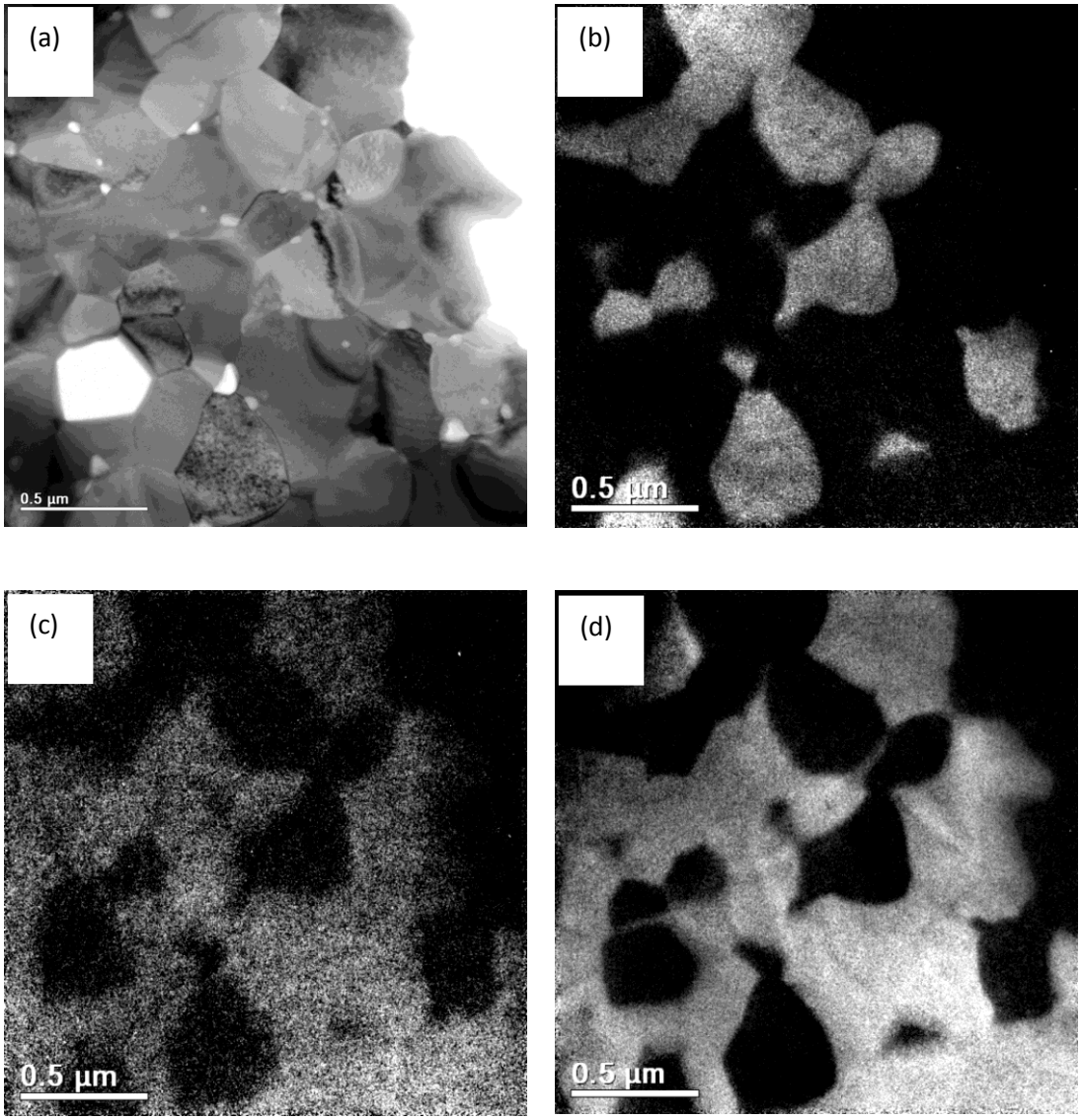

Figure 4.5 TEM images of pellet sample AS 50:50 sintered for 50 h at 1400 ℃. (a) TEM bright field electron image and electron energy loss elemental maps of (b) Mg, (c) Zr, and (d) Nd; light phases in (b) – (d) indicate detection of the element.

4.3.2 Thermal properties

The thermal diffusivity data for the 50:50 MgO:$Nd_2Zr_2O_7$ samples prepared by the various methods (Figure 4.6(a)) show the same general trend and are within 5% error. This indicates the effect of particle size variations between sol-gel, solid state and aqueous solution methods on thermal diffusivity was small. Figure 4.6(b) displays the thermal

diffusivity for the varying ratios of $MgO:Nd_2Zr_2O_7$ produced by the novel aqueous synthesis approach. For these three samples, thermal diffusivity was the same (within error) at temperatures above 800 ℃. At temperatures below 800 ℃ the thermal diffusivity was enhanced with increasing MgO content and the sample with 70% MgO provided the highest thermal diffusivity in the 100 – 800 ℃ range. Others have reported a particle size of 1-2 μm using a mixed oxide approach and have similarly shown higher thermal conductivity with higher MgO content (50% to 70%) [87] up to 1000 ℃ although their experiments do not investigate the high temperature range shown here.

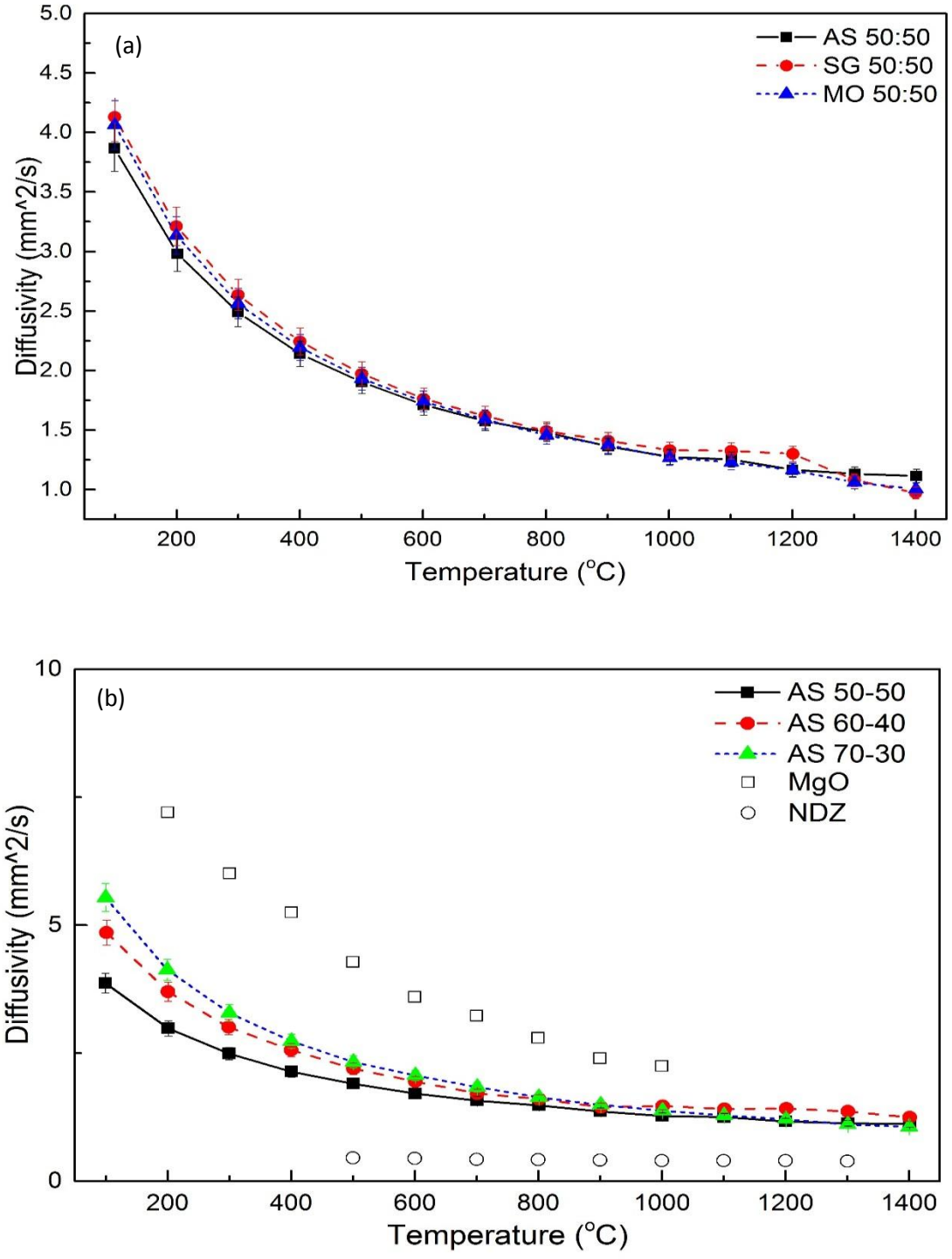

Figure 4.6 LFA data from samples (a) using different synthetic methods with MgO : $Nd_2Zr_2O_7$ v/v ratios at 50:50, and (b) MgO : Nd2Zr2O7 v/v ratios at 50:50; 60:40; 70:30, the literature values for MgO [107] and Nd2Zr2O7 [86] are included for comparison.

Figure 4.7 (a) shows the specific heat capacity data for each composition synthesized using the novel method. Since there was no phase transformation or other reaction in the measured temperature range, the Neumann-Kopp rule [108] was used to predict the heat capacity and these data are plotted together with the measured data in the inset of Figure 4.7(a). The two sets of values were within 5% error.

The specific heat capacity data for the MgO:$Nd_2Zr_2O_7$ v/v ratio 50:50 samples produced by different synthetic approaches (Figure 4.7(b)) are similar and within the 5% instrumental error, which again suggest that the different particle size produced by the various synthetic approaches has little effect on heat capacity in the measured temperature range. A previous study [109] investigating CuO nanoparticles suggests a smaller particle size reduces heat capacity but mainly in the very low temperature range of 0-14 K.

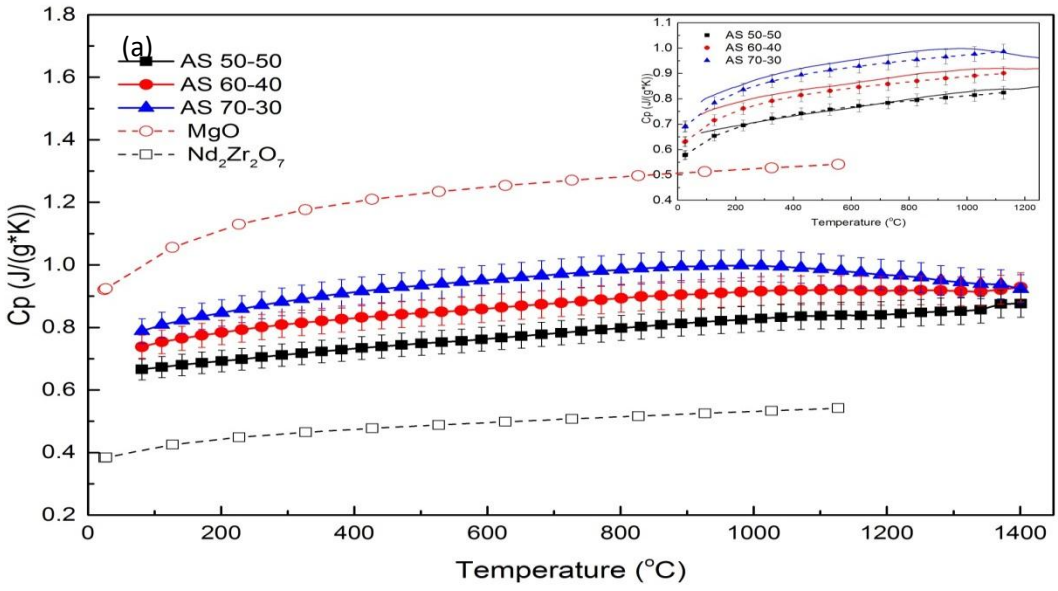

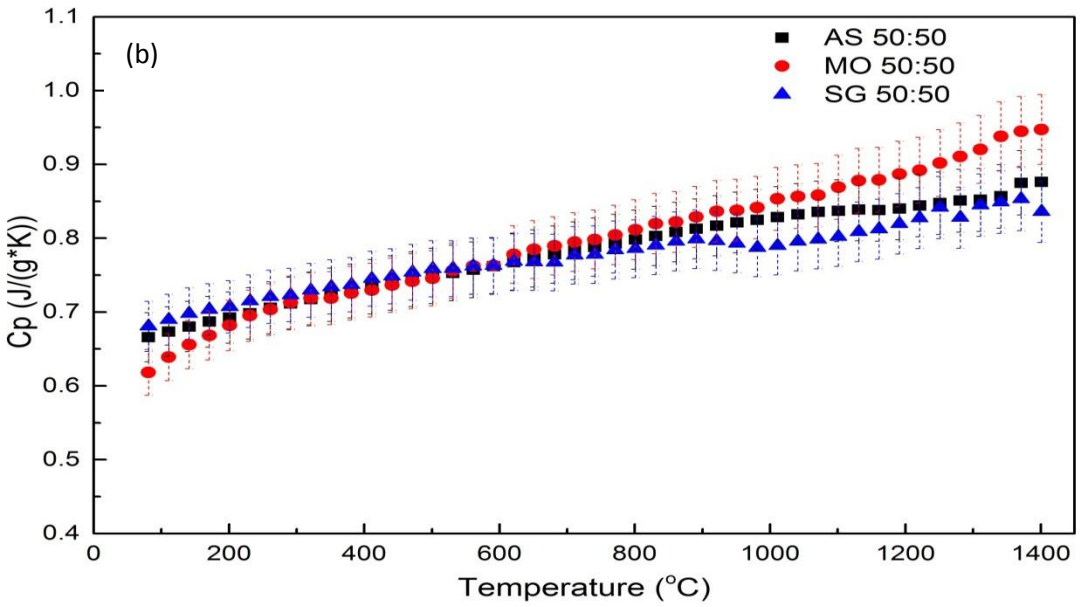

Figure 4.7 Heat capacity measurements for samples with (a) MgO:$Nd_2Zr_2O_7$ v/v ratio 50:50; 60:40; 70:30. The literature values for MgO [84] and Nd2Zr2O7 [60] are included for comparison, and the inset figure in (a) shows the predicted heat capacity (dotted lines), (b) using different synthesis approaches for samples with MgO : $Nd_2Zr_2O_7$ v/v ratios at 50:50.

The measured thermal expansion of all samples is shown in Figure 4.8 and these appear to be linear across the temperature range of interest. The average thermal expansion coefficients for AS 50-50; 60-40; 70-30 are 1.3, 1.4, and 1.4×10^{-5}, respectively, and 1.3 and 1.3×10^{-5} for the mixed oxide and sol-gel synthesis methods. The values are ~10% higher when compared to the data of Nelson et al [87] who investigated thermal expansion up to 1000 ℃. There is no difference in the thermal expansion for samples synthesized by the various approaches, thus the particle size effect on thermal expansion was negligible in the temperature range investigated here. The change in MgO content also had little effect on thermal expansion coefficients.

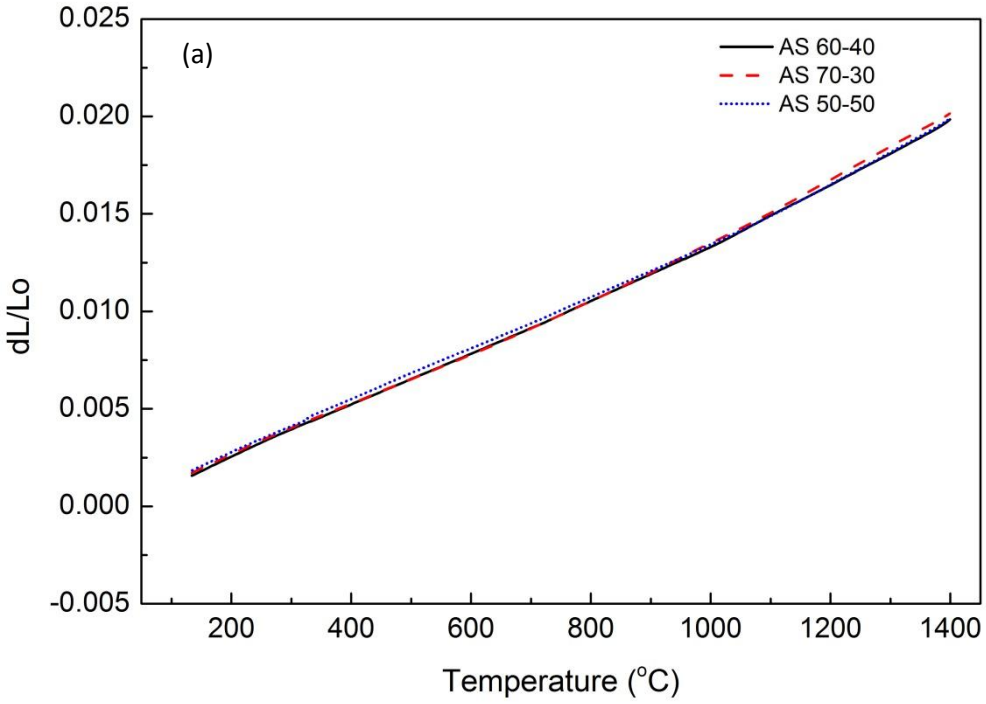
(a)
AS 60-40
AS 70-30
AS 50-50
dL/Lo
0.025
0.020
0.015
0.010
0.005
0.000
-0.005
200
400
600
800
1000
1200
1400
Temperature (°C)

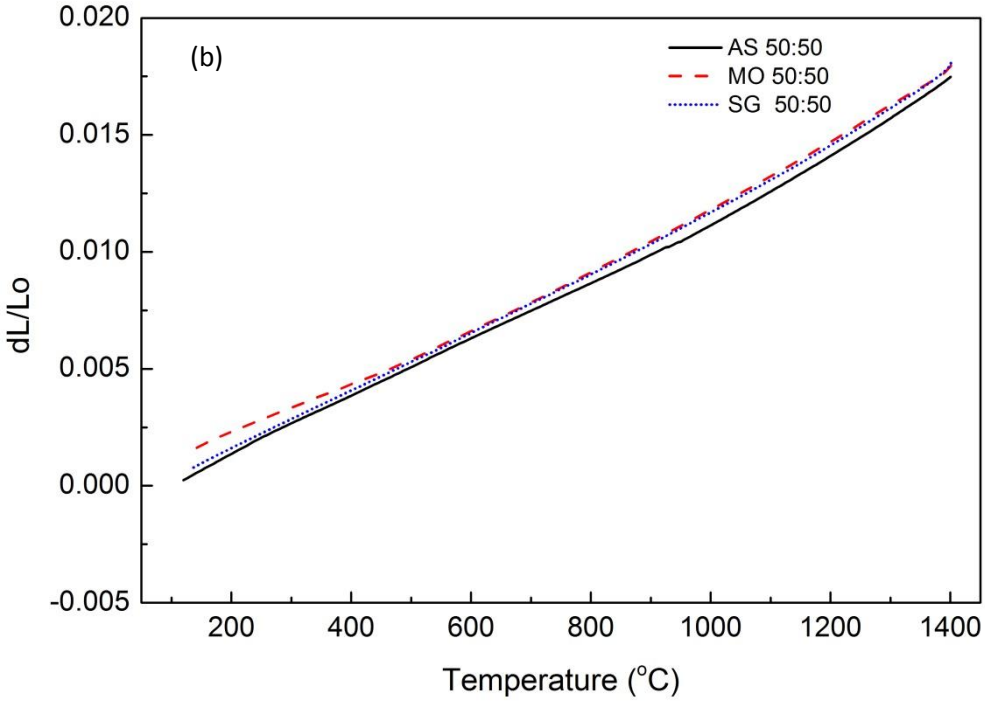

Figure 4.8 Linear thermal expansion data for samples with (a) MgO:$Nd_2Zr_2O_7$ v/v ratio of 70:30; 60:40; 50:50 produced by the novel aqueous approach, (b) MgO:$Nd_2Zr_2O_7$ v/v ratio 50:50 produced via different synthesis routes.

The thermal conductivity data for all samples were calculated as the product of the thermal diffusivity, specific heat capacity, and density and the results are shown in Figure 4.9. For the calculation, a temperature dependent density of all samples was calculated using the average bulk density at room temperature and the linear thermal expansion coefficient observed in the measurements. Generally speaking the thermal conductivity gradually decreases with increasing temperature, similar to most ionic-bonding polycrystalline materials and is related to the lattice thermal conduction (the phonon mechanism) [110]. The thermal conductivity at 100 ℃ was found to increase with increasing MgO content from ~12 W m^{-1} K^{-1} for AS 50:50 to ~18 W m^{-1} K^{-1} for AS 70:30. This is in agreement with percolation theory which states that after the percolation threshold is reached the conductivity of the composite increases significantly with

volumetric concentration of the particle with higher transport property [111]. This can be seen when comparing the thermal conductivity of AS 50:50 with AS70:30 where the higher volume of MgO results in an increase in the thermal conductivity. In the 1000-1400 ℃ range however, where lattice vibrations are significant and the phonons are scattered, the thermal conductivity was independent of MgO content and consistent for all samples (~5 $Wm^{-1}K^{-1}$). This value is consistent with those reported previously for MgO:$Nd_2Zr_2O_7$ compositions [85]. The thermal conductivity determined here is also significantly higher than that for UO_2 and ZrO_2 (approximately 2 and 3.5 $Wm^{-1}K^{-1}$, respectively at 1000 ℃ [112]).

No significant difference in thermal conductivity was noted for the 50:50 MgO:$Nd_2Zr_2O_7$ samples produced by the novel and traditional methods above 400 ℃, however below this temperature the AS sample shows a slightly lower thermal conductivity with ~7% and 11% average reductions when compared to the MO and SG samples, respectively. This is likely a result of the submicron particle size produced during AS and the associated increased grain boundaries in the samples. As A phonon propagates across the interface between MgO and $Nd_2Zr_2O_7$, the phonon wave is refracted at the interface and the smaller particle size results in a larger number of interfaces, thus more refraction and less propagation occurs. Again, this is only notable at low temperatures, and above 400 ℃ these samples showed similar thermal conductivity (Figure 4.9(b)). As such, for in-reactor pellet operating temperatures of the order of 1000 ℃, all samples appear to have similar thermal conductivity (~5 $Wm^{-1}K^{-1}$) and thus independent of the synthesis procedure undertaken and MgO content.

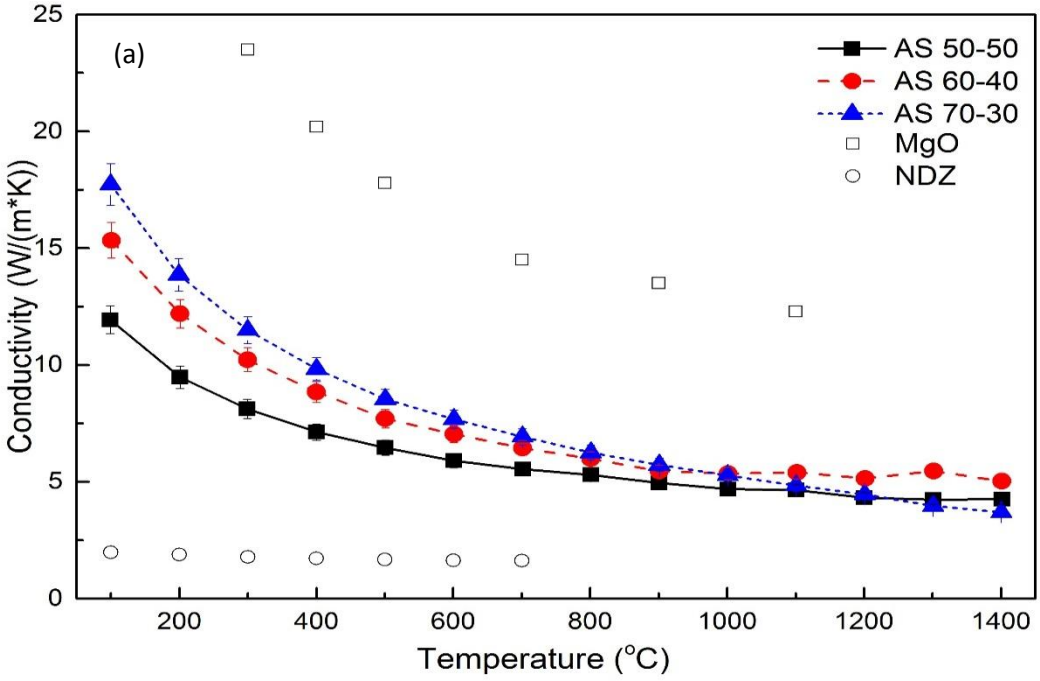
(a)
AS 50-50
AS 60-40
AS 70-30
MgO
NDZ
Conductivity (W/(m*K))
Temperature (°C)
0
5
10
15
20
25
200
400
600
800
1000
1200
1400

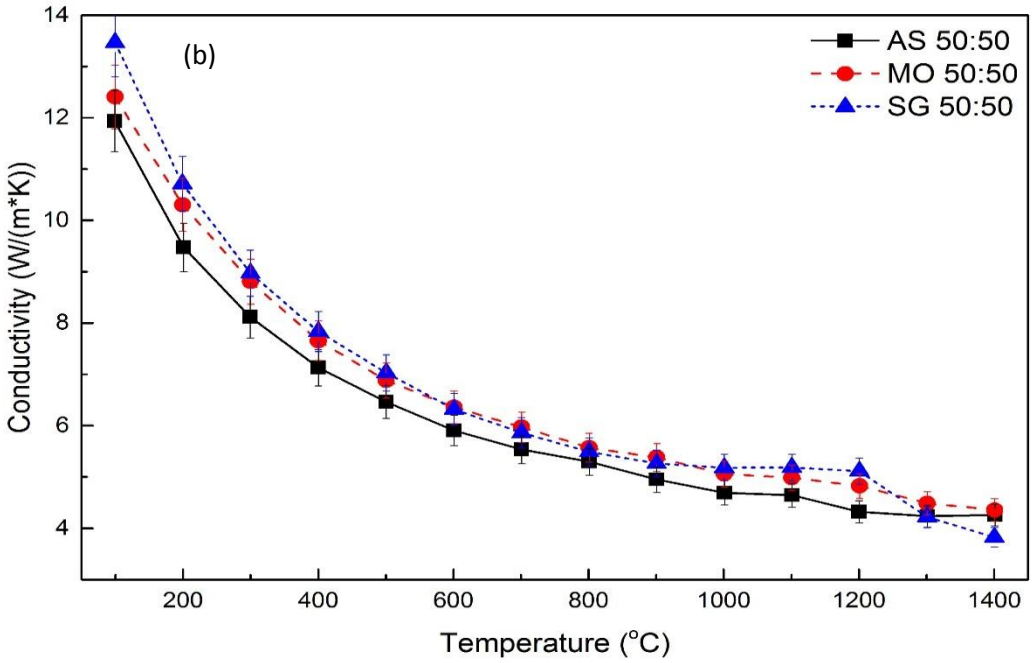

Figure 4.9 Thermal conductivity measurements for sample with (a) MgO:$Nd_2Zr_2O_7$ v/v ratio of 70-30; 60-40; 50-50 produced by novel aqueous approach, the literature values for MgO [107] and $Nd_2Zr_2O_7$ [93] are included for comparison, (b) MgO:$Nd_2Zr_2O_7$ v/v ratio of 50-50 produced using different synthesis routes.

4.4 Summary

MgO and pyrochlore $Nd_2Zr_2O_7$ composites were produced via a chemical route using an aqueous solution in a one-pot synthesis procedure. The chemical reaction takes place at molecular level which ensures high homogeneity of the synthesized powder. The results show that the $Nd_2Zr_2O_7$ pyrochlore superstructure is formed after sintering for 12 h over 1200 ℃ in the presence of MgO. The pellets with a content of MgO 50–70 vol.% show grains in the submicron size range (200–500 nm) for both phases and relatively high density (> 90% of theoretical density) is achieved after sintering at 1400 ℃ for 50 h. MgO and $Nd_2Zr_2O_7$ are homogeneously distributed with no agglomerates observed for samples containing 50–60 vol.% MgO synthesized by aqueous solution route. Certainly samples synthesized by aqueous solution processing have better homogeneity than those

synthesized by mixed oxide and sol-gel routes which produced pyrochlore agglomerates. Further, no cracking between grains of the two phases was observed for the aqueous solution route. Importantly, the results show that although the aqueous solution method results in a reduced particle size it does not detrimentally affect the thermal conductivity at application relevant temperatures above 300 ℃, due to enhanced homogeneity and connectivity. This novel aqueous synthetic method provides a simple pathway for the candidate IMF MgO–lanthanide zirconate pyrochlore production without need for organic solvents and mechanical milling, making it very attractive for a potential scale-up production.

5. Gold Ion Beam Irradiation Effects on ABO_4 Compounds with Various Structure Type

5.1 Introduction

The immobilization and long-term disposal of nuclear wastes have become a significant challenge. There are various types of high level nuclear wastes generated from nuclear operations, mainly spent fuel, liquid from reprocessing spent fuels and waste arising from the production of nuclear weapons, also weapon grade plutonium from dismantled nuclear war-heads. One way to dispose of these high level nuclear wastes is to process them into dense refractory solids (waste forms) which can survive a long period of time underground (e.g. U & Th containing minerals monazite and zircon). Over the past several decades, synthetic rock (Synroc) waste forms have been studied as nuclear waste host phase materials, because these types of natural minerals often contain uranium and thorium. For example, pyrochlore [52], and zirconolite [53], are both ideal host phases for Pu, U and actinide immobilization. In recent years zircon ($ZrSiO_4$) [54] and monazite ($REEPO_4$, where REE are rare earth elements) [55] (ABO_4), and zirconium-based materials with fluorite or defect fluorite structures have also been extensively studied. These materials have excellent resistance to α-radiation induced amorphization and excellent chemical durability [22, 56-58]; however, little work has been done on other compounds in the ABO_4 family which regard to radiation tolerance.

The ABO_4 family has a crystal structure consisting of A cations surrounded by isolated BO_4 (B = P, Si, V, and Nb) tetrahedra, and numerous structures of ABO_4 are found. Further, these are polymorphic at normal atmosphere with different structures at higher pressure. There are mainly four structure types, monazite (monoclinic, P21/n), zircon (tetragonal, I41/amd), scheelite (tetragonal, I41/a), and fergusonite (monoclinic, I2/c).

The strong tetrahedral bonding of B-O provide eight-fold (tetragonal) or nine-fold (monoclinic) coordination around the A atoms [59]. The structures show various combinations of valence for both A- and B-site atoms such as I-VII, II-VI, and III-V groups. There are many studies on the phase transformations of these structures [60-63]; the pathways from one structure to another have been summarized by Aldred [59] with, pressure, temperature, preparation techniques and changes in A and B site atom size. As a nuclear waste host material, the potential phase changes (loss in crystallinity and amorphization) of these compounds can affect the durability over the long term.

There are many studies on different A-site atoms of zircon, and monazites using ion beam irradiation or the doping of actinides [22, 57, 66-69]. The most studied ABO_4 compounds were zircon (tetragonal) and monazites (monoclinic) and these respond differently to ion irradiation. Meldrum et al. [22] have studied actinide induced radiation damage in zircon (natural and synthetic) and monazite. They found that monazite cannot be amorphized by 800 KeV Kr^+ ions at temperatures greater than 175 ℃; whereas zircon can be simply amorphized at temperatures up to 740 ℃ [22]. Meldrum et al. [69] have also described the effect of structure variations of zircon and monazite on ion beam irradiation (Kr^{2+}, 800 KeV) using Hobb [21] model, and according to the model the susceptibility to amorphization is governed by the connectivity of the cation polyhedra. However very little work has been undertaken to investigate other B cations in this system. Lu et al. [70] investigated the radiation tolerance of varying B-site compositions of vanadate-phosphate fluorapatites. Here other ABO_4 compounds have been studied and a range of samples with three different B site cations and with different structures was selected. For $CaWO_4$, $LaNbO_4$, $YNbO_4$, $LaVO_4$, and YVO_4 the corresponding crystal structures are scheelite, fergusonite, fergusonite, monazite and zircon respectively. Calcium tungstate has a scheelite (tetragonal) structure, and the vanadates selected have two different structures

at room temperature, such as, $LaVO_4$ has a monazite (monoclinic) structure and YVO_4 has a zircon (tetragonal) structure; while both niobates have fergusonite (monoclinic) structure. The compositions that were selected cover all possible structures in the ABO_4 family, and span a range of chemistries.

The α-decay process in minerals includes simultaneous release of one energetic α-particle normally 4-5 MeV, and one heavy but low energy (70-100 KeV) recoil atom [113]. The stopping ion range, in general, for the massive recoil nucleus is of the order of 20-25 nm and would displace approximately 1000 atoms primarily by nuclear stopping processes; However for an α-particle the ion range is much longer, about 10 - 15 μm, and the energy is predominantly deposited through electronic interactions, while at the end of its track it displaces on the order of 100 atoms by mainly nuclear stopping processes [113]. In the study, ion beam irradiation using 5 MeV Au-ions has been selected to provide a measurable damage depth for further analysis, and the investigate the consequences of the recoil nucleus from α-decay on the structure and properties of different ABO_4 structure type compounds were studied.

5.2 Experimental section

Samples of $CaWO_4$, $LaNbO_4$, $LaVO_4$, $YNbO_4$, and YVO_4 were synthesised via a mixed oxides method using laboratory grade powders of 99.99% of La_2O_3, 99.99% Nb_2O_3, 99.99% Y_2O_3, 99% WO_3, 99% V_2O_5 and 99% $CaCO_3$. Firstly, all the powders were calcined, where $CaCO_3$ was heated at temperature of 120 ℃ for 12 hours and the rest were heat treated at 600 ℃ for 10 hours in a platinum crucible. Stoichiometric amounts of the mixed powders were weighed in Teflon containers and ball milled with zirconia balls in cyclohexane for 16 hours. The cyclohexane was then evaporated at 100 ℃ in stainless

steel pans and the powder pressed into pellets followed by cold isostatic pressing (CIP) at 400 MPa for the tungstate and vanadates, and at 300 MPa for the niobates. Finally, the resulting pellets were sintered at 1400 ℃ for the niobates and tungstate and at 1000 ℃ for the vanadates for 16 hours.

The samples were characterized by XRD, SEM and Raman for compositional and structural analysis, Density of all samples which used in measurements was measured using Archimedes' method.

5.3 Ion beam irradiation

Ion irradiation experiments were carried out in order to simulate the effect of the α-recoil nucleus. Au ions with 5 MeV were selected to simulate the α-recoil events which have energy between 70 and 100 KeV. The kinetic energy from these particles was deposited in the host material by ballistic (E_{nucl}) and electronic (E_{elec}) excitation processes [114].

Au ions have a similar mass to the α-recoil atom; however the low energy (~70-100 KeV [113]) in the actual event will only penetrate 20-25 nm which restricts the achieved characterization of the damage layer. Therefore, increasing the energy of the implanted Au ion can provide a thicker layer of damaged material which can be analysed by XRD, SEM, and Raman spectroscopy. However, the ballistic electronic energy ratio was altered by increasing the implanting ion energy. Table 5-1 summarizes the depth profile and energy fraction, and shows that for 5 MeV Au ions (used in study) the energy transfer by electronic excitation will be higher than that for an alpha recoil atom. Although the damage mechanism maybe affected by altering the implantation energy, it is expected amorphization fluences will be similar from Au ions and recoil atoms. The ion fluences were chosen to match a similar displacement per atom (dpa) value which would be

produced over several hundreds of years in a waste form material containing 10 wt% minor actinides oxide [68, 115], i.e. a corresponding nuclear damage of the order of 1 dpa. From SRIM [116] calculation, both electronic and nuclear stopping power and dpa at different fluences can be calculated and these are also listed in Table 5-1 [116].

Table 5-1 Depth profile and energy fraction based on SRIM 2013 simulation for 5 MeV Au+ ions ions [116][1]

Sample	Peak damage depth (μm)	Ion ranges (μm)	DPA (ions/cm^2)		f_{nucl} (%)	f_{elec} (%)	dE/dx Nuclear (eV/Ang)	dE/dx Electron (eV/Ang)	ENSP
			10^{14}	10^{15}					
$CaWO_4$	1.56	1.9	0.29	2.89	36	64	312.94	294.31	0.94
$LaNbO_4$	1.74	1.74	0.25	2.5	27	73	310.57	344.26	1.11
$LaVO_4$	0.63	1.94	0.33	3.25	26	74	276.93	315.11	1.14
$YNbO_4$	0.7	1.85	0.28	2.85	34	66	323.00	342.64	1.06
YVO_4	0.56	2.11	0.34	3.36	33	67	264.32	287.68	1.09
$CaWO_4$ [2]	0.014	0.0245	0.45	4.51	68	32	395.08	294.31	0.09

[1] The calculations for ABO_4 samples were using 50 eV displacement energies for every element, and the density was calculated from the XRD pattern by refining lattice parameter.

[2] The comparison of Th ion implanted in $CaWO_4$ with 100 KeV.

5.4 Results

5.4.1 Un-irradiated materials

The XRD results for all pristine ABO_4 compounds in this study are shown in Figure 5.1 from 15° to 60° with normalized intensity. The patterns show $CaWO_4$ and YVO_4 have tetragonal structure; $YNbO_4$, $LaVO_4$ and $LaNbO_4$ have monoclinic structure (although trace amounts of a second phase of Nb_2O_5 monoclinic structure and $(LaNb_3O_9)_{0.6667}$ with tetragonal structure were observed in the pattern for $LaNbO_4$). These results were confirmed by EDS-SEM analysis.

The different structures of the two vanadates were expected; in general vanadates will have zircon type structure with r_A/r_B (k) between ~1.5-2.0 and $(r_A + r_B)/2r_O$ (t) between ~0.45-0.55 [62], however with increasing ionic radius, the lanthanide vanadate will have a strong tendency to form a monazite structure, with the higher oxygen coordination number of 9 as compared with 8 of the zircon type structure [58]. Therefore, $LaVO_4$ has a thermodynamically stable monazite-type monoclinic structure while YVO_4 has zircon-type tetragonal structure.

Scanning electron microscopy with energy dispersive X-ray spectroscopy (SEM/EDS) was used to examine the phase purities of the samples. Figure 5.2 shows a back scattered image for each composition with low magnification (200x). Samples with composition $CaWO_4$, YVO_4, and $LaVO_4$ are phase pure with a perfect stoichiometric ratio 1:1 (A:B). SEM analysis of $YNbO_4$ and $LaNbO_4$, confirmed the presence of trace amounts of a second phase as observed in X-ray analysis. SEM confirmed the second phase was $(LaNb_3O_9)_{0.6667}$ and Nb_2O_5 and denote a slight non-stoichiometry in weighing the powders. In addition, the $YNbO_4$ sample displayed trace amounts of a second phase containing the elements La, W, Ti, and Yb. The presence of this phase was likely due to cross

contamination during sample preparation. However, the impurities were rarely observed and only a few small particles sat on the grain boundary.

The density of each sample was measured by Archimedes' method (Table 5-2). The porosity was determined by visualization of SEM pictures and was considered to be the range of 2% and 10% except for YVO_4 which was about 20%. $LaNbO_4$ had larger grains compared to $YNbO_4$, the vanadates and calcium tungstate. The average particle size was determined using the intercept technique where multiple random straight lines were drawn though the micrograph. The number of grain boundaries intersecting the line was counted and the average grain size was found by dividing the number of intersections by the actual line length.

Table 5-2 Porosity and density of each sample.

Sample	Measured density (g/cm^3)	Calculated density* (g/cm^3)	%Theoretical	%Porosity	Particle size (μm)
$CaWO_4$	5.53	6.02	92	2	30
$LaVO_4$	4.58	4.98	92	5	11
YVO_4	3.11	4.19	74	25	2.5
$LaNbO_4$	5.42	5.83	93	3	76
$YNbO_4$	5.10	5.10	91	8	8

*determined from unit cell parameters using X-ray diffraction.

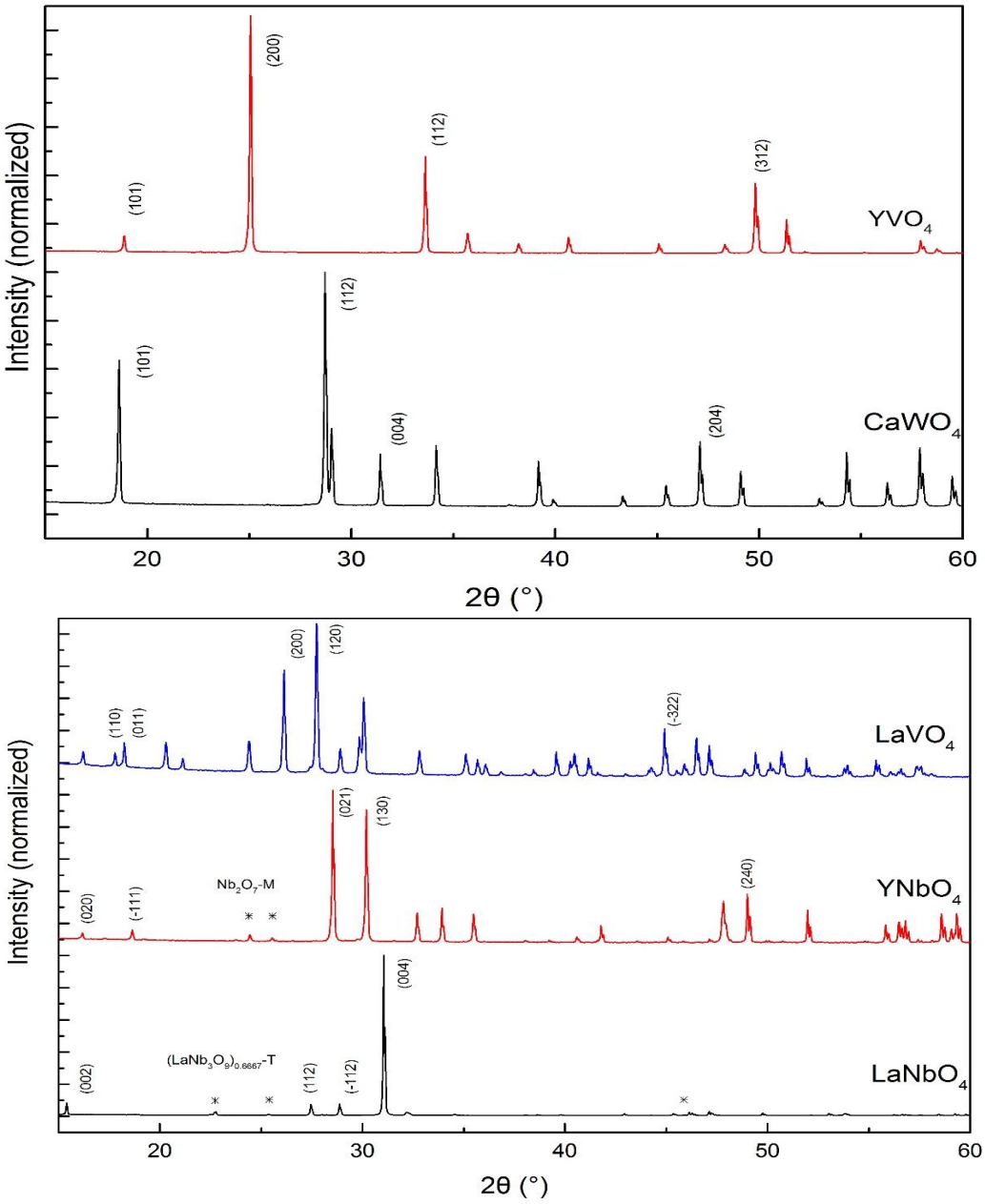

Figure 5.1 XRD patterns for the ABO_4 compounds. YVO_4 and $CaWO_4$ have tetragonal structure while $LaVO_4$, $YNbO_4$ and $LaNbO_4$ have monoclinic structure.* indicate reflections from an impurity in the samples.

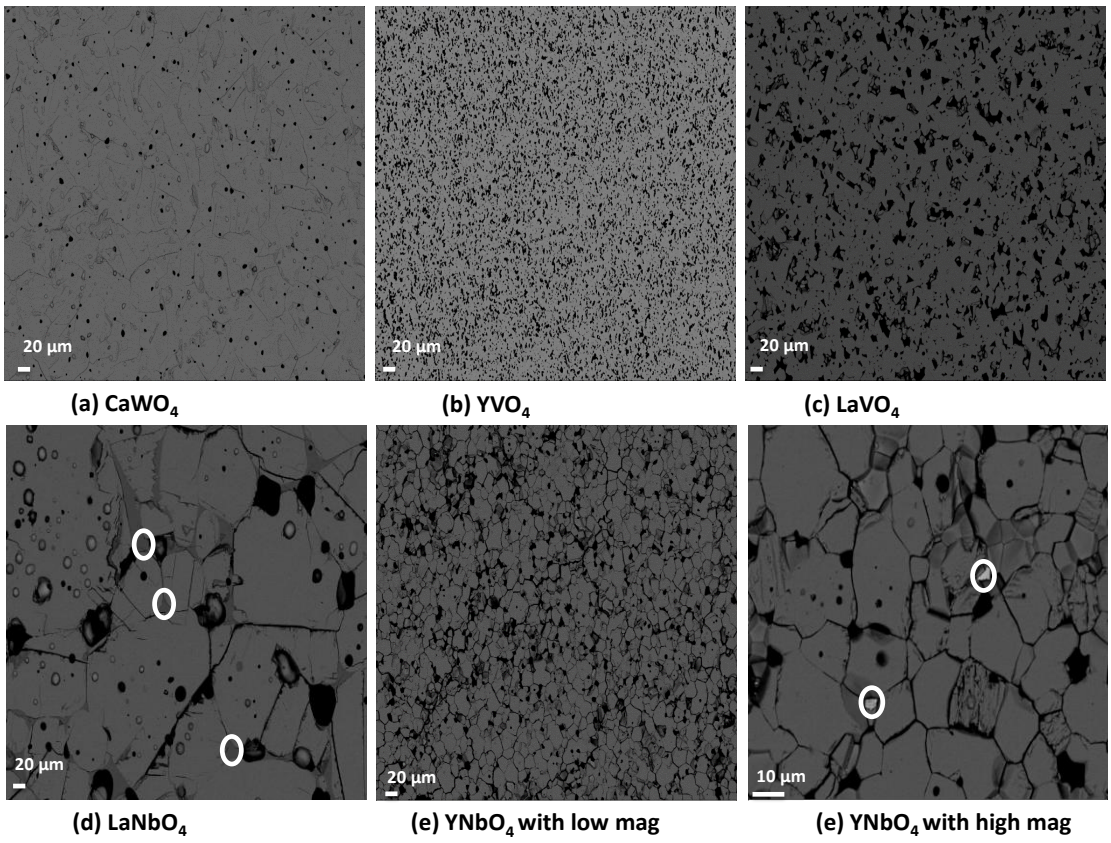

Figure 5.2 Backscattered SEM images for (a) $CaWO_4$ (b) YVO_4 (c) $LaVO_4$ (d) $LaNbO_4$ (e) $YNbO_4$ low mag and (f) $YNbO_4$ high mag. Where (a), (b) and (c) are single phases; (d) and (e) the main grey phase is $LaNbO_4$ and $YNbO_4$, the white phase in (e) and dark grey phase in (d) are the impurities (circled).

5.4.2 Ion implant range

In order to determine the thickness of the damaged layer, SEM was undertaken on cross-sectioned surfaces of the samples. A particular SEM mode was used where the input power was 20 kV and the sample stage was very close to the detector (working distance about 3 µm). This technique has been used to detect defect content and atomic structure of thin films. As shown in the cross-sectioned SEM images (Figure 5.3), the contrast difference infers changes in the crystallinity. In this case the damaged layer is less crystalline while the pristine material remains crystalline further away from the sample

surface. For comparison, the ion range was calculated using SRIM-2013, with displacement energy for each element set of 50 eV and assuming a fully dense sample (the results were listed in Table 5-1). Notice, the depth observed from SEM for $LaVO_4$, $YNbO_4$ and YVO_4 was a slightly higher value (~50%), while $CaWO_4$ and $LaNbO_4$ show slightly lower damage depth (~25%) than that calculated using SRIM. Due to the small percentage of porosity in the sintered samples, Au ions which easily pass through these voids will travel further into the materials. Also, the unknown displacement energy for each element may explain the discrepancy between experimental and calculated results.

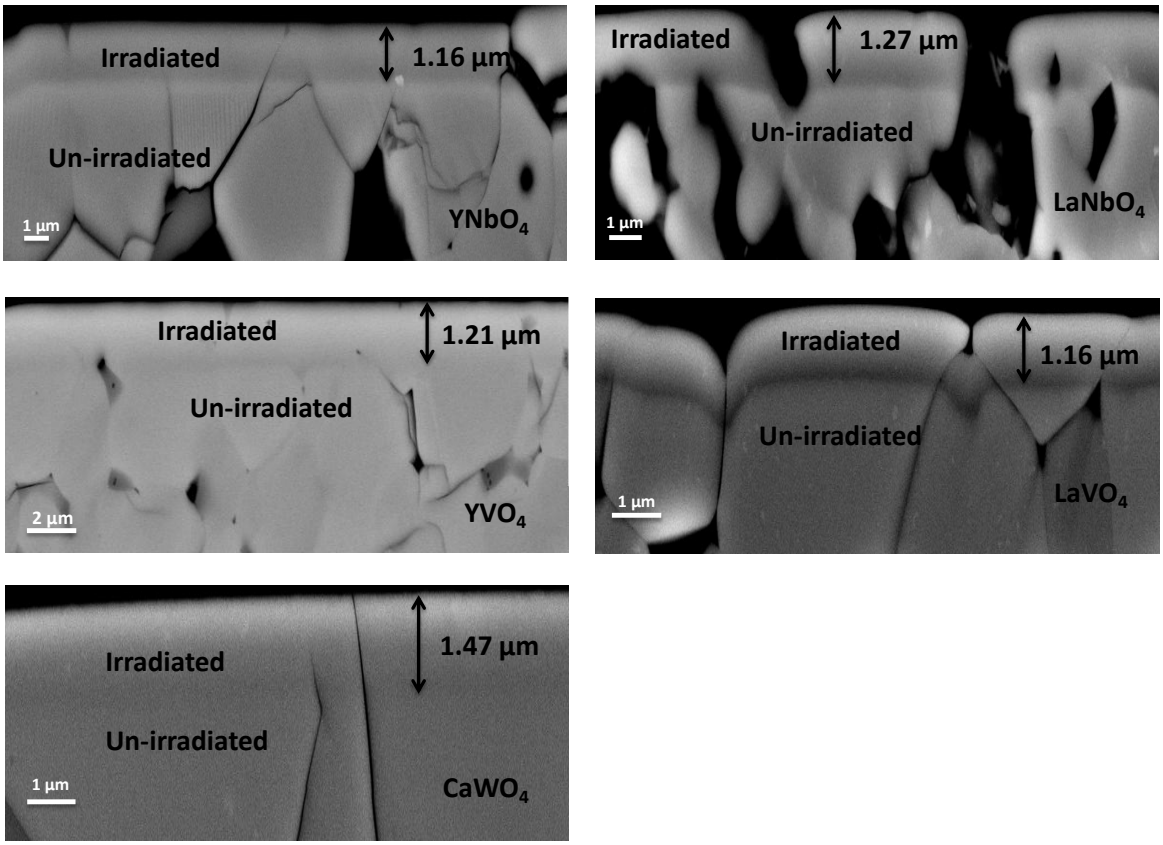

Figure 5.3 Cross-section SEM for ABO_4 compounds, using backscatter mode. The black area at the top of each image is resin, and the damaged layer is from the surface of the sample to where the colour starts change, the remaining area is the polished layer.

5.4.3 Grazing-incidence X-ray diffraction

Grazing incidence X-ray diffraction has been employed to study the change of crystallinity of samples irradiated by Au ions and the results are given in Figure 5.4. A 4 ° incidence angle was selected for analysis, as this interrogates a depth corresponding to the damaging depth of only around 1.2 μm (the depth of detection responding to selected incidence angle for each compound is summarized in Table 5-3, and all GI XRD patterns of the10^{15} ions/cm^2 with different incidence angles are shown in Figure 5.5.), as calculated from X-ray mass absorption coefficients [117]. In the GI XRD pattern (Figure 5.4), all samples showed diffraction peaks gradually disappearing with increasing Au ion fluence. In addition for $YNbO_4$ irradiated to 10^{14} ions/cm^2, two new weak diffraction peaks have emerged centred at 29.2^o and 34.5^o in 2θ, and these peaks disappeared with further irradiation; the peaks may indicate the formation of scheelite-type $YNbO_4$ with tetragonal structure. A broad amorphous hump was observed for $YNbO_4$, $LaNbO_4$ and $LaVO_4$. However, $CaWO_4$ and YVO_4 did not show a clear amorphous hump. The crystallinity has been calculated using both peak intensity and area under the peak for several intense XRD reflections, and consistent results have been found. These results are summarised in Table 5-4. At the highest fluence of 10^{15} ions/cm^2, the estimated remaining percentage of crystallinely (refers to absolute area under peak) in the $CaWO_4$, YVO_4, $LaVO_4$, $YNbO_4$ and $LaNbO_4$ sample was 47%, 46%, 36%, 13%, and 9%, respectively. Samples with a monoclinic crystal system ($LaVO_4$ and both the niobates) were almost completely amorphous even at lower fluence of 10^{14} ions/cm^2, while the samples with tetragonal crystal system ($CaWO_4$ and YVO_4) still have ~50% crystallinity at the highest fluence of 10^{15} ions/cm^2. In addition, $LaVO_4$ displays ~5% increase of crystallinity with both calculated methods from 10^{14} to 10^{15} ions/cm^2 fluence. However, as these crystallinity calculations are only an approximation this is believed to be within error.

During Au ion implantation, the Au ion path through the lattice creates an ion track by displacing the surrounding atoms in the lattice. Those displaced atoms can induce lattice strain and unit-cell volume changes; however, the amount of damage varies throughout the damaged layer. GIXRD provides the entire thickness (depending on incident angle) and thus providing an average picture of the damages. Refining the XRD diffraction peaks can be helpful to quantitate the average volume changes of each sample throughout the damaged layer. In my case, the increase of FWHM (full weight half maximum) can denote as non-uniform strain. FWHM has been calculated using OriginPro 8.6 (the steps to calculate: select 'Single Peak Fit…' under 'Analysis', 'Fitting', and Gaussian function has been selected to simulate the peak shape) for the maximum intensity diffraction peak of each sample. In Table 5-5, $LaVO_4$, YVO_4, and $LaNbO_4$ have shown increased peak width (FWHM) with increasing dose rate however, these increased peak widths were not significant at low dose particularly for YVO_4. On the other hand, $CaWO_4$ which also has tetragonal crystal system showed an obvious increase in FWHM at 10^{14} ions/cm^2 fluence, but further broadening was not obvious at 10^{15} ions/cm^2 fluence. A similar trend was also found in cross-section Raman results (see later) when comparing the width of vibration mode at both ion fluences. With $YNbO_4$, due to the appearance of new weak peaks, only the monoclinic peaks were analysed, and at low and high dose the FWHM decreased to 11% and 6% respectively. Refined lattice parameters were calculated using Rietica program (version 2.1), and the results are listed Table 5-6. The calculated average unit cell volume increases were all less than 0.5%, while, a 0.46% reduction of the $YNbO_4$ unit cell volume at 10^{14} ions/cm^2 fluence was also noted. It should be noted however, that the step size (0.02 ٩) used in the measurements would result in a refined volume error of about 1%, thus unit cell volume changes calculated were within error.

The weak XRD diffraction peaks that have emerged in 10^{14} ions/cm^2 Au irradiated $YNbO_4$ suggest the formation of tetragonal $YNbO_4$. The formation of the new tetragonal $YNbO_4$ (unit cell volume of 289 Å^3 and 293 Å^3 for tetragonal and monoclinic $YNbO_4$) crystal structure may produce local strain at the grain boundary and put pressure on the surrounding grains which may cause the monoclinic unit cell to shrink. In general, ABO_4 compounds, with rare-earth or yttrium at A-site and niobium at B-site, crystallize into two stable fergusonite-related structures: monoclinic (M) and tetragonal (T). The T phase was the high-temperature form of ABO_4 fergusonite. This phase was unquenchable and can be rapidly converted to the M phase by a second order transformation upon cooling [118]. The transition between M and T can be effected quite easily by small movements of atoms, the major change being merely a uniform shear parallel to [100], accompanied by an extension parallel to [010] [119]. The formation of the high temperature phase during the irradiation of oxide ceramics has been seen previously [120, 121].

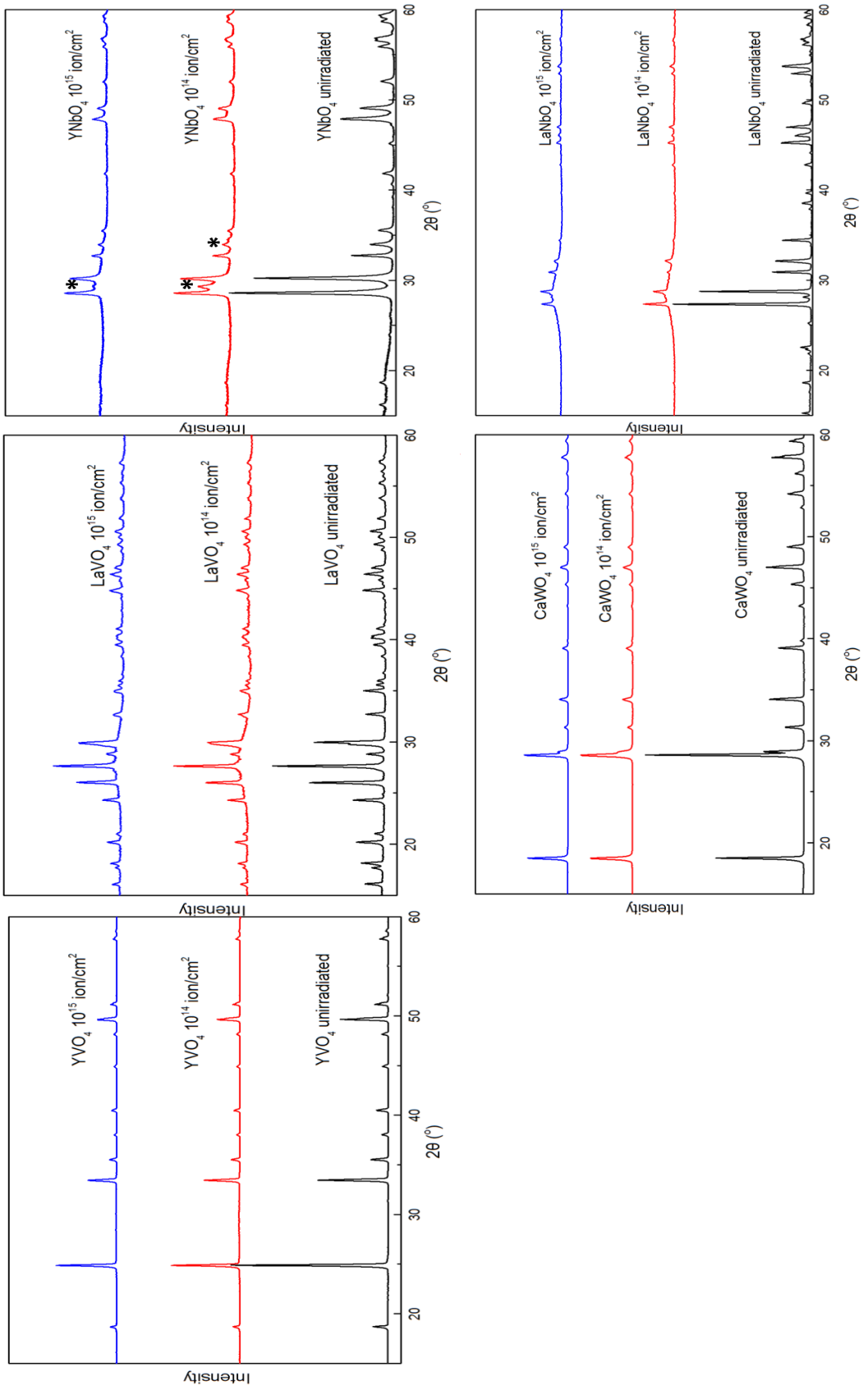

Figure 5.4 GI-XRD patterns for the ABO_4 compounds. $YNbO_4$, $LaVO_4$, and $LaNbO_4$ show an amorphous hump cantered around 27° 2θ and a decrease in reflection intensity,

$CaWO_4$ and YVO_4 only show loss in reflection intensity. The tetragonal phase of $YNbO_4$ was marked as "*".

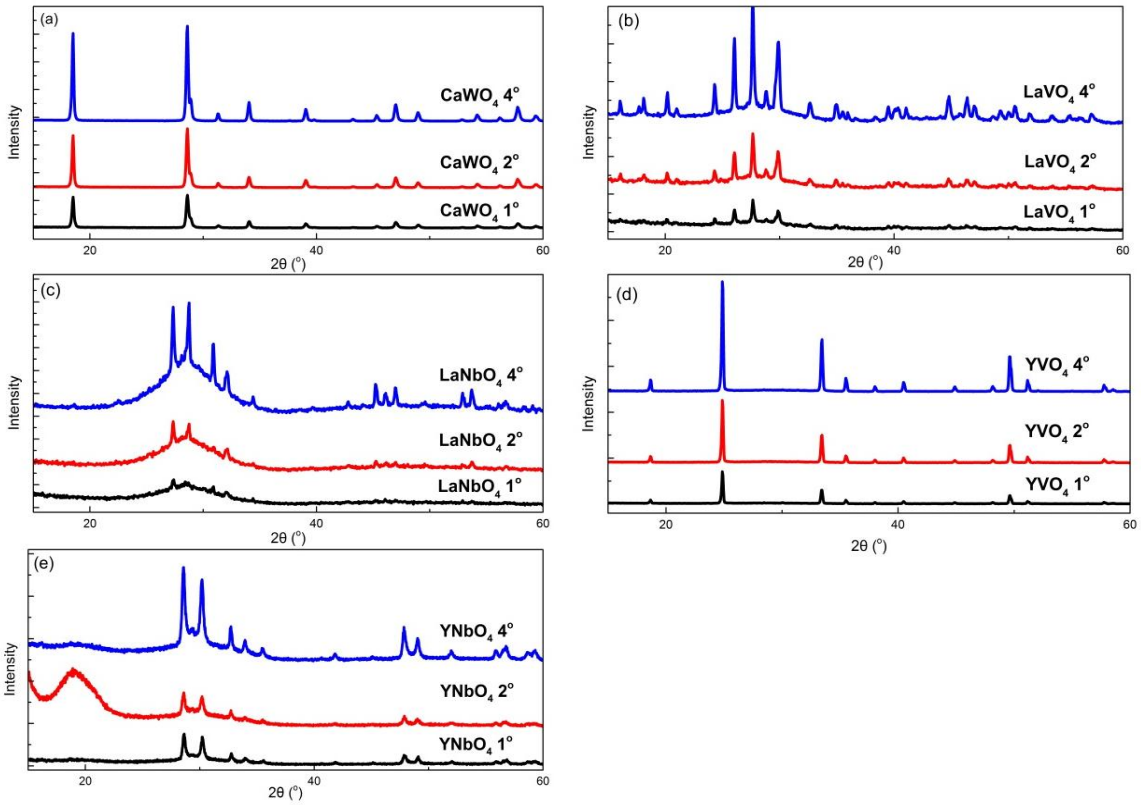

Figure 5.5 GI XRD pattern with various incidence angles (1 °, 2 °, and 4 °) for all samples irradiated to 10^{15} ions/cm^2.

Table 5-3 The X-ray scanning depth calculated using mass absorption coefficient [117] with 1 °, 2 °, and 4 °incidence angle, together with the damage depth observed using SEM.

Sample composition	Incidence angles[1] (μm)			Cross-section SEM (μm)	Ion range from SRIM analysis (μm)
	1 °	2 °	4 °		
$CaWO_4$	0.2	0.42	0.85	1.47	1.9
$LaVO_4$	0.12	0.24	0.48	1.16	1.94
$LaNbO_4$	0.1	0.21	0.43	1.21	1.74
YVO_4	0.33	0.68	1.36	1.27	2.11
$YNbO_4$	0.28	0.57	1.16	1.15	1.85

[1] the density of each sample used in the calculation is from Archimedes' measurements.

Table 5-4 The average crystallinity estimated using both peak intensity and area under the peak for several intense XRD reflections.

Sample		Crystallinity	
		Average peak intensity	Absolute area under peak
$CaWO_4$	Un-irradiated	100%	100%
	10^{14} ions/cm^2	46%	64%
	10^{15} ions/cm^2	43%	47%
YVO_4	Un-irradiated	100%	100%
	10^{14} ions/cm^2	49%	50 %
	10^{15} ions/cm^2	43%	46%
$LaVO_4$	Un-irradiated	100%	100 %
	10^{14} ions/cm^2	30%	32 %
	10^{15} ions/cm^2	37%	36 %
$LaNbO_4$	Un-irradiated	100%	100 %
	10^{14} ions/cm^2	6%	10 %
	10^{15} ions/cm^2	5%	9%
$YNbO_4$	Un-irradiated	100%	100 %
	10^{14} ions/cm^2	20%	16%
	10^{15} ions/cm^2	14%	13 %

Table 5-5 FWHM for the maximum intensity diffraction peak of each ABO_4 compound.

Sample		Peak position	FWHM	Error	Broaden (%)
$CaWO_4$	Un-irradiated	28.611(3)	0.15708	0.01094	
	1e^{14} ions/cm^2	28.577(4)	0.21553	0.01607	37.21%
	1e^{15} ions/cm^2	28.585(4)	0.18447	0.01262	17.44%
YVO_4	Un-irradiated	24.877(1)	0.15771	0.00434	
	1e^{14} ions/cm^2	24.868(2)	0.16019	0.00516	1.57%
	1e^{15} ions/cm^2	24.866(2)	0.16199	0.00503	2.71%
$LaVO_4$	Un-irradiated	27.636(2)	0.18622	0.0051	
	1e^{14} ions/cm^2	27.635(1)	0.18623	0.00527	0.01%
	1e^{15} ions/cm^2	27.651(2)	0.2099	0.00494	12.72%
$LaNbO_4$	Un-irradiated	27.329(3)	0.17251	0.00811	
	1e^{14} ions/cm^2	27.345(3)	0.18	0.00832	4.34%
	1e^{15} ions/cm^2	27.346(5)	0.2044	0.01346	18.49%
$YNbO_4$	Un-irradiated	28.608(1)	0.27123	0.0052	
	1e^{14} ions/cm^2	28.595(6)	0.24189	0.0179	-10.82%
	1e^{15} ions/cm^2	28.584(2)	0.25464	0.0075	-6.12%

Table 5-6 Lattice parameters for all ABO4 compounds.

Sample		Lattice Parameter			Angles	Volume	%
		a	b	c	β		
$CaWO_4$	Un-irradiated	5.272 (1)	5.272(1)	11.41(1)	90	317.24(4)	
	$1e^{14}$ ions/cm^2	5.279(1)	5.279(1)	11.42(1)	90	318.32(5)	0.34
	$1e^{15}$ ions/cm^2	5.277(1)	5.277(1)	11.42(1)	90	318.06(3)	0.26
$LaVO_4$	Un-irradiated	7.081(1)	7.317(1)	6.764(1)	104.92(1)	338.67(3)	
	$1e^{14}$ ions/cm^2	7.084(1)	7.317(1)	6.765(1)	104.99(1)	338.72(4)	0.01
	$1e^{15}$ ions/cm^2	7.081(1)	7.316(1)	6.768(1)	104.95(1)	338.95(1)	0.08
YVO_4	Un-irradiated	7.151(1)	7.151(1)	6.323(1)	90	323.35(3)	
	$1e^{14}$ ions/cm^2	7.152(1)	7.152(1)	6.324(1)	90	323.45(7)	0.03
	$1e^{15}$ ions/cm^2	7.153(1)	7.153(1)	6.328(1)	90	323.78(2)	0.13
$LaNbO_4$	Un-irradiated	5.590(1)	11.572(1)	5.222(1)	94.07(1)	336.96(4)	
	$1e^{14}$ ions/cm^2	5.588(1)	11.582(1)	5.227(1)	93.95(1)	337.55(8)	0.18
	$1e^{15}$ ions/cm^2	5.592(1)	11.580(1)	5.227(1)	93.99(1)	337.69(9)	0.22
$YNbO_4$	Un-irradiated	7.040(1)	10.956(1)	5.297(1)	134.11(1)	293.34(3)	
	$1e^{14}$ ions/cm^2	7.066(1)	10.963(1)	5.282(1)	134.48(1)	292.0(1)	-0.46
	$1e^{15}$ ions/cm^2	7.049(1)	10.97(1)	5.307(1)	134.27(1)	293.76(7)	0.14
$YNbO_4$	$1e^{14}$ ions/cm^2	5.231(1)	5.231(1)	10.866(2)	90	297.4(2)	

5.4.4 Cross-section Raman

Raman spectroscopy has been used to study the shorter correlation length scale of a few unit cells of the ABO_4 samples. Micro-Raman analysis was measured on the cross-sectioned pellets at different depths from the damaged surface, to study the effect of radiation damage on all samples. In the selected ABO_4-type materials there are mainly two crystal structures, therefore each of the crystal structures will first be described based on their Raman vibration modes. As shown in Figure 5.6, the fingerprint region for the compositions is between 70 and 1000 cm^{-1} phonon frequency. $CaWO_4$ and YVO_4 have tetragonal structure with I 41/A and I 41/AMD space group respectively. In the experiment there are five bands of internal vibration for both WO_4 and VO_4 ionic group, and two external bands which are free rotation and translation modes. $LaNbO_4$, $YNbO_4$, and $LaVO_4$ all have monoclinic structures with I 2/C, C 2/C, and P 21/N space group respectively. By observation, the internal vibration modes of NbO_4 and VO_4 groups appear between ~200 and 1000 cm^{-1} phonon frequency. In the internal vibration mode range, it is only possible to distinguish the motion of the O-V-O bond for $LaVO_4$ i.e. bending or stretching.

Raman spectroscopy has been used to study the effect of self-radiation, swift ion and ion irradiation on many forms of ceramics. Often, materials undergoing radiation damage have shown loss of short range order (broadening of Raman modes), decrease of Raman intensity and sometimes decrease in phonon frequency. In general, for samples studied in this work with monoclinic structure (i.e. $LaNbO_4$, $YNbO_4$, and $LaVO_4$) I observed:

(a) A broad hump centred around V_1 mode and significant mode broadening

(b) Increased asymmetry of the broadened band at symmetric stretching modes

(c) Loss of all Raman mode intensity with increased Au ion fluence

On the other hand, samples with tetragonal structure showed only a decrease of Raman mode intensity with increasing fluence and less significant band broadening, suggesting that the damage did not completely destroy the bonding for the fluences investigated. This is in agreement with that observed from GI XRD analysis. Again, by using OriginPro 8.6 to calculate the V_1 mode band width (FWHM) for each sample, the results show an overall broadening with increasing fluence.

Samples with a monoclinic structure have exhibited a broad hump centred at V_1 mode; however, a sample with tetragonal structure did not show this. As listed in Table 5-7 the band width of the most intensive vibration mode (V_1-symmetric stretching mode) for all spectra of each composition was compared. Tungstates and vanadates showed less broadening with increasing ion fluence (overall broadening of 0.9 ± 0.3 cm^{-1} for $CaWO_4$ 1 ± 0.3 cm^{-1} for $LaVO_4$ and 1.4 ± 0.2 cm^{-1} for YVO_4). Whereas, niobates have much larger broadening (overall broadening of 4.2 ± 1 cm^{-1} for $LaNbO_4$, 2.3 ± 0.3 cm^{-1} for $YNbO_4$) with increasing ion fluence. Meanwhile, the phonon frequency of each of the vibration modes of the samples was analysed. There was small phonon frequency shifts of the V_1 mode observed for all spectra of all samples (see Table 5-7). Samples with monoclinic structure (without $LaNbO_4$, its shift was insignificant) have an overall ~1 cm^{-1} down-shift with the shift order for $LaVO_4$ > $YNbO_4$. On the other hand, YVO_4 and $CaWO_4$ showed very small phonon frequency shift. It should also be noted that, (a) the band width and phonon frequency was fitted using Gaussian function in OriginPro 8.6, and (b) the implantation depth is expected to be about 1.2 μm for $CaWO_4$, and the limit of the detecting laser size is only ~1.5 μm in diameter, therefore the interrogation of the damage layer may have a small portion of un-damaged materials been examined.

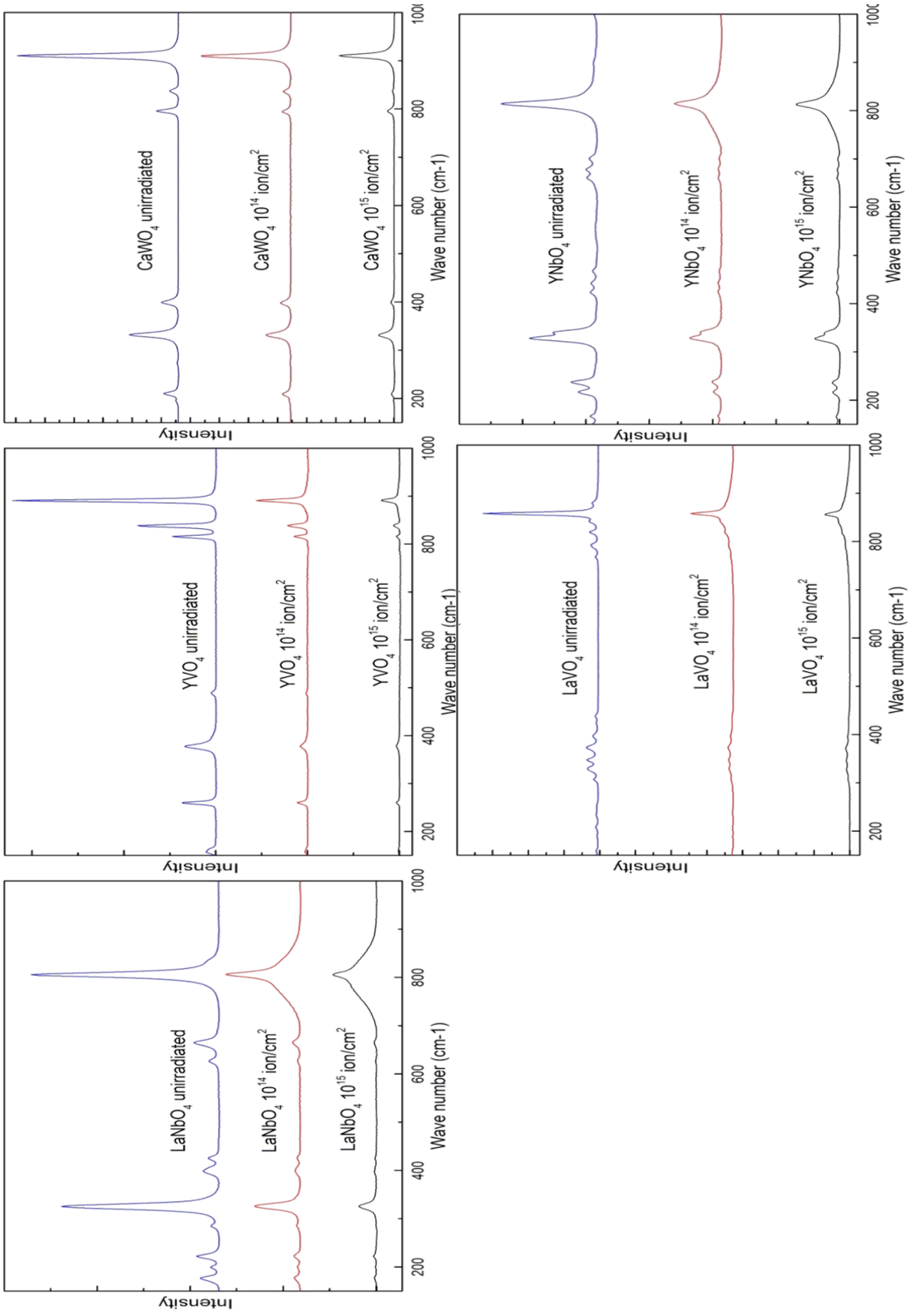

Figure 5.6 Cross-section Raman for ABO_4 compounds. The irradiated pattern for each compound was taken from within the damage layer for each sample.

Table 5-7 Phonon frequency and FWHM of V_1-symmetric stretching mode for each sample with increasing Au-ion fluence.

Sample		Phonon Frequency cm^{-1}	FWHM
$CaWO_4$	Un-irradiated	909.9(1)	9.8(2)
	$1e^{14}$ ions/cm^2	909.4(1)	10.3(2)
	$1e^{15}$ ions/cm^2	910.1(1)	10.7(3)
YVO_4	Un-irradiated	890.6(1)	6.4(1)
	$1e^{14}$ ions/cm^2	890.6(1)	7.4(2)
	$1e^{15}$ ions/cm^2	890.9(1)	7.8(2)
$LaVO_4$	Un-irradiated	857.9(1)	6.2(3)
	$1e^{14}$ ions/cm^2	857.7(1)	6.5(2)
	$1e^{15}$ ions/cm^2	856.2(1)	7.2(3)
$LaNbO_4$	Un-irradiated	805.8(3)	12.8(3)
	$1e^{14}$ ions/cm^2	805.7(2)	14.6(2)
	$1e^{15}$ ions/cm^2	804.8(4)	17(1)
$YNbO_4$	Un-irradiated	814.0(2)	17.2(5)
	$1e^{14}$ ions/cm^2	813.8(2)	19.5(7)
	$1e^{15}$ ions/cm^2	812.9(2)	19.5(6)

5.4.5 Thermal annealing after ion irradiation

The most heavily damaged samples (10^{15} ions/cm^2) were thermally annealed in air at temperatures from 200 to 1200°C for 2 hours, and the recrystallization and structural recovery from the ion beam irradiation was studied by GI-XRD (all measurements were under the same condition, with 4 °glancing angle). The patterns for each composition are shown in Figure 5.7. $CaWO_4$ and YVO_4 have a sudden jump in crystallinity after 200 ℃ and 400 ℃ annealing heat treatment, respectively. $LaVO_4$, $LaNbO_4$ and $YNbO_4$ showed a gradual increase in crystallinity on annealing at theses temperatures. The degree of crystallinity was determined by comparing the GI-XRD peak intensities of the annealed and un-irradiated samples (Figure 5.8). The $YNbO_4$ and $LaNbO_4$ tetragonal phases were

observed at 600 ℃ and 800 ℃ annealing temperatures, respectively, and the tetragonal peaks were not included in the (monoclinic) crystallinity calculation. All samples showed an almost complete re-crystallization after 1200 ℃ annealing for 2 hours. In addition, $LaVO_4$ regain crystallinity after an 800 ℃ annealing heat treatment.

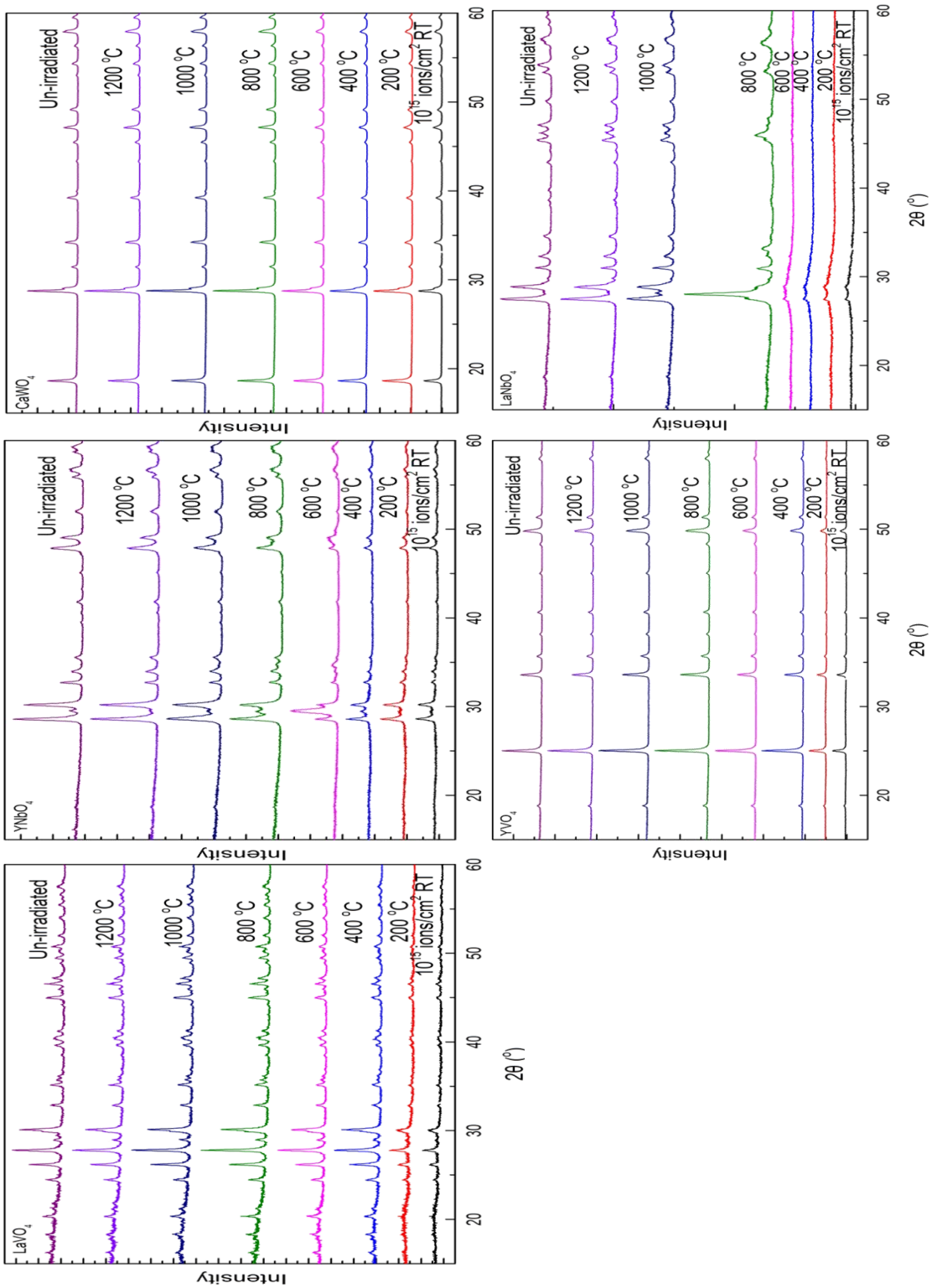

Figure 5.7 Temperature evolution of the GI-XRD data of all samples with a fluence of 10^{15} ions/cm^2 with 2 hours annealing at each temperature.

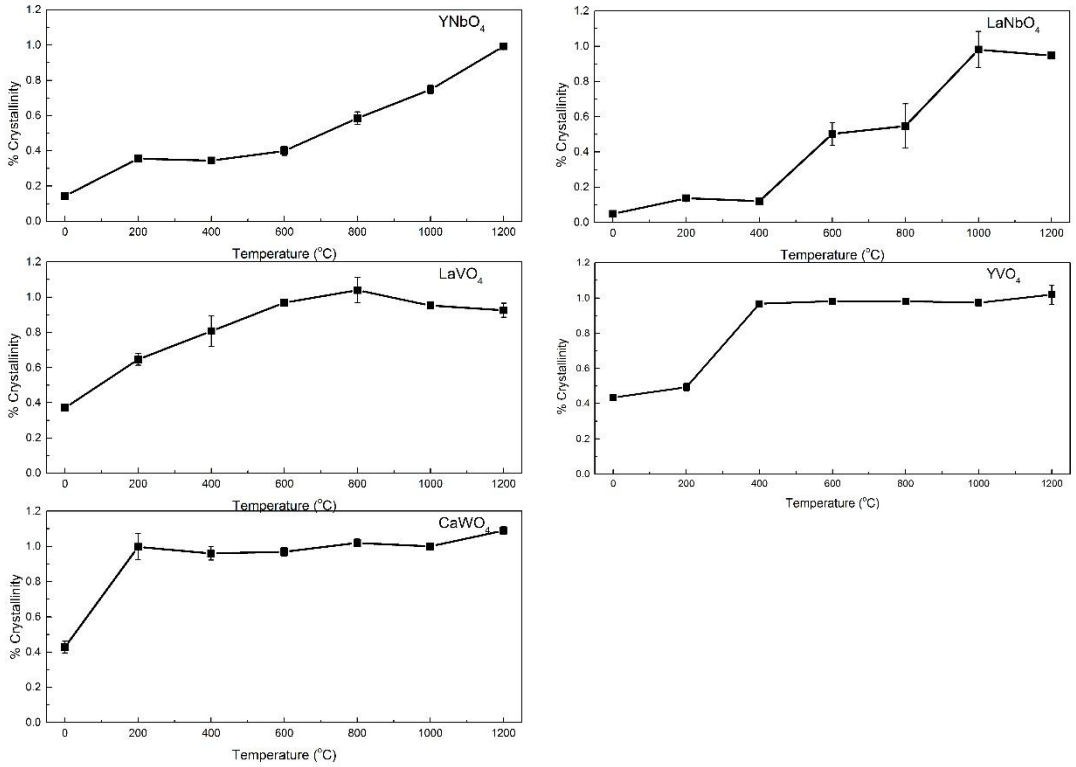

Figure 5.8 The crystallinity changes with annealing temperature of all ABO_4 samples.

5.5 Discussion

Irradiation by Au-ions was intended to simulate the recoil particle during α-decay process. The energy deposited into the material following Au-ion irradiation derives from electronic interactions and nuclear displacements. Some of the total energy from the former is released in the form of heat, and the nuclear displacements results in the displacements of the atoms which are knocked from their crystal sites by the Au-ions. There is about 70% of total energy deposited through electronic interactions and about 30% through nuclear displacements according to the SRIM data shown in Table 5-1. The travel distances of the implanted ion for the samples were measured by SEM to be around 1.2 μm for $CaWO_4$ (expected to be 1.4 μm from SRIM). Results of GI-XRD and cross-sectional Raman of all samples show varying damage through loss of long and short range

order, insignificant unit cell volume expansion, and in general the tetragonal structure appeared to have a better radiation tolerance than the monoclinic structure.

From GI XRD data no peak shifts were observed that occurred at lower angles (as determined within my experimental limitations). However, the peaks in the pattern at higher angle show some evidence of asymmetric broadening towards a lower angle (see Figure 5.9), except for YVO_4 (not shown). The XRD peak shape is affected by both crystallite size and lattice strain [122]. Lattice strain can be caused by dislocation loops and point defect accumulation [123] and volume changes during the crystalline to amorphous transition. In addition, $LaNbO_4$ and $YNbO_4$ have shown a clear increase of peak width for the peak with maximum intensity, suggesting point defect and dislocation density accumulation.

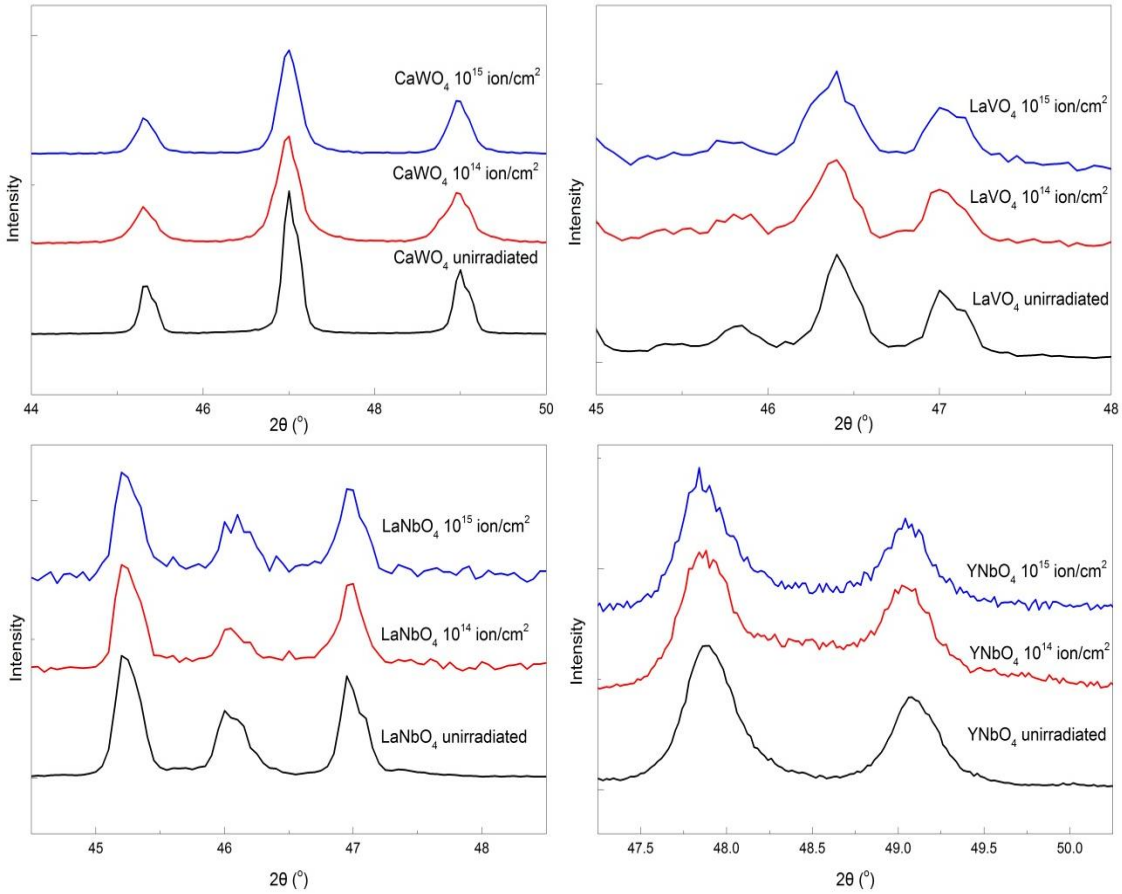

Figure 5.9 GI XRD data in the 44 °-50° 2θ range for $CaWO_4$, $LaVO_4$, $LaNbO_4$, and $YNbO_4$. The incident angle is 4 °.

The Raman results (see Figure 5.6) for the damaged $LaNbO_4$ $YNbO_4$ and $LaVO_4$ samples suggest two phases: one is the crystalline phase (monoclinic) which shows all bond vibration modes, the other phase is distorted where bands are broadened and shifted. The V_1 vibration mode for monoclinic structured samples shows significant broadening. The band broadening of the V_1 mode indicates the loss of short-range order following Au ion irradiation (point defect accumulation and distortion of the BO_4 tetrahedra). The decrease of phonon frequency indicates the lengthening of B-O bonds (i.e. $LaVO_4$ (V-O) and $YNbO_4$ (Nb-O)), which is caused by an increase of distortion of the B-O tetrahedra and stress produced by the volume change during amorphization [67, 124]. At highest fluence,

scheelite $CaWO_4$ and zircon-type structured YVO_4 have shown a decrease of Raman band intensity and slight band broadening for all vibration modes; both the samples have the tetragonal crystal system. Zhang et al. [125] concluded that natural Sri Lanka zircons lost short range order and become amorphous at a dose of 6.3 x 10^{18} α-events g^{-1}, and remain amorphous with a higher dose. For the samples with the monoclinic crystal system ($LaVO_4$, $LaNbO_4$, and $YNbO_4$) an amorphous hump near V_1 mode is observed after the maximum irradiation dose. This is in agreement with Nasdala et al. [67], who used both bulk and thin lamellae monazite ($CePO_4$) samples to study irradiation damage by Au ions (1-7 MeV, at room temperature); with their bulk samples at a highest fluence of 5.1 x 10^{14} ions/cm^2 the Raman spectra did not show a V_1 mode shift, however the lamellae sample displayed a small V_1 mode down-shifted (from ~970 to 960 cm^{-1}). Both bulk and lamellae showed increases in the FWHM of V_1 mode from 2.3 cm^{-1} to 2.5 cm^{-1} and an 'amorphous' hump was noted. The explanation given by Nasdala is that the Raman results of the bulk sample interrogate part of the undamaged material, as well as the damaged zone. A similar explanation could be used in my case, as the beam size used for Raman analysis (~1.5 μm) was of a similar size to the damaged zone.

YVO_4 and $LaVO_4$ samples both have VO_4 tetrahedra but because of the r_A/r_O ratio difference, their crystal structures are different. However, at a fluence of 10^{15} ions/cm^2, YVO_4 showed more calculated crystallinity than $LaVO_4$. Further, no amorphous hump was observed in the GI-XRD patterns. Also the Raman results showed significantly more damage to the V-O bond in the $LaVO_4$ sample irradiated with the 10^{15} ions/cm^2 fluence (i.e. phonon frequency down-shift and band broadening are observed). These results suggest that the zircon-type-vanadates have higher tolerance under irradiation than monazite-type-vanadates. The effect of ion irradiation in certain energy ranges appears to improve defect recombination in many ceramic oxides. Meldrum et al [69] observed that

generally the critical temperatures (T_c) for lanthanide phosphates with a monazite-structure are lower than those for the zircon-structure materials. Also, T_c decreases uniformly as ENSP increases, and their results agree with those of Zinkle [126, 127]. Interestingly, the observations on vanadates were the opposite with regard to structure type and the zircon structured vanadates were seen more radiation tolerant than the monazite structured vanadates. A possible reason for the different observation could be due to the B-site chemistry difference. $LaPO_4$ with monazite structure appears to be completely amorphized (5 MeV, Au ion) at a fluence 7.2 x 10^{14} ions/cm^2 [68], whereas $LaVO_4$ was found to still have 30% crystallinity even at a fluence of 10^{15} ions/cm^2. The different ENSP ratios may have play a part in the explanation, however more detail is required in order to understand this fascinating and exciting observation.

The results suggest materials with tetragonal structure have more radiation tolerance under Au ion irradiation than monoclinic systems, however, the changes of crystal structure and space group (zircon I41/AMD and scheelite I 41/A) will have further impact on their physical properties. For example, a comparison of zircon and scheelite ABO_4 compounds showed that the scheelite type structure has higher density, slightly larger A-O and B-O bond lengths, and slightly higher thermal expansion coefficient than the zircon type structure [128, 129]. For the application of immobilization of nuclear wastes, a stable crystal structure (for example low thermal expansion coefficient, low critical amorphization temperature, chemical stability) under radiation must be achieved. If the sample does go amorphous it is important that the radioactive materials are maintained and do not leach out into ground stratum. Mechanical testing and leaching experiments should be carried out as future work.

$LaNbO_4$ and $YNbO_4$ have the same crystal structure; therefore, the A-site atom difference likely drives the differences in radiation tolerance of the samples. The calculated amorphous fraction for $LaNbO_4$ and $YNbO_4$ increased with increasing ion fluence, with about a 90% and 80% amorphous fraction, respectively even at 10^{14} ions/cm^2 fluence. Similar conclusions were found from Raman results (refer to table 5-7) although less band broadening was observed in $YNbO_4$ than $LaNbO_4$. In this case my results agree with Meldrum et al [69], who plotted the A-site atom mass of lanthanide phosphates vs Tc (the temperature above which amorphization was not induced). Their results suggest that the higher atomic weight, the easier the crystalline to amorphous phase transformation can occur (same irradiation condition, e.g. temperature, ion energy) [69].

$YNbO_4$ at fluence 10^{14} ions/cm^2 showed evidence for a second order phase transformation. The XRD results suggest some of the material phase changes from monoclinic to tetragonal crystal structure (mainly via the appearance of two new monoclinic peaks centred at 29.2^o and 34.5^o in 2θ), and at higher fluence the intensity of these characteristic tetragonal peaks then decreased. The Raman observations could not confirm such a phase transformation as these two crystal systems have similar vibration frequencies. For example, Dymshits et al [130] have shown Raman spectroscopy of monoclinic $YbNbO_4$ and metastable tetragonal $YbNbO_4$ have similar vibration frequencies. An in situ study of the phase transformation of $YNbO_4$ undertaken by K. Jurkschat suggested the monoclinic to metastable tetragonal phase change occurs around at 860 ℃ in normal atmosphere [131]. Mather and Davies [118] used a Sol-gel method to study the crystallization upon heating of fergusonite-related structures, and in their differential thermal analysis results, upon heating to the range 500-600 ℃ a metastable tetragonal (T) structure is first produced from amorphous precursors; with continued heating the metastable T phase then start to phase transformation to monoclinic (M) phase at 750-800 ℃, and eventually M

phase was observed at 850 ℃. Also, Kriven et al. [132] suggested that the phase transformation involves a small distortion caused by slight displacement of the atoms in the parent phase. Serval authors [120, 121, 133] have studied phase transitions under irradiation on zirconia. Benyagoub [133] suggested a "thermal spike" model, which assumes that as the ion just passes an atom in the lattice, a fraction of electronic energy loss is converted to heat for the atomic lattice The phase transition can occur in the heated region if the lattice temperature exceeds the phase transition temperature. Simeone et al [120] suggested a microscopic model to explain the phase transition with irradiation. Defects are produced in the oxygen sub-lattice, and these defects generate a local strain field which lowers the critical phase transformation temperature and it quenches the tetragonal (zirconia) phase at room temperature. Although a similar argument may be used to explain the observation of the phase transition on $YNbO_4$, further work is required and this may involve in situ TEM or similar irradiation experiments.

From thermal annealing experiments, $YNbO_4$ and $LaNbO_4$ have shown a formation of tetragonal phase from their amorphous state at temperatures of 600 and 800 ℃, respectively, at high temperatures (800 ℃ for $YNbO_4$, and 1000 ℃ for $LaNbO_4$) the monoclinic structure reforms. Monoclinic structure appears as annealing temperature increased. This agrees with the results of Mather and Davies [118] for sol-gel synthesised fergusonite-related phases. $CaWO_4$ has shown a very low recovery temperature, it may due to low defect diffusion activation energy in the scheelite crystal. $CaWO_4$, YVO_4 and $LaVO_4$ were completely re-crystallized after 2 hours at 800 ℃. It is clear that chemical effects were more significant than the structure difference when it came to thermal annealing.

5.6 Summary

Various kinds of compositions and structures ABO_4 compounds were made using solid state synthesis methods and these have been irradiated with 5 MeV Au ions to simulate the effects of α-decay. $LaVO_4$, $LaNbO_4$, $YNbO_4$ with monoclinic structure showed long- and short-range order loss upon irradiation. $CaWO_4$ and YVO_4 with tetragonal structure showed less damage when compared to the monoclinic variants. Moreover, their radiation tolerance was very pronounced, where undergo 10^{15} ions/cm^2 dose with about ~3 dpa damage level did not provide complete amorphization. It is necessary to carry out further radiation behaviour investigations of these compounds. Chemical effects were more significant in annealing experiments than the structure difference.

6. Gold Ion Beam Irradiation Effects on Scheelite and powellite type structures

6.1 Introduction

The ABO_4 tungstate and molybdate families have attracted significant interest for several decades. This interest has been driven by the fact that these materials have excellent optical and luminescence properties, and have applications as laser host materials [134], scintillation detectors [135], and phosphors [136]. The common form of tungstates and molybdates in nature is as $CaWO_4$ and $CaMoO_4$ or so-called scheelite and powellite minerals, often containing uranium or thorium. Most of these minerals are found amorphous in nature having lost their crystallinity through α-decay of the incorporated uranium and thorium [66, 137, 138]. These types of ABO_4 compound provide excellent models for studying the long-term stability and durability of oxide ceramics. Also, this type of compound can incorporate actinides within their crystal structure, and as such are potential ceramic phases for the incorporation of actinides in ceramic nuclear waste forms.

In these scheelite and powellite structured compounds (Space Group I41/a, Z = 4), oxygen atoms form a distorted simple cubic arrangement; BO_4^{2-} anion tetrahedra are surrounded by A^{2+} cations with eightfold coordination, and the A and B sites have S_4 point symmetry. The BO_4^{2-} tetrahedra have short B-O bond lengths (approximately 1.77 Å) and the A^{2+} is loosely bonded [139].

A few studies have investigated the effect of damage accumulation on the luminescence properties of single crystal calcium molybdate and the results indicate the threshold fluence for defect formation is about 1×10^{15} ions/cm^2 [140]. However, there is very limited work on the effect of ion beam irradiation on scheelite type materials. $ThGeO_4$ with the scheelite structure was implanted with swift heavy ions (93 MeV Ni^{7+}) and the

amorphization fluence at room temperature was determined to be 7.5 x 10^{16} ions/cm^2 [141].

The α-decay process in minerals includes simultaneously releasing one energetic α-particle ($^4_2$He of normally 4-5 MeV), and one heavy ion with low energy (about 70-100 KeV recoil atom) [113]. In general for ceramic materials, most of the damage is caused by the heavy recoil nucleus which will have a stopping range of approximately 20-25 nm and will cause around 1000 atom displacements. The α-particle range is much longer at around 10-15 μm with most of its energy deposited through electronic stopping processes [113]. In the present study gold ion-beam irradiation was used to simulate the effect of the recoil nucleus in cumulative α-decay on tungstate and molybdate ABO_4 type structures. In the previous chapter the scheelite ($CaWO_4$) structures was further investigated in regard to the radiation behaviour. In order to gain insight into the radiation tolerance of these structure types, a range of compositions were selected: AWO_4 and $AMoO_4$ where A = Ca, Sr, and Ba.

6.2 Experimental section

The raw materials used for the synthesis of the ABO_4 compounds (A = Ca, Sr, and Ba; and B = W, and Mo) were ammonium molybdate, tungsten trioxide, calcium, strontium and barium nitrates. The $AMoO_4$ samples were prepared by first dissolving stoichiometric amounts of ammonium molybdate into 25% ammonia solution by stirring at 70 ℃. $A(NO_3)_2$ was dissolved in distilled water and added to the molybdate solution with stirring to form a white precipitate. The mixtures were stir dried at 70 ℃. The solid was calcined for 5 hours at 500 ℃ (5 ℃/min ramp rate). The calcined powder was then milled using yttria-stabilized zirconia balls in cyclohexane for 2 h and dried at 100 ℃. The powder was

pelletized using a uniaxial press with ~2.5 MPa pressure, and sintered at 1200 ℃ for 12 hours (5 ℃/min ramp rate) in air. The AWO_4 samples were prepared similarly but with the following changes: (a) WO_3 was dissolved in 25% ammonia solution and (b) sintering was undertaken at 1300 ℃ for 12 hours (5 ℃/min ramp rate) in air.

The samples were characterized by XRD, SEM and Raman for compositional and structural analysis, and the density of all samples was measured using Archimedes' method.

6.3 Ion beam irradiation

Ion irradiation experiments were carried out in order to simulate the effect of the α-recoil nucleus during α-decay. Au ions with 12 MeV were selected to simulate the α-recoil events which have energy between 70 and 100 KeV. The kinetic energy from these particles is deposited in the host material by ballistic (E_{nucl}) and electronic (E_{elec}) excitation processes [114].

Au ions have a similar mass compared to the α-recoil atom; however the low energy (~70-100 KeV [113]) in the actual event will only penetrate 20-25 nm which restricts the achievable characterization of the damage layer. Therefore, increasing the energy of the implanted Au ion can provide a thicker layer of damaged material which can be characterised by XRD, SEM, and Raman spectroscopy. Here 12 MeV Au ions were used in order to provide a reasonably thick damaged layer that allows for various characterisations. It should be noted that the ballistic to electronic energy ratio as calculated from SRIM 2013 for the 12 MeV Au ions is quite different to that of a recoil nucleus in α-decay. Table 6-1 summarizes the depth profile and energy fraction, and shows that for 12 MeV Au ions (used in my study); the energy transfer by electronic

excitation was higher than that for an alpha recoil atom. Although the damage mechanism maybe affected by altering the implantation energy, the expectation of amorphization displacements will be similar for Au ions and recoil atoms. The ion fluences were chosen to match a similar displacement per atom (dpa) value which would be produced over several hundreds of years in a waste form matrix containing ~10 wt % minor actinide oxide [68, 115], i.e. a corresponding nuclear damage of the order of 1 dpa. Both electronic and nuclear stopping power and dpa at the various investigated fluences can be calculated from SRIM and these values are listed in Table 6-1 [116, 142].

Table 6-1 Depth profile and energy fraction based on SRIM 2013 simulation [116, 142][1]

Sample	Peak damage depth (um)	Ion range (μm)	Dpa (ions/cm^2)		f_{nucl} (%)	f_{elec} (%)	dE/dx (eV/Ang)		ENSP
			10^{15}	10^{16}			Nuclear	Electron	
$CaWO_4$	1.56	2.1	2.6	26.2	28.3	71.7	202	363	1.8
$SrWO_4$	1.65	2.1	2.6	26.1	28.5	71.5	199	357	1.8
$BaWO_4$	1.68	2.2	2.6	25.8	28.3	71.7	188	342	1.82
$CaMoO_4$	1.8	2.2	2.8	27.5	26.9	73.1	172	374	2.17
$SrMoO_4$	1.77	2.3	2.3	22.6	27.3	72.7	174	371	2.13
$BaMoO_4$	1.74	2.3	2.4	24.0	27.2	72.8	168	356	2.13

[1] The calculations for ABO_4 samples used 50 eV displacement energies for every element, and the density was calculated from the XRD pattern by refining lattice parameters.

6.4 Results

6.4.1 Un-irradiated samples

The XRD patterns for all pristine scheelite-ABO_4 compounds in this study are shown in Figure 6.1. All samples appear single phase except for $CaWO_4$ which shows trace quantities of WO_3. The XRD patterns for all samples show tetragonal symmetry with the I41/a space group confirming the scheelite and powellite structures.

SEM-EDS (Scanning Electron Microscopy with X-ray microanalysis) were used to examine the phase purities of the samples (see Figure 6.2). As suggested by XRD analysis, the $CaWO_4$ sample showed trace quantities of WO_3 (<2%). Further, trace impurities were detected in the $CaWO_4$, $BaMoO_4$ and $BaWO_4$ samples. The impurities contained the elements Mg, Fe, Al, Si, and Na and their presence is likely due to cross contamination during sample preparation. However, the impurities were rarely observed and appeared as the small particles on a grain boundary. All other samples appeared single phase and EDS analysis suggested perfect stoichiometric ratios 1:1 (A:B) for all samples. The bulk density of each sample was measured in triplicate by Archimedes' method and the results are listed in Table 6-2.

Table 6-2 Porosity and bulk density.

Composition	Theoretical Density* (g/cm^3)	Measured Density (g/cm^3)	%Theoretical
$CaWO_4$	6.15	5.43	88
$SrWO_4$	6.35	5.37	85
$BaWO_4$	6.37	5.75	90
$CaMoO_4$	4.28	3.99	93
$SrMoO_4$	4.74	4.19	89
$BaMoO_4$	5.01	4.27	86

*Calculated from unit cell parameters.

Figure 6.1 XRD patterns for the pristine ABO_4 compounds. Reflections from a second

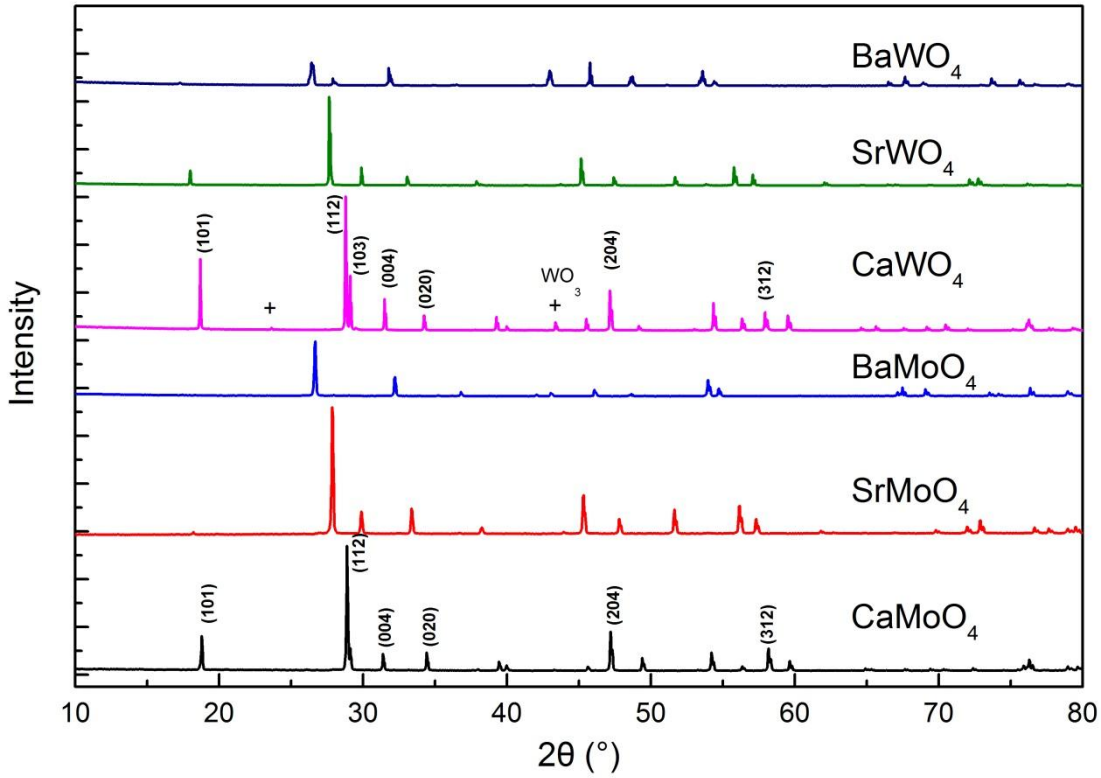

phase in the $CaWO_4$ are indicated by +.

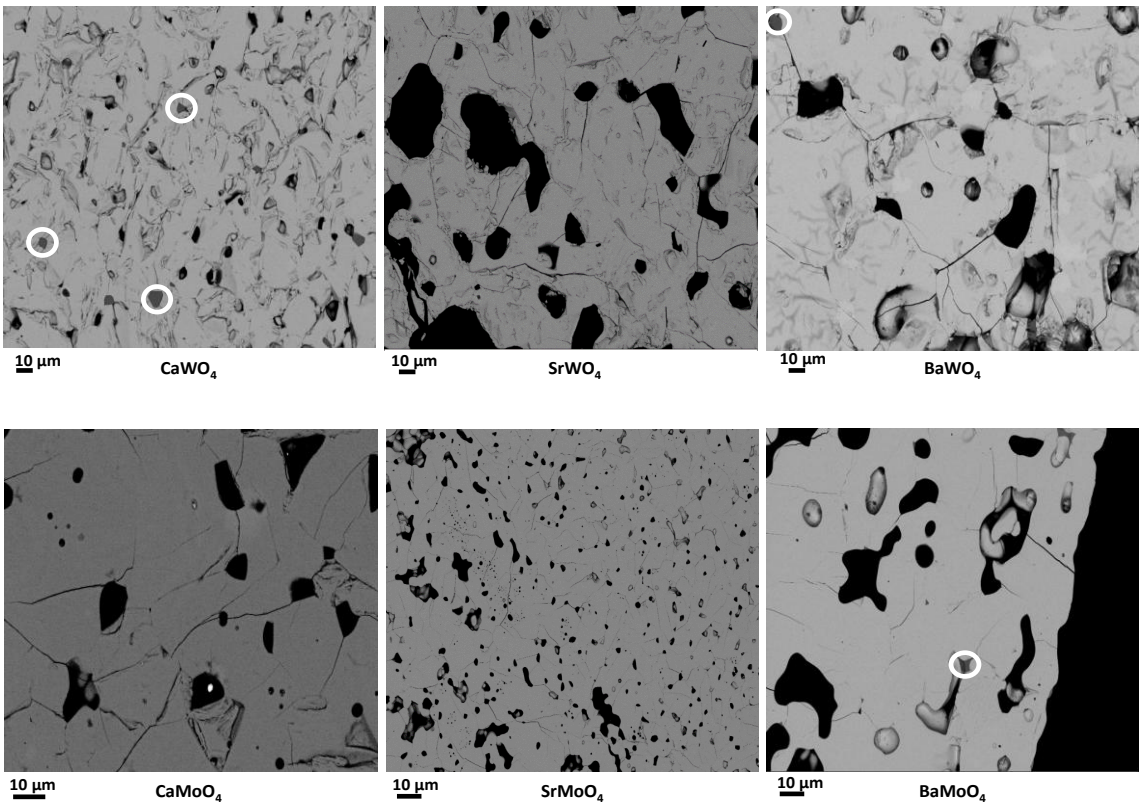

Figure 6.2 Backscattered SEM images for the pristine ABO_4 compounds. The main grey phase is the target phase and the traces of impurity phases are circled. Black areas are pores.

6.4.2 Ion-irradiated samples

Grazing-incidence X-ray diffraction

Based on the work from the previous chapter, samples were subjected to ion beam irradiation with fluences of either 10^{15} or 10^{16} Au ions/cm^2. They were analysed by Grazing incidence X-ray diffraction to study the changes of crystallinity and macrostructure. The X-ray patterns for all samples are shown in Figure 6.3. Considering the sample porosity and ion implantation depth which was measured via cross-section SEM and calculated using SRIM 2013, a 2^o incidence angle was selected for the analysis of $SrMoO_4$ and 5^o incidence angle was selected for analysis of all other samples. The

depth corresponding to 2^{o} and 5^{o} incidence angle for each compound is summarized in Table 6-3, as calculated from X-ray mass absorption coefficients [117]. It should be noted that the effect of ion beam irradiation will vary throughout the damage depth and GI-XRD provides an average pattern for the entire region that it probes. Only $CaWO_4$ displayed a broad amorphous hump centered at ~28° (2θ) and this appeared at both fluences. Otherwise, all samples showed decreasing diffraction peak intensity with increasing ion fluence for all reflections except the reflection of the (004) plane (see Figure 6.4) which appeared to increase in intensity with increasing ion fluence. To demonstrate this effect, the intensity ratio of the (004) X-ray reflection and the most intense reflection (112) are listed in Table 6-4. Although, $CaWO_4$ showed a decrease for the ratio suggesting the loss of long range order in (004) plane, all other samples showed an increase and the effect was more pronounced in the samples irradiated at higher fluence. The crystallinity has been calculated using the four most intense X-ray reflections (excluding the (004) plane) of all samples that were irradiated to all ion fluences and divided by the same peak intensity of the un-irradiated sample. The average crystallinity of all compounds irradiated to different fluence and the standard error were plotted in Figure 6.5. GI-XRD analysis was repeated 3 months after the irradiation and this is also plotted. The largest loss of crystallinity for samples irradiated to 10^{16} ions/cm^2 was for $CaWO_4$ (~22% crystalline), while $BaMoO_4$ (~60% crystalline) and the other compounds (~75% crystalline) show much more crystallinity. Approximately 40% of crystallinity was recovered during room temperature aging for 3 months for $CaWO_4$ that had been irradiated to 10^{16} ions/cm^2.

In order to further investigate this unusual observation, lattice parameters and unit cell volume (V) have been plotted in Figure 6.6 (data can be found Table 8-1 and 8-2 of Appendix section), and FWHM (full weight half maximum) for the (112) and (004)

reflection planes were determined and the results are provided in Table 6-5. The unit cell volume of all samples showed expansion after irradiation; however the changes were very small (less than 1%). $CaWO_4$ and $CaMoO_4$ showed a continuously increase of V with the ion fluence, as the atomic number of A-site increases the trend of unit cell volume vs ion fluence changed from linear to quadratic. The error of estimated V was taken from Rietica [71]. On the other hand, for the samples irradiated to 10^{16} ions/cm^2 the greatest broadening of FWHM for (112) and (004) plane reflections were $CaBO_4$, followed by $SrBO_4$ and $BaBO_4$ (B = W and Mo) which showed almost no notable changes for (112) plane. The (004) plane showed much more broadening than (112) plane, which may suggest the (112) plane allowed more facile defect diffusion than in the (004) plane. As the sample (except $CaWO_4$ and $CaMoO_4$) was irradiated to 10^{16} ions/cm^2, the FWHM of both planes showed less broadening, which was similar to the V change. To investigate room temperature recovery, all the samples were analyzed again three months after the initial irradiations and the differences in FWHM, lattice parameter and V for the samples with the highest ion fluence are displayed in Figure 6.7 (data are given in Table 8-1 and 8-2 of the Appendix section) and Table 6-5. $CaWO_4$ showed a small decrease of V (~0.38% for 10^{15} ions/cm^2 and ~0.67% for 10^{16} ions/cm^2) when compared to the data produced immediately after irradiation, while others showed no significant changes to the data collected within a week of the irradiation damage. Figure 6.3(g) shows the GI-XRD pattern for the $CaWO_4$ sample measured 3 months after initial irradiation and importantly no amorphous hump was observed. $CaWO_4$ also showed a large reduction of FWHM for the (112) X-ray reflection (reduction of ~19% and ~43% when compared with the data produced just after irradiation. The (004) X-ray reflection showed a decrease of FWHM (~9% and ~22% when compare with the data produced just after irradiation). $SrMoO_4$ $BaMoO_4$, $SrWO_4$ and $BaWO_4$ showed no clear change in FWHM for both (112) and (004)

planes. Similarly to $CaWO_4$, $CaMoO_4$ showed a reduction of ~34% for the FWHM in (112) plane when compared to the just irradiated sample with a fluence of 10^{16} ions/cm^2.

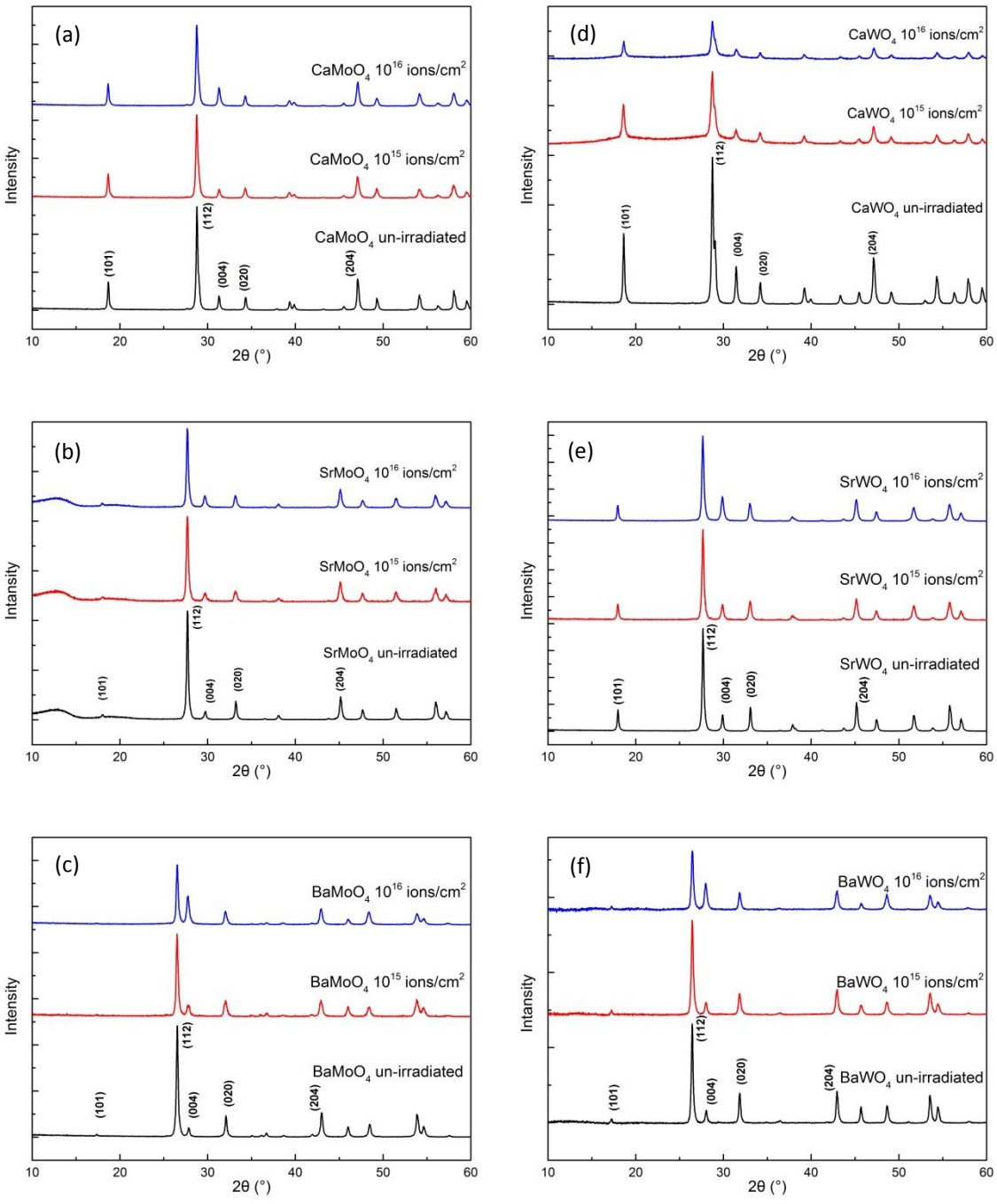

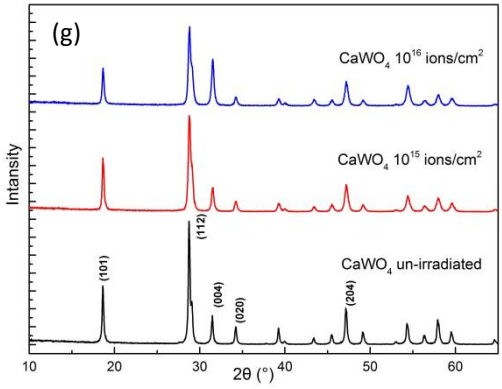

Figure 6.3 The GI-XRD patterns for ABO_4 (a) – (f) $CaMoO_4$, $SrMoO_4$, $BaMoO_4$, $CaWO_4$, $SrWO_4$ and $BaWO_4$ measured within 1 week of irradiation, and (g) $CaWO_4$ same samples measured three months later.

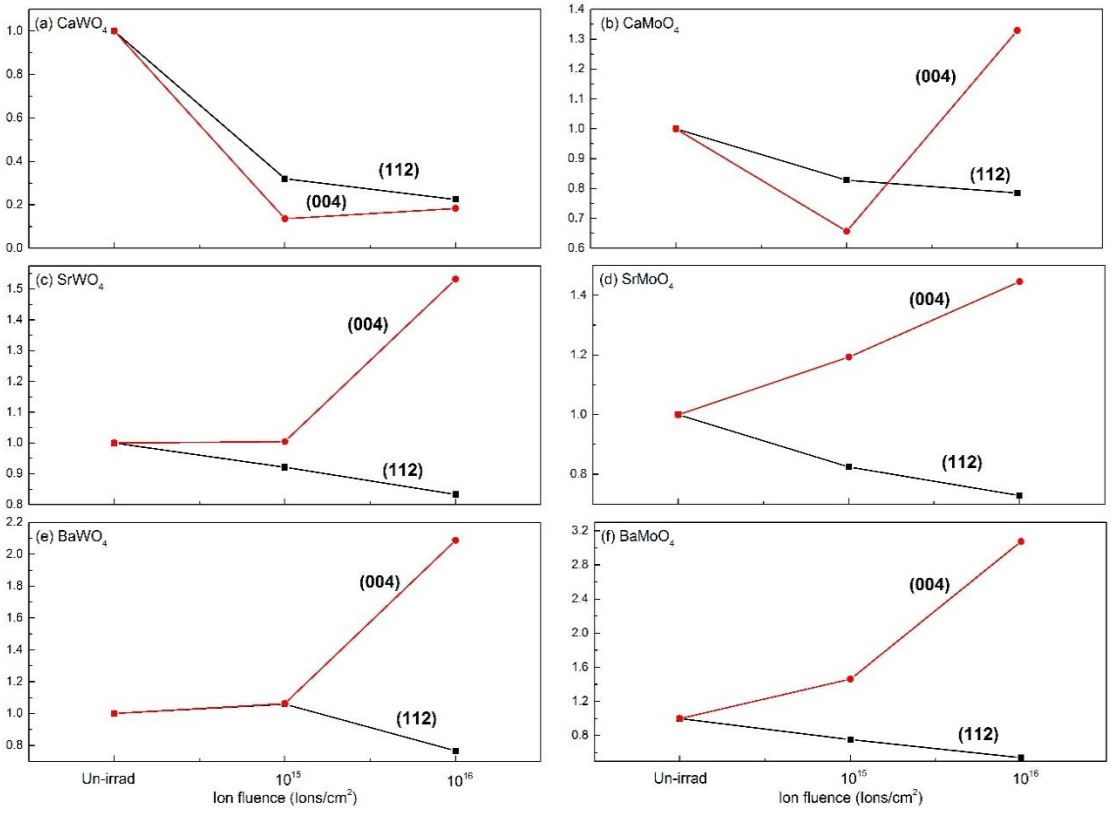

Figure 6.4 The normalized intensity of the (112) and (004) X-ray reflections for all compounds. Measurements were taken within 1 week after irradiation.

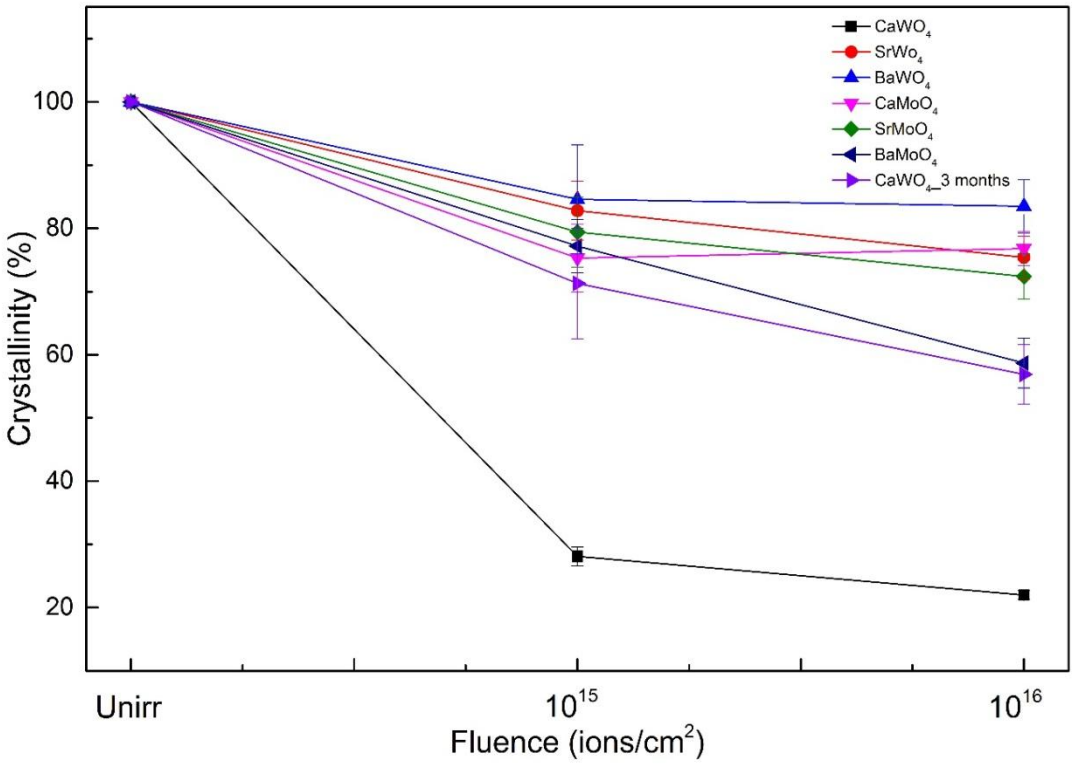

Figure 6.5 The crystallinity of all compounds irradiated to 10^{15} and 10^{16} ions/cm^2 within 1 week.

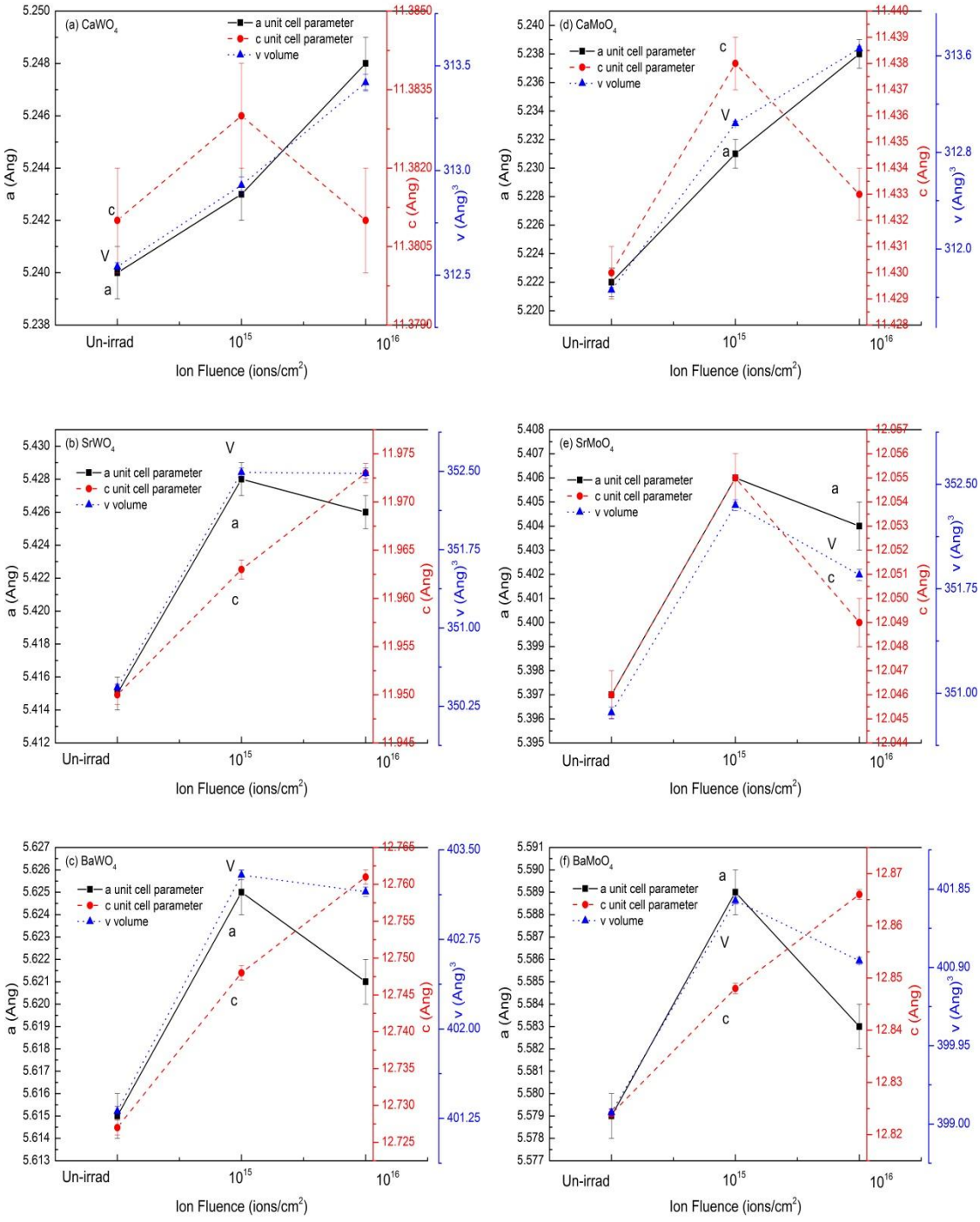

Figure 6.6 Lattice parameters for all ABO_4 compounds. Measurements were undertaken within 1 week following irradiation.

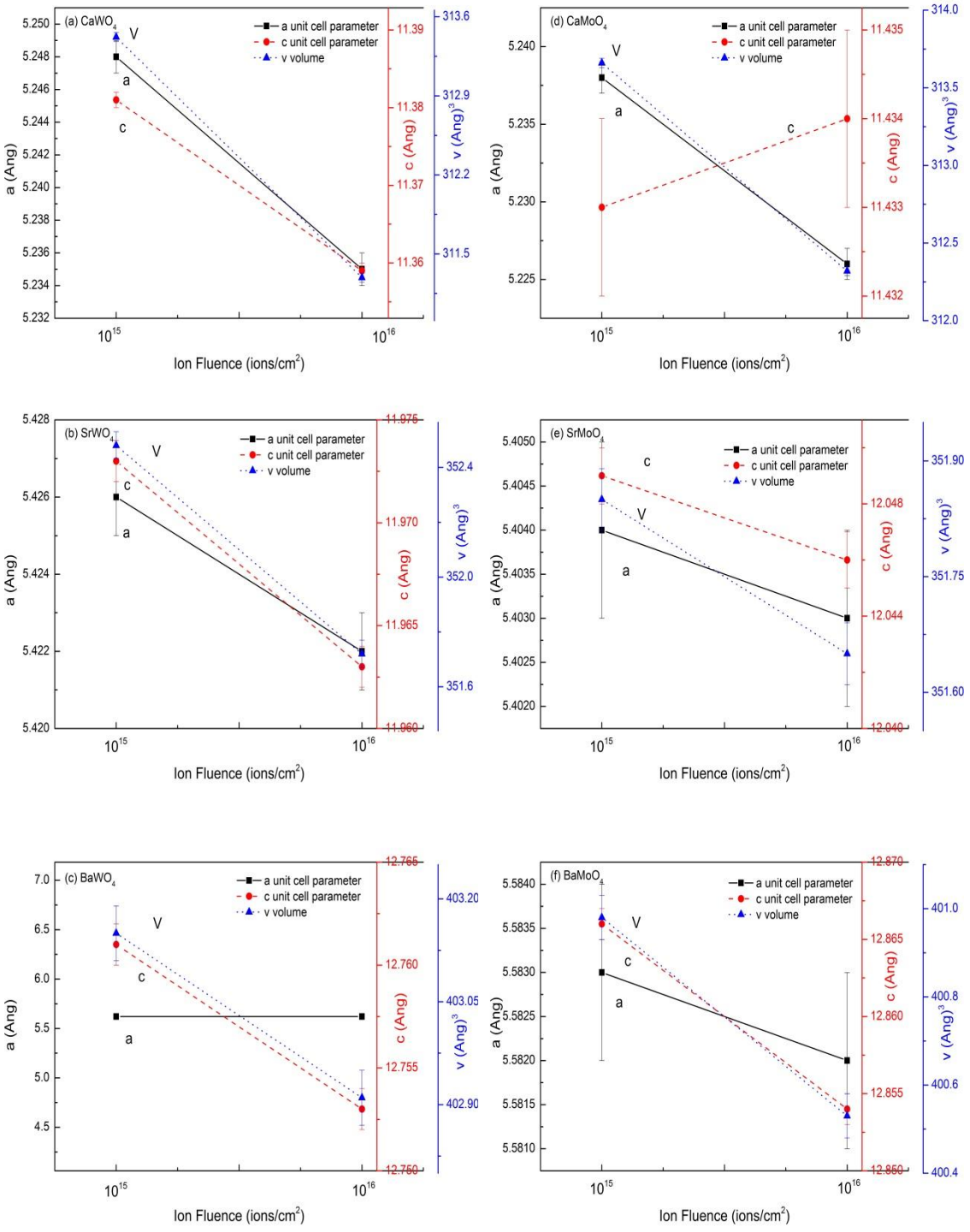

Figure 6.7 The comparison of lattice parameters that were measured in 3 months for all ABO_4 compounds that irradiated at 10^{16} ions/cm^2.

Table 6-3 The X-ray scanning depth calculated using mass absorption coefficient [117] with 2 °and 5 °incidence angle, damage depth observed using SEM, and calculated from SRIM analysis.

Sample	X-ray Depth (μm)		Ion Depth determined by SEM(μm)	Calculated Implantation depth from SRIM [116, 142] (μm)
	2 °	5 °		
$CaWO_4$	0.42	1.07	1.99	1.56
$SrWO_4$	0.42	0.61	1.99	1.65
$BaWO_4$	0.27	0.68	1.92	1.68
$CaMoO_4$	0.71	1.80	1.97	1.8
$SrMoO_4$	0.67	1.69	1.77	1.77
$BaMoO_4$	0.34	0.85	2.17	1.74

Table 6-4 The intensity ratio of the (004) and (112) reflection obtained by GI-XRD. Measurements were performed within 1 week.

Fluences	Intensity Ratio (004)/(112)					
	$CaWO_4$	$CaMoO_4$	$SrWO_4$	$SrMoO_4$	$BaWO_4$	$BaMoO_4$
Un-irradiated	0.25	0.14	0.16	0.08	0.14	0.09
10^{15} ions/cm^2	0.11	0.11	0.18	0.12	0.13	0.17
10^{16} ions/cm^2	0.2	0.23	0.29	0.16	0.45	0.49

Table 6-5 FWHM of diffraction peaks (112) and (004) for each sample. Measurements were undertaken within 1 week following irradiation.

Sample		Peak (112)			Peak (004)		
		X (°)	FWHM (°)		X (°)	FWHM (°)	
			1 week	3 months		1 week	3 months
$CaWO_4$	Un-irradiated	28.727	0.19	0.18	31.431	0.214	0.243
	10^{15} ions/cm^2	28.725	0.335	0.27	31.435	0.33	0.302
	10^{16} ions/cm^2	28.754	0.47	0.27	31.482	0.401	0.314
$CaMoO_4$	Un-irradiated	28.782	0.192	0.184	31.296	0.213	0.2
	10^{15} ions/cm^2	28.759	0.256	0.233	31.301	0.265	0.264
	10^{16} ions/cm^2	28.772	0.31	0.205	31.307	0.314	0.306
$SrWO_4$	Un-irradiated	27.643	0.235	0.23	29.877	0.235	0.265
	10^{15} ions/cm^2	27.624	0.263	0.248	29.853	0.303	0.286
	10^{16} ions/cm^2	27.65	0.257	0.252	29.879	0.331	0.332
$SrMoO_4$	Un-irradiated	27.668	0.211	0.206	29.688	0.217	0.27
	10^{15} ions/cm^2	27.647	0.24	0.22	29.668	0.298	0.285
	10^{16} ions/cm^2	27.678	0.225	0.22	29.692	0.315	0.298
$BaWO_4$	Un-irradiated	26.445	0.25	0.255	28.047	0.225	0.225
	10^{15} ions/cm^2	26.449	0.239	0.26	28.003	0.291	0.255
	10^{16} ions/cm^2	26.454	0.25	0.261	27.972	0.337	0.338
$BaMoO_4$	Un-irradiated	26.506	0.238	0.241	27.803	0.293	0.28
	10^{15} ions/cm^2	26.491	0.254	0.243	27.752	0.339	0.308
	10^{16} ions/cm^2	26.53	0.243	0.257	27.75	0.344	0.321

Cross-section Raman

Micro-Raman spectroscopy has been used to study the shorter correlation length scale of the ABO_4 samples following irradiation. Raman analysis was measured on the cross-sectioned pellets at various depths through the damaged layer, to study the effect of radiation damage on all samples. However, as the beam size was about 1.5 μm in diameter and the damaged layer was around 2 μm thick, it was possible that some un-irradiated material was also examined by the scattered laser beam when analysing the damaged materials. The measurements were carried out around 2 weeks after GI-XRD measurements. In the selected compositions there was one crystal structure, and two

different BO_4^{2-} ion groups, so each of the compositions will first be described based on their Raman vibration modes. As shown in Figure 6.8, the fingerprint region for the compositions was between 150 and 1000 cm^{-1} phonon frequency. The Raman spectrum for a typical ABO_4-type scheelite structure of BO_4 tetrahedra with strong covalent B-O bonding is well known [139]. There are five internal vibration bands with the BO_4 ionic group observed in Figure 6.8, which were V_1 (symmetrical stretching mode), V_2 (symmetrical bending mode), V_3 (asymmetrical stretching) and V_4 (asymmetrical bending mode) with one free rotation mode $V_{f.r.}$ which was an external vibration mode. As shown in Figure 6.9 the vibration frequency for AWO_4 and $AMoO_4$ compounds increased with atomic number, as expected due to the decrease of bond length of B-O with increase in A-site atom size. The V_1 mode of AWO_4 showed higher phonon frequency than $AMoO_4$ compounds; suggesting that W-O bonds have higher energy in the bonding direction than Mo-O bonds.

Micro-Raman spectroscopy has been used to study the effect of self-radiation, swift ion and ion irradiation on many ceramics. Often, materials undergoing radiation damage show loss of short range order (broadening of Raman modes), decrease of Raman intensity and sometimes decrease in phonon frequency. All samples showed a decrease of Raman mode intensity and band broadening with increasing fluence. $SrWO_4$ and $SrMoO_4$ had the least reduction of intensity, while other samples showed more significant reduction. OrginPro 8.6 was used to calculate the V_1 and V_2 mode band width (FWHM) for each sample and the band shape was fitted using Gaussian function (see Table 6). The errors of band width determined from the fitted peak were ± 0.3 cm^{-1} for the width <10 cm^{-1} and ± 0.7 cm^{-1} for the width between 18 and 10 cm^{-1}. The results showed an overall broadening and no clear band shifting when materials were irradiated. Tungstates showed less V_1 mode broadening with increasing the ion fluence than molybdates, where the

overall V_1 broadenings of $CaWO_4$, $SrWO_4$, and $BaWO_4$ were 1 cm^{-1}, 1 cm^{-1} and 0.3 cm^{-1}, respectively, while they were 1.4 cm^{-1}, 1.8 cm^{-1}, and 0.7 cm^{-1} for $CaMoO_4$, $SrMoO_4$, and $BaMoO_4$, respectively. Tungstates showed more broadening of the V_2 band than powellites where the overall broadening of AWO_4 was 4.5 cm^{-1}, 3.1 cm^{-1}, and 1.1 cm^{-1}, for $CaWO_4$, $SrWO_4$, and $BaWO_4$, respectively, and 3.4 cm^{-1}, 0.9 cm^{-1}, and 1.8 cm^{-1} overall broadening for $AMoO_4$ with A = Ca, Sr, and Ba, respectively. Further band broadenings at 10^{16} ions/cm^2 were unable to identify due to low band single, except for $SrWO_4$ and $SrMoO_4$ these samples have relative strong band intensity and did not show further broadening.

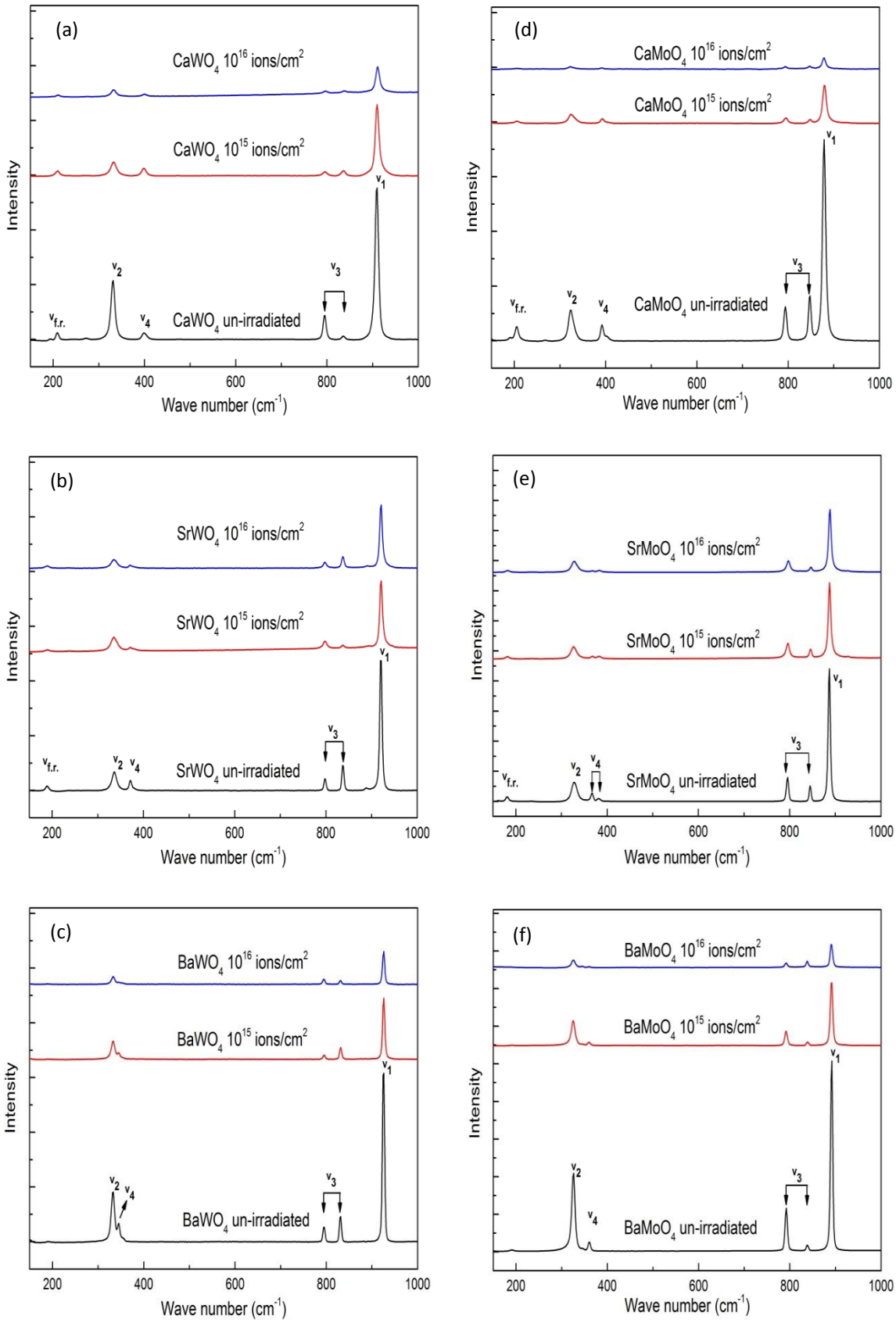

Figure 6.8 Cross-section Raman for ABO_4 compounds. (a) – (c) $CaWO_4$, $SrWO_4$ and $BaWO_4$, (d) – (f) $CaMoO_4$, $SrMoO_4$ and $BaMoO_4$ irradiated at 10^{16} and 10^{15} ions/cm^2.

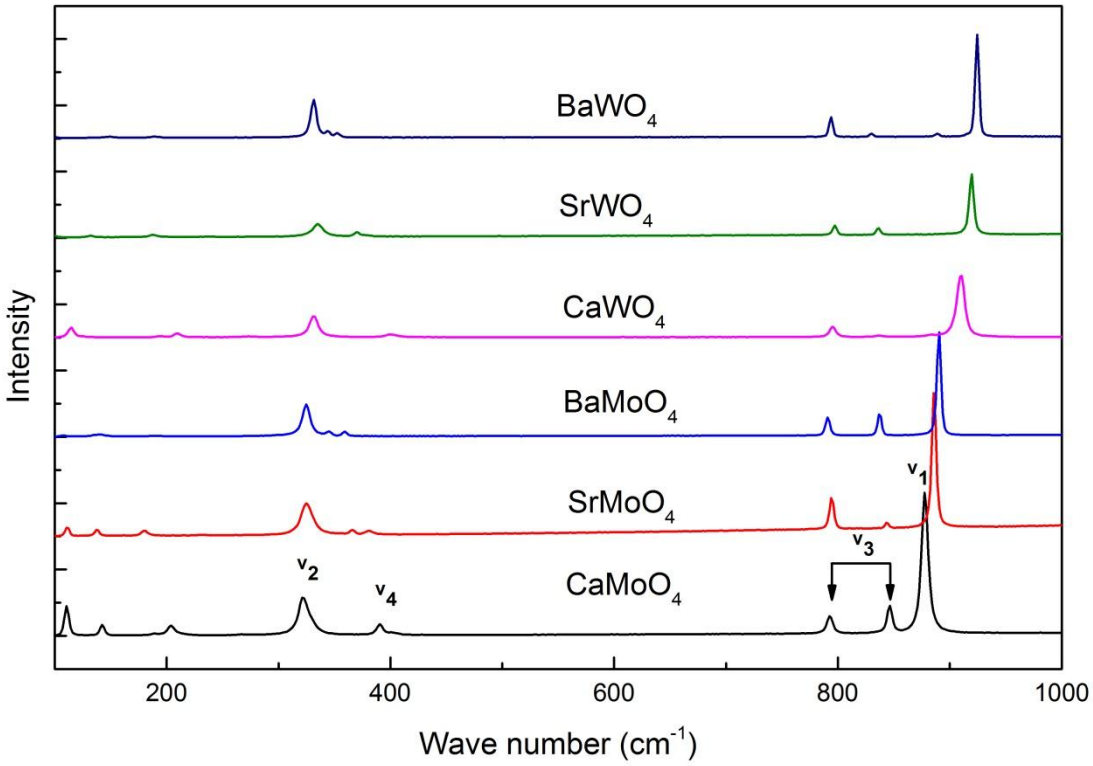

Figure 6.9 Raman spectra for the un-irradiated ABO_4 compounds.

Table 6-6 Phonon frequency and width of V_1-symmetric stretching mode and V_2-symmetric bending mode for each sample with increasing fluence of irradiation.

Sample		V_1	FWHM	V_2	FWHM
$CaWO_4$	Un-irradiated	910.2	9.4	330.8	10.6
	10^{15} ions/cm^2	909.9	10.1	332.3	15.1
	10^{16} ions/cm^2	910.2	10.4	333.7	14.7
$SrWO_4$	Un-irradiated	920.3	6.1	336.0	12.2
	10^{15} ions/cm^2	920.7	7.2	335.6	15.9
	10^{16} ions/cm^2	920.5	7.0	335.7	14.7
$BaWO_4$	Un-irradiated	925.2	5.4	332.3	7.9
	10^{15} ions/cm^2	925.7	5.7	332.8	9.3
	10^{16} ions/cm^2	925.4	5.7	332.9	8.8
$CaMoO_4$	Un-irradiated	878.7	8.3	324.3	14.4
	10^{15} ions/cm^2	879.6	9.6	325.7	17.9
	10^{16} ions/cm^2	878.5	9.7	324.4	17.7
$SrMoO_4$	Un-irradiated	886.6	6.3	328.1	14.5
	10^{15} ions/cm^2	887.3	8.1	327.0	15.1
	10^{16} ions/cm^2	888.1	8.1	328.2	15.5
$BaMoO_4$	Un-irradiated	891.4	5.7	325.5	8.7
	10^{15} ions/cm^2	891.2	6.4	325.0	10.4
	10^{16} ions/cm^2	891.0	6.3	325.6	10.7

6.5 Discussion

Irradiation by Au-ions was intended to simulate the recoil particle during α-decay process. The energy deposited into the material following Au-ion irradiation includes electronic interactions and nuclear displacements. Some of the total energy from the former is released in the form of heat, and the latter remainder in the displacement of the atoms which are knocked from their crystal sites by the Au-ions. Around 70% of total energy deposited by the Au ion is released through electronic interactions and about 30% through nuclear displacements, according to the SRIM data shown in Table 6-1. The AWO_4 samples exhibited a slightly lower electronic percentage than $AMoO_4$ samples (~13% on average). The ion range in all samples was found to be around 2 μm. In general, results

of GI-XRD and cross-section Raman of all samples suggested loss of long and short range order; moreover, an amorphous hump was noted in the XRD pattern for irradiated $CaWO_4$. It was remarkable that with such high dose and damage levels most of these samples still remained at least 60% crystalline. In terms of GI-XRD, all samples displayed an increase of peak width under irradiation that did not increase further at higher fluence, except for $CaWO_4$ and $CaMoO_4$. However, both the V_1 and V_2 vibration band widths in the Raman spectra were unable to be measured due to the low band intensity after the 10^{16} ions/cm^2 dose. The samples were first analysed by GI-XRD followed by Raman analysis about 2 weeks later, and a second GI-XRD analysis was undertaken three months after irradiation. The results of the second GI-XRD analysis on $CaWO_4$ which irradiated to the highest ion fluence (10^{16} ions/cm^2) showed 0.68% reduction of V comparing to the result obtained from the first analysis. The GI-XRD peak widths of (112) and (004) plane showed less broadening after 3 months for both ion fluences. Lastly, an interesting observation was the change in intensity ratio of (004) / (112) reflections where it increased an order of magnitude following Au irradiation with 10^{16} ions/cm^2 (within 1 week after irradiation). The peak widths of the (004) reflections for $SrWO_4$, $SrMoO_4$, $BaWO_4$, and $BaMoO_4$ also have displayed more broadening when compared to the (112) reflections.

The effect of varying A- and B-site atom in the ABO_4 scheelite type compounds on radiation resistance were investigated using GI-XRD and Micro-Raman spectroscopy. $CaWO_4$ displayed a broad hump in the GI-XRD measurement indicating amorphization with approximately 22% crystallinity remaining after 10^{16} ions/cm^2 irradiation. $CaWO_4$ and $CaMoO_4$ showed small overall increases in unit cell volume after 10^{16} ions/cm^2 irradiation which continued to expand with ion fluence. All samples showed significant peak broadening in (112) and (004) reflections. These observations could suggest that the crystal structure of $CaWO_4$ and $CaMoO_4$ were less stable than other selected compounds.

The calculated crystallinity data from GI-XRD results suggests $CaMoO_4$ had better radiation tolerance than $CaWO_4$ under irradiation especially at high ion fluence. Radiation resistance appears to follow a simple direction whereby the higher the atomic number on the A-site the more radiation tolerance in the system. However, $BaMoO_4$ displayed ~60% crystallinity at the highest ion fluence while other molybdate samples showed more than 70%. This may be due to the chemical effect of A-site atom or experimental error. Meldrum et al [69] have found a chemical effect can counterbalance the structure effect between monazite ($GdPO_4$) and zircon ($ScPO_4$) where the critical amorphization temperature of $GdPO_4$ and $ScPO_4$ were similar. On the other hand, there was no clear "amorphous hump" in the Raman spectra of the studied samples, and no shifts in the vibration bands were observed. In terms of band broadening V_2 is more sensitive to point defect accumulation than V_1 in tungstates that I studied, however the molybdates except $SrMoO_4$ did not show as significant band differences between V_1 and V_2 modes as the tungstates. While, AWO_4-scheelite samples have more broadening of V_1 mode, and $AMoO_4$-powellite samples showed greater broadening in V_2 mode. Based on the Raman results on the band broadening, the W-O and Mo-O bonding may show anisotropic behaviour following radiation damage, since the bonding was stronger in the bond direction than other directions.

Compared to the previous study in chapter 5 on other ABO_4 compounds, the scheelite structure showed extreme radiation tolerance where the highest dose in this chapter is ten times higher than that of the previous chapter, and the remaining crystalline percentage is higher after the irradiation. Interestingly, in the previous report on 5 MeV Au-ion irradiation different structure ABO_4 families, CaWO4 was not found to go amorphous and the SRIM calculation on nuclear stopping power (dE/dx) was 312.94 eV/Å, whereas in this study 12 MeV Au-ions was used, dE/dx equal 201.96 eV/Å. Grover et al [143]

have shown large grains provide better radiation stability. Indeed, samples were prepared in different ways and as a result the grain size of each sample was different, with Sol-Gel methods grains will tend to be smaller, although this depends on the heat treatment.

The samples displayed an increase in the X-ray peak intensity ratio of (004) / (112) with samples irradiated to 10^{16} ions/cm^2; this may suggest that the local amorphization and re-crystallization was easier in (004) plane than (112) plane, due to the amorphization mechanics discussed in chapter 2. However the orientation change was often found in doped scheelite materials (for example in ref [144]). The XRD peak width of the (004) reflection for all samples show greater broadening than the (112) and other XRD reflections and the anisotropic behaviour after irradiation which also observed in Raman band broadening. These may suggest that the defects easier accumulated in (004) plane rather than any other planes in selected ABO_4-scheelite and powellite type compounds. Zhu et al. [145] have illustrated the degree of radiation damage is affected by ion beam direction with respect to different crystal orientations. For example ref. [145] they demonstrate that the beam directed along (100) will cause more severe structural damage than that in the (001) direction. However, another possible explanation for XRD peak width broadening could relate to the "thermal spike" model [146]. The crystal undergoing high energy irradiation could result in some degree of structural recovery [147]. However, these crystal recovery effects also highly depend on the ENSP (electronic-to-nuclear stopping power) ratio and the dose rate. The current data are not sufficient to explain why and what causes this phenomenon. Several explanations are available to explain the phenomenon and further work is required to assess each. For example, one such experiment could be to assess the degree of radiation damage by ion beam direction with respect to different crystal orientations.

The disappearance of the amorphous hump in the XRD pattern measured three months after the ion irradiation could suggest a low recovery temperature for $CaWO_4$, and the pervious study also found $CaWO_4$ could potentially have a relative low recovery temperature in the annealing experiments. Again, this could be a result of unstable defects produced during ion irradiation, which self-recover by defect diffusion [148]. This will mainly relate to the activation energy for vacancy diffusion, which is very hard to observe experimentally.

6.6 Summary

In this study, a set of ABO_4 scheelite and powellite type compounds were irradiated using 12 MeV Au-ions with two doses 10^{15} and 10^{16} ions/cm^2. GI-XRD and Raman spectroscopy were carried out for structural analysis. The results suggest that this series of compounds are extremely radiation tolerant. Their irradiation stability was increased as the A-site atom increase in atomic number, and powellite compounds generally have better irradiation stability than scheelite compounds. The possible reasons for decreases in XRD peak broadening of higher fluence for the (112) plane were discussed. Further work is needed to study the anisotropic behaviour following ion irradiation.

7. Conclusions and Future Work

7.1 Conclusions

In this study, the two possible methods that can potentially reduce the risk of growing nuclear wastes have been investigated. One traditional method is to process them into dense refractory solids (waste forms) which can survive a long period of time underground. In this regard, although lots research on the radiation tolerance of ABO_4 monazite and zircon structural, little work on scheelite and powellite structures. The second method investigated was by using Inert Matrix Fuels in the burn circle. The IMF materials offer the advantage of burning surplus plutonium and other minor actinides produced from the fuel cycle in current light water reactors with minimal production of further actinides. In this work, materials for both methods have been designed and studied with the ultimate future goal of providing options to manage the global nuclear waste stockpiles.

The MgO and pyrochlore $Nd_2Zr_2O_7$ composites with a content of MgO 50–70 vol.% were produced via a chemical route using an aqueous solution in a one-pot synthesis procedure. The grain size of these composites is in the submicron size range (200–500 nm) for both phases and relatively high density (> 90% of theoretical density). Samples synthesized by aqueous solution processing have better homogeneity than those synthesized by mixed oxide and sol-gel routes. Importantly, the results show that although the aqueous solution method results in a reduced particle size it does not detrimentally affect the thermal conductivity at application relevant temperatures above 300 ℃, due to enhanced homogeneity and connectivity. This novel aqueous synthetic method provides a simple pathway for the candidate IMF MgO–lanthanide zirconate pyrochlore production without

need for organic solvents and mechanical milling, making it very attractive for a potential scale-up production.

The study on 5 MeV Au ion irradiation effect on various kinds of compositions and structures ABO_4 compounds were found $CaWO_4$ and YVO_4 with tetragonal structure shown promising radiation tolerant property, where undergo 10^{15} ions/cm^2 dose with about ~3 dpa damage level did not show complete amorphization. $LaVO_4$, $LaNbO_4$, $YNbO_4$ with monoclinic structure showed long- and short-range order loss upon irradiation. Only $YNbO_4$ showed phase transition during Au ion irradiation. Chemical effects were more significant in annealing experiment than the structure difference. Since there are very little studies on the radiation tolerance of ABO_4 scheelite and powellite structural and the promising radiation tolerant result showed in $CaWO_4$ (scheelite). It is worth to carrying out further radiation behaviour investigation to seek out more about these structural under higher irradiation fluence.

Further, a set of ABO_4 scheelite and powellite type compounds were irradiated using 12 MeV Au-ion with higher doses than the previous study (chapter 5), GI-XRD and Raman spectroscopy were carried out for structural analysis. The results suggest that this series of compounds are extremely radiation tolerance. During and after the irradiation there are two interesting observations were found, the $CaWO_4$ was able to re-crystalline itself at room temperature 3 months after irradiation, and the (004)/(112) intensity ratio of all compounds undergo irradiation were increased.

In conclusion, a novel synthetic method was established which provides simply pathway and much more homogeneity and connectivity of the MgO-$Nd_2Zr_2O_7$ composited. The studies on ABO_4 compounds showed scheelite and powellite compounds have extremely good radiation tolerance which remains about 60% crystalline even after 10^{16} ions/cm^2

dose. Further work is needed to gain a fully understanding of the structural evaluation during and after irradiation.

7.2 Future Work

In this study, there was one interesting results worth to carry on further investigation. The radiation tolerance of scheelite structure compounds, such as $CaWO_4$, was very promising already, but also the re-crystalline itself at room temperature in three months. The mechanism behands this recovery was not clear at the moment, but the possible explanation is due to the defects that produced by ion irradiation were highly unstable. The crystal will self-recover by defect diffusion, and this process is mainly relating to the activation energy for vacancy diffusion, which is very hard to observe experimentally. In future, in situ transmission electron microscopy would experimentally test and verify the phenomenon of this annealing temperature also observe displacement defects, and together with the use of computer modelling theoretically to calculate the activation energy of defect migration. Preferred orientation studies also needed to explain the relative peak interstices, and increase the XRD measuring range from 60 ° to 140° 2θ to have a more accurate lattice parameter and unit cell volume calculation.

8. Appendix

Table 1-1 Lattice parameters for all ABO_4 compounds. Measurements were undertaken within 1 week following irradiation.

Sample		Lattice parameters			Volume ($Å^3$)
		a (Å)	b (Å)	c (Å)	
$CaWO_4$	Un-irradiated	5.240(1)	5.238(1)	11.381(1)	312.54(2)
	10^{15} ions/cm^2	5.243(1)	5.243(1)	11.383(1)	312.93(4)
	10^{16} ions/cm^2	5.248(1)	5.248(1)	11.381(1)	313.42(4)
$CaMoO_4$	Un-irradiated	5.222(1)	5.222(1)	11.430(1)	311.66(2)
	10^{15} ions/cm^2	5.231(1)	5.231(1)	11.438(1)	313.04(2)
	10^{16} ions/cm^2	5.238(1)	5.238(1)	11.433(1)	313.66(2)
$SrWO_4$	Un-irradiated	5.415(1)	5.415(1)	11.950(1)	350.43(3)
	10^{15} ions/cm^2	5.428(1)	5.428(1)	11.963(1)	352.49(4)
	10^{16} ions/cm^2	5.426(1)	5.426(1)	11.973(1)	352.48(5)
$SrMoO_4$	Un-irradiated	5.397(1)	5.397(1)	12.046(1)	350.86(4)
	10^{15} ions/cm^2	5.406(1)	5.406(1)	12.055(1)	352.35(4)
	10^{16} ions/cm^2	5.404(1)	5.404(1)	12.049(1)	351.85(4)
$BaWO_4$	Un-irradiated	5.615(3)	5.615(1)	12.727(1)	401.31(4)
	10^{15} ions/cm^2	5.625(3)	5.625(1)	12.748(1)	403.29(4)
	10^{16} ions/cm^2	5.621(3)	5.621(1)	12.761(1)	403.15(4)
$BaMoO_4$	Un-irradiated	5.579(1)	5.579(1)	12.824(1)	399.14(4)
	10^{15} ions/cm^2	5.589(1)	5.589(1)	12.848(2)	401.71(4)
	10^{16} ions/cm^2	5.583(1)	5.583(1)	12.866(1)	400.98(4)

Table 2-2 Lattice parameters for all ABO_4 compounds. Measurements were undertaken within three months after irradiation.

Sample		Lattice parameters			Volume ($Å^3$)
		a (Å)	b (Å)	c (Å)	
$CaWO_4$	Un-irradiated	5.238(1)	5.238(1)	11.372(1)	312.02(2)
	10^{15} ions/cm^2	5.238(1)	5.239(1)	11.359(1)	311.74(3)
	10^{16} ions/cm^2	5.235(1)	5.235(1)	11.359(1)	311.29(3)
$CaMoO_4$	Un-irradiated	5.223(1)	5.223(1)	11.431(1)	311.77(2)
	10^{15} ions/cm^2	5.229(1)	5.229(1)	11.434(1)	312.65(3)
	10^{16} ions/cm^2	5.226(1)	5.227(1)	11.434(1)	312.32(3)
$SrWO_4$	Un-irradiated	5.414(1)	5.414(1)	11.947(1)	350.18(3)
	10^{15} ions/cm^2	5.425(1)	5.425(1)	11.973(1)	352.35(3)
	10^{16} ions/cm^2	5.422(1)	5.422(1)	11.963(1)	351.72(3)
$SrMoO_4$	Un-irradiated	5.391(1)	5.391(1)	12.039(1)	349.89(3)
	10^{15} ions/cm^2	5.404(1)	5.404(1)	12.046(1)	351.72(3)
	10^{16} ions/cm^2	5.403(1)	5.400(1)	12.046(1)	351.65(3)
$BaWO_4$	Un-irradiated	5.617(1)	5.617(1)	12.734(1)	401.73(4)
	10^{15} ions/cm^2	5.619(1)	5.619(1)	12.715(1)	401.54(5)
	10^{16} ions/cm^2	5.621(1)	5.621(1)	12.753(1)	402.91(4)
$BaMoO_4$	Un-irradiated	5.579(1)	5.579(1)	12.822(1)	399.12(4)
	10^{15} ions/cm^2	5.583(1)	5.583(1)	12.850(1)	401.01(5)
	10^{16} ions/cm^2	5.582(1)	5.582(1)	12.854(1)	400.53(5)

9. Reference

1. Mian, Z. and A. Glaser. *Global Fissile Material Report 2015. Nuclear weapons and fissile material stockpiles and production*. in *presentation at NPT Review Conference, May*. 2015.
2. A.T. Nelson, M.M.G., J.C. Nino, K.J. McClellan, *Effect of composition on thermal conductivity of MgO-Nd2Zr2O7 composites for IMF.* Journal of Nuclear Materials, 2014. **444**: p. 385-392.
3. S.J. Yates, K.J.M., J.C. Nino, *The effect of processing on the thermal diffusivity of MgO–$Nd_2Zr_2O_7$ composites for IMF.* Journal of Nuclear Materials, 2009. **393**: p. 203-211.
4. Hellwig, C. and U. Kasemeyer, *Inert matrix fuel performance during the first two irradiation cycles in a test reactor: comparison with modelling results.* Journal of Nuclear Materials, 2003. **319**(0): p. 87-94.
5. Hellwig, C., et al., *Interpretation of experimental results from moderate-power in-pile testing of a Pu–Er–Zr–oxide inert matrix fuel.* Annals of Nuclear Energy, 2003. **30**(3): p. 287-299.
6. Nawada, F.S.a.H.P., *Viability of inert matrix fuel in reducing plutonium amounts in reactors.* International Atomic Energy Agency, 2006. **IAEA-TECDOC-1516**.
7. Shukla, P., et al., *Thermal transport properties of MgO and $Nd_2Zr_2O_7$ pyrochlore by molecular dynamics simulation.* Journal of Nuclear Materials, 2008. **380**(1–3): p. 1-7.
8. S. Lutique , R.J.M.K., V.V. Rondinella, J. Somers, T. Wiss, *The thermal conductivity of $Nd_2Zr_2O_7$ pyrochlore and the thermal behaviour of pyrochlore-based inert matrix fuel.* Journal of Alloys and Compounds, 2003. **325**: p. 1-5.
9. Toberer, E.S., A. Zevalkink, and G.J. Snyder, *Phonon engineering through crystal chemistry.* Journal of Materials Chemistry, 2011. **21**(40): p. 15843-15852.
10. Goldsmid, H.J. and A.W. Penn, *Boundary scattering of phonons in solid solutions.* Physics Letters A, 1968. **27**(8): p. 523-524.
11. Parrott, J.E., *The thermal conductivity of sintered semiconductor alloys.* J. Phys. C: Solid State Physics, 1969. **2**: p. 147-151.
12. Chung, J.D., A.J.H. McGaughey, and M. Kaviany, *Role of Phonon Dispersion in Lattice Thermal Conductivity Modeling.* Journal of Heat Transfer, 2004. **126**(3): p. 376-380.
13. Klemens, P.G., *The Scattering of Low-Frequency Lattice Waves by Static Imperfections.* Proceedings of the Physical Society. Section A, 1955. **68**(12): p. 1113.
14. Kim, W. and A. Majumdar, *Phonon scattering cross section of polydispersed spherical nanoparticles.* Journal of Applied Physics, 2006. **99**(8): p. -.
15. Pöml, P., et al., *3.09 - Inert Matrix Fuel*, in *Comprehensive Nuclear Materials*, R.J.M. Konings, Editor. 2012, Elsevier: Oxford. p. 237-256.
16. Miller, J.V., *Estimating thermal conductivity of cermet fuel materials for nuclear reactor application.* NASA Lewis Research Center, Apr 01, 1967. **NASA-TN-D-3898**.
17. Russell, K.C., *Phase stability under irradiation.* Progress in Materials Science, 1984. **28**(3–4): p. 229-434.
18. Norgett, M.J., M.T. Robinson, and I.M. Torrens, *A proposed method of calculating displacement dose rates.* Nuclear Engineering and Design, 1975. **33**(1): p. 50-54.
19. Ianniello, L.C., et al., *Radiation-induced voids in metals; proceedings*. AEC Symposium series,26. 1972, [Washington]: U.S. Atomic Energy Commission, Office of Information Services; [available from National Technical Information Service, Springfield, Va.]. xii, 884 p.
20. Zinkle, S., *1.03 - Radiation-Induced Effects on Microstructure*, in *Comprehensive Nuclear Materials*. 2012, Elsevier: Oxford. p. 65-98.

21. Hobbs, L.W., *Topology and geometry in the irradiation-induced amorphization of insulators.* Nuclear Instruments and Methods in Physics Research Section B: Beam Interactions with Materials and Atoms, 1994. **91**(1–4): p. 30-42.
22. Meldrum, A., et al., *Radiation damage in zircon and monazite.* Geochimica et Cosmochimica Acta, 1998. **62**(14): p. 2509-2520.
23. S.J. Zinkle, L.L.S., W. S. Eatherly, J.W. Jones and D.K. Hensley, *Effect of Low Temperature ion Irradiation on the Microstructure of Nitride Ceramics.* MRS Proceedings, 1998. **540**: p. 305.
24. Weber, W.J., *Models and mechanisms of irradiation-induced amorphization in ceramics.* Nuclear Instruments and Methods in Physics Research Section B: Beam Interactions with Materials and Atoms, 2000. **166–167**: p. 98-106.
25. Motta, A.T. and D.R. Olander, *Theory of electron-irradiation-induced amorphization.* Acta Metallurgica et Materialia, 1990. **38**(11): p. 2175-2185.
26. Zhu, Y., et al., *Structures and effects of radiation damage in cuprate superconductors irradiated with several-hundred-MeV heavy ions.* Physical Review B, 1993. **48**(9): p. 6436.
27. Zinkle, S.J.F., S. A., *Atomic Plasma Mater. Interact. Data Fusion (supplement to Nucl. Fusion)*. Vol. 5. 1994. 174-181.
28. Snead, L.L., S.J. Zinkle, and D.P. White, *Thermal conductivity degradation of ceramic materials due to low temperature, low dose neutron irradiation.* Journal of Nuclear Materials, 2005. **340**(2–3): p. 187-202.
29. Mansur, L.K., *Void swelling in metals and alloys under irradiation: An assessment of the theory.* American Nuclear Society, 1978. **40**(1): p. 5-34.
30. Garner, F.A., *Impact of the injected interstitial on the correlation of charged particle and neutron-induced radiation damage.* Journal of Nuclear Materials, 1983. **117**(0): p. 177-197.
31. Hickman, B.S., *Studies in Radiation Effects,*. Physcial and chemical ed. S. A. Vol. 1. 1966: Dienes, G. J., Ed. Gordon and Breach: New York.
32. Snead, L.L. and S.J. Zinkle, *Use of beryllium and beryllium oxide in space reactors.* AIP Conference Proceedings, 2005. **746**(1): p. 768-775.
33. Clinard Jr, F.W., G.F. Hurley, and L.W. Hobbs, *Neutron irradiation damage in MgO, Al_2O_3 and $MgAl_2O_4$ ceramics.* Journal of Nuclear Materials, 1982. **108–109**(0): p. 655-670.
34. Seitz, F. and J. Koehler, *Displacement of atoms during irradiation.* Solid State Physics-Advances In Research And Applications, 1956. **2**: p. 305-448.
35. Chadderton, L.T. and I.M. Torrens, *Fission Damage in Crystals.* 1969.
36. Fernández, A., R.J.M. Konings, and J. Somers, *Design and fabrication of specific ceramic–metallic fuels and targets.* Journal of Nuclear Materials, 2003. **319**(0): p. 44-50.
37. Streit, M., et al., *Zirconium nitride as inert matrix for fast systems.* Journal of Nuclear Materials, 2003. **319**(0): p. 51-58.
38. Yasuda, K., et al., *Radiation-induced defect clusters in fully stabilized zirconia irradiated with ions and/or electrons.* Journal of Nuclear Materials, 2003. **319**(0): p. 74-80.
39. Hojo, T., et al., *Irradiation effects on yttria-stabilized zirconia irradiated with neon ions.* Journal of Nuclear Materials, 2003. **319**(0): p. 81-86.
40. Sattonnay, G., et al., *Structural stability of $Nd_2Zr_2O_7$ pyrochlore ion-irradiated in a broad energy range.* Acta Materialia, 2013. **61**(17): p. 6492-6505.
41. Wilks, R.S., *Neutron-induced damage in BeO, Al_2O_3 and MgO — a review.* Journal of Nuclear Materials, 1968. **26**(2): p. 137-173.
42. Noirot, J., et al., *Post-irradiation examinations of THERMHET composite fuels for transmutation.* Journal of Nuclear Materials, 2003. **320**(1–2): p. 117-125.
43. Neeft, E.A.C., et al., *The EFTTRA-T3 irradiation experiment on inert matrix fuels.* Journal of Nuclear Materials, 2003. **320**(1–2): p. 106-116.

44. Thurber, W.C., st al., *Irradiation testing of fuel for core B of the Enrico Fermi Fast Breeder Reactor*. 1964, [Oak Ridge, Tenn.]: Oak Ridge National Laboratory.
45. Baldi, S., et al., *Preliminary Evaluation of a BWR with CERMET Fuel Core Loading*, in *Advanced reactors with innovative fuels*. 1999: Switzerland p. 6 pages
46. Lian, J., et al., *Heavy Ion Irradiation of Zirconate Pyrochlores.* MRS Online Proceedings Library, 2002. **713**: p. null-null.
47. Ewing, R.C., J. Lian, and L.M. Wang, *Ion Beam-Induced Amorphization of the Pyrochlore Structure-Type: A Review.* MRS Online Proceedings Library, 2003. **792**: p. null-null.
48. Lutique, S., et al., *Zirconate pyrochlore as a transmutation target: thermal behaviour and radiation resistance against fission fragment impact.* Journal of Nuclear Materials, 2003. **319**(0): p. 59-64.
49. Sickafus, K.E., et al., *Radiation Tolerance of Complex Oxides.* Science, 2000. **289**(5480): p. 748-751.
50. Lian, J., et al., *Radiation-induced amorphization of rare-earth titanate pyrochlores.* Physical Review B, 2003. **68**(13): p. 134107.
51. Minervini, L., et al., *The oxygen positional parameter in pyrochlores and its dependence on disorder.* Philosophical Magazine A, 2002. **82**(1): p. 123-135.
52. Ball, C.J., et al., *Titanate ceramics for the stabilization of partially reprocessed nuclear fuel elements.* Journal of the American Ceramic Society, 1989. **72**(3): p. 404-414.
53. Vance, E.R., *Synroc: A suitable waste form for actinides.* MRS Bulletin, 1994. **19**(12): p. 28-32.
54. Ewing, R.C., W. Lutze, and W.J. Weber, *Zircon: A host-phase for the disposal of weapons plutonium.* Journal of Materials Research, 1995. **10**(02): p. 243-246.
55. Lutze, W. and R.C. Ewing, *Radioactive waste forms for the future*. 1988. Medium: X; Size: Pages: (712 p).
56. Lian, J., et al., *Ion beam irradiation in $La_2Zr_2O_7$ - $Ce_2Zr_2O_7$ pyrochlore.* Nuclear Instruments and Methods in Physics Research Section B: Beam Interactions with Materials and Atoms, 2004. **218**: p. 236-243.
57. Ewing, R.C., et al., *Radiation Effects in Zircon.* Reviews in Mineralogy and Geochemistry, 2003. **53**(1): p. 387-425.
58. Jia, C.-J., et al., *Selective Synthesis of Monazite- and Zircon-type $LaVO_4$ Nanocrystals.* The Journal of Physical Chemistry B, 2005. **109**(8): p. 3284-3290.
59. A. T, A., *Crystal Chemistry of ABO_4 Compounds*, in *Geochemical Behavior of Disposed Radioactive Waste*. 1984, American Chemical Society. p. 305-314.
60. Chen, G., et al., *Pressure-induced phase transition in $YVO_4:Eu^{3+}$: An emission lifetime study at high pressure.* Solid State Communications, 1992. **84**(3): p. 313-315.
61. Errandonea, D., M. Somayazulu, and D. Häusermann, *Phase transitions and amorphization of $CaWO_4$ at high pressure.* physica status solidi (b), 2003. **235**(1): p. 162-169.
62. Fukunaga, O. and S. Yamaoka, *Phase transformations in ABO_4 type compounds under high pressure.* Physics and Chemistry of Minerals, 1979. **5**(2): p. 167-177.
63. Ma, J., Q. Wu, and Y. Ding, *Selective synthesis of monoclinic and tetragonal phase $LaVO_4$ nanorods via oxides-hydrothermal route.* Journal of Nanoparticle Research, 2008. **10**(5): p. 775-786.
64. Seifert, K.F., *Untersuchungen zur druck-kristallchemie der AX_2-verbindungen.* Fortschr. Mineral, 1968. **45**: p. 214-280.
65. Bastide, J.P., *Systématique simplifiée des composés ABX_4 ($X = O^{2-}, F^-$) et evolution possible de leurs structures cristallines sous pression.* Journal of Solid State Chemistry, 1987. **71**(1): p. 115-120.
66. Ruschel, K., et al., *A Raman spectroscopic study on the structural disorder of monazite–(Ce).* Mineralogy and Petrology, 2012. **105**(1-2): p. 41-55.

67. Nasdala, L., et al., *Irradiation damage in monazite - (Ce): An example to establish the limits of Raman confocality and depth resolution.* The Canadian Mineralogist, 2010. **48**(2): p. 351-359.
68. Picot, V., et al., *Ion beam radiation effects in monazite.* J. Nucl. Mater., 2008. **381**(3): p. 290-296.
69. Meldrum, A., L.A. Boatner, and R.C. Ewing, *Displacive radiation effects in the monazite- and zircon-structure orthophosphates.* Physical Review B, 1997. **56**(21): p. 13805-13814.
70. Lu, F., et al., *Tailoring the radiation tolerance of vanadate-phosphate fluorapatites by chemical composition control.* RSC Advances, 2013. **3**(35): p. 15178-15184.
71. Hunter, B., *Rietica-A visual rietveld program.* 2000.
72. Le Bail, A., H. Duroy, and J.L. Fourquet, *Ab-initio structure determination of $LiSbWO_6$ by X-ray powder diffraction.* Materials Research Bulletin, 1988. **23**(3): p. 447-452.
73. Jaksch, H., *Strain related Contrast mechanisms in crystalline materials imaged with AsB detection*, in *EMC 2008 14th European Microscopy Congress 1–5 September 2008, Aachen, Germany*, M. Luysberg, K. Tillmann, and T. Weirich, Editors. 2008, Springer Berlin Heidelberg. p. 553-554.
74. Degueldre, C. and J. Paratte, *Concepts for an inert matrix fuel, an overview.* J. Nucl. Mater., 1999. **274**(1): p. 1-6.
75. Imaura, A., N. Touran, and R.C. Ewing, *MgO–pyrochlore composite as an inert matrix fuel: Neutronic and thermal characteristics.* J. Nucl. Mater., 2009. **389**(3): p. 341-350.
76. Kleykamp, H., *Selection of materials as diluents for burning of plutonium fuels in nuclear reactors.* J. Nucl. Mater., 1999. **275**(1): p. 1-11.
77. Degueldre, C., *Zirconia inert matrix for plutonium utilisation and minor actinides disposition in reactors.* J. Alloys Compd. , 2007. **444–445**: p. 36-41.
78. Sokolov, F. and H. Nawada, *Viability of Intert Matrix Fuel in Reducing Plutonium Amounts in Reactors.* International Atomic Energy Agency, 2006: p. 1.
79. Lutique, S., et al., *Zirconate pyrochlore as a transmutation target: thermal behaviour and radiation resistance against fission fragment impact.* J. Nucl. Mater., 2003. **319**: p. 59-64.
80. Konings, R., et al., *Transmutation of actinides in inert-matrix fuels: fabrication studies and modelling of fuel behaviour.* J. Nucl. Mater., 1999. **274**(1): p. 84-90.
81. Matzke, H., V. Rondinella, and T. Wiss, *Materials research on inert matrices: a screening study.* J. Nucl. Mater., 1999. **274**(1): p. 47-53.
82. Xu, P., et al., *Dissolution behavior of MgO–pyrochlore composites in acidic solutions.* J. Nucl. Mater., 2009. **394**(1): p. 39-45.
83. Yates, S., K. McClellan, and J. Nino, *The effect of processing on the thermal diffusivity of MgO–$Nd_2Zr_2O_7$ composites for inert matrix materials.* J. Nucl. Mater., 2009. **393**(2): p. 203-211.
84. Shukla, P., et al., *Thermal transport properties of MgO and $Nd_2Zr_2O_7$ pyrochlore by molecular dynamics simulation.* J. Nucl. Mater., 2008. **380**(1): p. 1-7.
85. Yates, S., et al., *Processing of magnesia–pyrochlore composites for inert matrix materials.* J. Nucl. Mater., 2007. **362**(2): p. 336-342.
86. Lutique, S., et al., *The thermal conductivity of $Nd_2Zr_2O_7$ pyrochlore and the thermal behaviour of pyrochlore-based inert matrix fuel.* J. Alloys Compd. , 2003. **352**(1–2): p. 1-5.
87. Nelson, A.T., et al., *Effect of composition on thermal conductivity of MgO– $Nd_2Zr_2O_7$ composites for inert matrix materials.* J. Nucl. Mater., 2014. **444**(1): p. 385-392.
88. Xu, P., S.J. Yates, and J.C. Nino, *Hydrothermal corrosion of magnesia-pyrochlore composites for inert matrix materials.* J. Compos. Mater., 2010. **44**(12): p. 1533-1545.

89. Medvedev, P.G., M.J. Lambregts, and M.K. Meyer, *Thermal conductivity and acid dissolution behavior of $MgO–ZrO_2$ ceramics for use in LWR inert matrix fuel.* J. Nucl. Mater., 2006. **349**(1–2): p. 167-177.
90. Ewing, R.C., W.J. Weber, and J. Lian, *Nuclear waste disposal—pyrochlore ($A_2B_2O_7$): Nuclear waste form for the immobilization of plutonium and "minor" actinides.* J. Appl. Phys., 2004. **95**(11): p. 5949-5971.
91. Gregg, D.J., et al., *The incorporation of plutonium in lanthanum zirconate pyrochlore.* J. Nucl. Mater., 2013. **443**(1–3): p. 444-451.
92. Lang, M., et al., *Review of $A_2B_2O_7$ pyrochlore response to irradiation and pressure.* Nucl. Instrum. Methods Phys. Res., Sect. B 2010. **268**(19): p. 2951-2959.
93. Wu, J., et al., *Low thermal conductivity rare earth zirconates for potential thermal barrier coating applications.* J. Am. Ceram. Soc., 2002. **85**(12): p. 3031-3035.
94. Bhattacharya, A., et al., *Electrical characterization of spherical $Ln_2Zr_2O_7$ (Ln=La, Nd, Dy) prepared via a low temperature sol-gel route.* Eur. J. Solid State Inorg. Chem. , 1996. **33**(5): p. 441-452.
95. Bhattacharya, A., et al., *Preparation and characterization of $Ln_2Zr_2O_7$ microspheres by an inorganic sol-gel route.* J. Mater. Sci. Lett., 1994. **29**(23): p. 6076-6078.
96. Nästren, C., et al., *Actinide incorporation in a zirconia based pyrochlore ($Nd_{1.8}An_{0.2})Zr_2O_{7+x}$ (An = Th, U, Np, Pu, Am).* J. Solid State Chem., 2009. **182**(1): p. 1-7.
97. Sedmidubský, D., O. Beneš, and R. Konings, *High temperature heat capacity of $Nd_2Zr_2O_7$ and $La_2Zr_2O_7$ pyrochlores.* J. Chem. Thermodyn, 2005. **37**(10): p. 1098-1103.
98. Lutique, S., et al., *The low-temperature heat capacity of some lanthanide zirconates.* J. Chem. Thermodyn, 2004. **36**(7): p. 609-618.
99. Lutique, S., et al., *Low temperature heat capacity of $Nd_2Zr_2O_7$ pyrochlore.* J. Chem. Thermodyn, 2003. **35**(6): p. 955-965.
100. Rao, K.K., et al., *Preparation and characterization of bulk and nano particles of $La_2Zr_2O_7$ and $Nd_2Zr_2O_7$ by sol–gel method.* Mater. Lett., 2002. **54**(2): p. 205-210.
101. Karmali, R., et al., *Citrate gel route for synthesis of dense pyrochlores.* Mater. Chem. Phys., 2011. **129**(3): p. 1116-1120.
102. Lee, Y., H. Sheu, and H.-C. Kao, *Preparation and characterization of $Nd_2Zr_2O_7$ nanocrystals by a polymeric citrate precursor method.* Mater. Chem. Phys., 2010. **124**(1): p. 145-149.
103. Shimamura, K., et al., *Thermophysical properties of rare-earth-stabilized zirconia and zirconate pyrochlores as surrogates for actinide-doped zirconia.* Int. J. Thermophys., 2007. **28**(3): p. 1074-1084.
104. Pechini, M.P., *Method of preparing lead and alkaline earth titanates and niobates and coating method using the same to form a capacitor*. 1967, US Patent 3,330,697.
105. Kong, L., et al., *A novel chemical route to prepare $La_2Zr_2O_7$ pyrochlore.* J. Am. Ceram. Soc., 2013. **96**(3): p. 935-941.
106. Kong, L., et al., *$Gd_2Zr_2O_7$ and $Nd_2Zr_2O_7$ pyrochlore prepared by aqueous chemical synthesis.* J. Eur. Ceram. Soc., 2013. **33**(15): p. 3273-3285.
107. Luo, J., R. Stevens, and R. Taylor, *Thermal diffusivity/conductivity of magnesium oxide/silicon carbide composites.* J. Am. Ceram. Soc., 1997. **80**(3): p. 699-704.
108. Kopp, H., *Investigations of the specific heat of solid bodies.* Philosophical Transactions of the Royal Society of London, 1865. **155**: p. 71-202.
109. Wang, B., L. Zhou, and X. Peng, *Surface and size effects on the specific heat capacity of nanoparticles.* Int. J. Thermophys., 2006. **27**(1): p. 139-151.
110. Holland, M.G., *Analysis of lattice thermal conductivity.* Phys. Rev., 1963. **132**(6): p. 2461-2471.
111. Stauffer, D. and A. Aharony, *Introduction to percolation theory*. 1994: CRC press.

112. Hagrman, D.L. and G.A. Reymann, *MATPRO-Version 11: A handbook of materials properties for use in the analysis of light water reactor fuel rod behavior*. 1979. p. Medium: ED.
113. Lumpkin, G.R. and T. Geisler-Wierwille, *5.22 - Minerals and Natural Analogues*, in *Comprehensive Nuclear Materials*, R.J.M. Konings, Editor. 2012, Elsevier: Oxford. p. 563-600.
114. Weber, W.J., et al., *Radiation effects in crystalline ceramics for the immobilization of high-level nuclear waste and plutonium.* Journal of Materials Research, 1998. **13**(06): p. 1434-1484.
115. Deschanels, X., et al., *Plutonium incorporation in phosphate and titanate ceramics for minor actinide containment.* J. Nucl. Mater., 2006. **352**(1–3): p. 233-240.
116. Ziegler, J., et al., *Stopping power and ranges of ions in matter, Vol. 1Pergamon.* New York, 1985.
117. Harold P. Klug and L.E. Alexander, *X-Ray Diffraction Procedures: For Polycrystalline and Amorphous Materials*. 2nd ed. 1974.
118. Mather, S.A. and P.K. Davies, *Nonequilibrium phase formation in oxides prepared at low temperature: Fergusonite-telated phases.* Journal of the American Ceramic Society, 1995. **78**(10): p. 2737-2745.
119. Gnnseu, J., *Crystal Chemistry of Complex Niobium and Tantalum Oxides lll. Relationship Between M, T, and M'Fergusonite Structures.* American Mineralogist, 1974. **59**: p. 1045-1046.
120. Simeone, D., et al., *Phase transition of pure zirconia under irradiation: A textbook example.* Nuclear Instruments and Methods in Physics Research Section B: Beam Interactions with Materials and Atoms, 2006. **250**(1): p. 95-100.
121. Simeone, D., et al., *Investigation on the zirconia phase transition under irradiation.* J. Nucl. Mater., 2000. **281**(2–3): p. 171-181.
122. Jian, Z. and W. Hejing, *The physical meanings of 5 basic parameters for an X-ray diffraction peak and their application.* Chinese Journal of Geochemistry, 2003. **22**(1): p. 38-44.
123. Partyka, P., et al., *Damage and lattice strain in ion‐irradiated AlAs.* Applied Physics Letters, 1994. **65**(4): p. 421-423.
124. Falkovsky, L.A., *Width of optical phonons: Influence of defects of various geometry.* Physical Review B, 2001. **64**(2): p. 024301.
125. Zhang, M., et al., *Metamictization of zircon: Raman spectroscopic study.* Journal of Physics: Condensed Matter, 2000. **12**(8): p. 1915.
126. Zinkle, S., *Microstructure of ion irradiated ceramic insulators.* Nuclear Instruments and Methods in Physics Research Section B: Beam Interactions with Materials and Atoms, 1994. **91**(1): p. 234-246.
127. Zinkle, S., *Effect of irradiation spectrum on the microstructural evolution in ceramic insulators.* J. Nucl. Mater., 1995. **219**: p. 113-127.
128. Achary, S.N., et al., *Crystal structure analysis of scheelite and zircon type thorium germanates: A neutron diffraction study.* J. Alloys Compd. , 2007. **438**(1–2): p. 274-278.
129. Bayer, G., *Thermal expansion of ABO_4 compounds with zircon and scheelite structures.* Journal of the Less Common Metals, 1972. **26**(2): p. 255-262.
130. Dymshits, O.S., et al., *Structural characteristics and spectral properties of novel transparent lithium aluminosilicate glass-ceramics containing (Er,Yb)NbO_4 nanocrystals.* Journal of Luminescence, 2015. **160**: p. 337-345.
131. Jurkschat, K., et al., *In situ high temperature phase transformations in rare earth niobates.* Advances in X-Ray Analysis, 2004. **47**: p. 357-362.

132. W M Kriven, P Sarin, and L F Siah, *Phase transformations in rare earth niobates*, in *Solid-to-Solid Phase Transformations in Inorganic Materials* James M. Howe, et al., Editors. 2005.
133. Benyagoub, A., *Mechanism of the monoclinic-to-tetragonal phase transition induced in zirconia and hafnia by swift heavy ions.* Physical Review B, 2005. **72**(9): p. 094114.
134. Loiko, P.A., et al., *Dispersion and anisotropy of thermo-optic coefficients in tetragonal $GdVO_4$ and YVO_4 laser host crystals.* Applied Optics, 2013. **52**(4): p. 698-705.
135. Mikhailik, V.B., et al., *Structure, luminescence and scintillation properties of the $MgWO_4$ – $MgMoO_4$ system.* Journal of Physics: Condensed Matter, 2008. **20**(36): p. 365219.
136. Blasse, G. and A. Bril, *Luminescence of phosphors based on host lattices ABO_4 (A is Sc, In; B is P, V, Nb).* The Journal of Chemical Physics, 1969. **50**(7): p. 2974-2980.
137. Capitani, C.G., et al., *A TEM investigation of natural metamict zircons: Structure and recovery of amorphous domains.* Physics and Chemistry of Minerals. **27**(8): p. 545-556.
138. Nasdala, L., et al., *Metamictisation of natural zircon: Accumulation versus thermal annealing of radioactivity-induced damage.* Contributions to Mineralogy and Petrology, 2004. **141**(2): p. 125-144.
139. Zhang, Y., N.A.W. Holzwarth, and R.T. Williams, *Electronic band structures of the scheelite materials $CaMoO_4$, $CaWO_4$, $PbMoO_4$, and $PbWO_4$.* Physical Review B, 1998. **57**(20): p. 12738-12750.
140. Jagielski, J., et al., *Luminescence analysis of damage accumulation; case study of calcium molybdate.* Nuclear Instruments and Methods in Physics Research Section B: Beam Interactions with Materials and Atoms, 2014. **332**(0): p. 60-62.
141. Patel, M.K., et al., *Swift heavy ion induced structural modifications in zircon and scheelite phases of $ThGeO_4$.* Nuclear Instruments and Methods in Physics Research Section B: Beam Interactions with Materials and Atoms, 2010. **268**(1): p. 42-48.
142. Ziegler, J.F. and J.P. Biersack, *The stopping and range of ions in matter*. 1985: Springer.
143. Grover, V., et al., *Effect of grain size and microstructure on radiation stability of CeO_2: An extensive study.* Physical Chemistry Chemical Physics, 2014. **16**(48): p. 27065-27073.
144. Venugopalan Pillai, N., et al., *Effect of ZnO doping on the structural and optical properties of $BaWO_4$ thin films prepared using pulsed laser ablation technique.* Pramana, 2011. **75**(6): p. 1157-1161.
145. Zhu, Y., et al., *Structures and effects of radiation damage in cuprate superconductors irradiated with several-hundred-MeV heavy ions.* Physical Review B, 1993. **48**(9): p. 6436-6450.
146. Morehead, F.F. and B.L. Crowder, *A model for the formation of amorphous Si by ion bombardment.* Radiation Effects, 1970. **6**(1): p. 27-32.
147. Spinella, C., et al., *Mechanism and kinetics of the ion-assisted nucleation in amorphous silicon.* Physical Review B, 1996. **53**(12): p. 7742-7749.
148. Dhaka, V.D.S., et al., *Room-temperature self-annealing of heavy-ion-irradiated InGaAs/GaAs quantum wells.* Electronics Letters, 2005. **41**(23): p. 1304-1305.